Proximity induced exchange coupling in graphene

MASTER THESIS

Summer term 2016
University of Regensburg
Faculty of Physics

Author:
Klaus Zollner

Matriculation number:
156 022 9

Supervisors:
Prof. Dr. Jaroslav Fabian
Dr. Martin Gmitra
Tobias Frank

July 14, 2016

Contents

Chapter 1

Introduction

In current solid state physics, researchers often investigate van-der-Waals (vdW) heterostructures. On the one hand, the technical know-how to produce and post process thin slabs from many layered crystals allows multiple material combinations. On the other hand, the diversity of materials that already intrinsically possess extraordinary properties in a 2D-arrangement, is very large (hexagonal boron nitride (hBN), transition metal dichalcogenides (TMDC), phosphorene, topological insulators as Bi_2Se_3). In contrast to semiconductor physics, where different materials are brought into contact for the purpose of band gap engineering, vdW structures rely on proximity mediated properties, like magnetism or spin-orbit coupling (SOC).

An often used material for vdW structures is graphene due to its prominent properties, like high electron mobility and its spin quantities, which are especially attractive in electronics when building new and faster integrated circuits. The mobility of graphene for instance, has been measured to 10.000 $\frac{\mathrm{cm}^2}{\mathrm{Vs}}$ [1, 2] at room temperature, giant compared to the usual semiconducting devices. Combined with its mechanical properties [3], making graphene the strongest material ever measured, it could be useful in producing flexible graphene-based displays [4] and the creation of next generation high-tech devices. Graphene is also interesting when it comes to manipulating electron spins, potentially leading to spintronic devices [5, 6]. Especially spin relaxation and spin transport can be altered, by the enhancement of SOC [7, 8].

There are several possibilities to modify the electronic properties of graphene. One way is to introduce adatoms or admolecules on graphene in order to enhance spin-orbit interaction. There have been lots of investigations with light [9–15] and heavy [16–20] adatoms, as well as small organic molecules [21]. It has been shown, that SOC parameters of the order of 1 meV are used in tight binding Hamiltonians to describe the induced SOC strength, giant compared to the intrinsic SOC of graphene ($\lambda_\mathrm{I} \approx 12$ μeV [22]). Recent scanning tunneling microscopy (STM) experiments on hydrogenated graphene confirm the theoretically predicted induced spin polarization in graphene by hydrogen adatoms [23].

Additionally one can alter the physics of graphene, by building vdW heterostructures with insulating or metallic materials [24–33]. There have been several theoretical predictions and experiments for graphene on an insulating substrate, like hBN, where they found a gap in the band structure of graphene at the K point, due to the breaking of graphenes sublattice symmetry [24]. The predicted band gap of a graphene/hBN structure is of the order of 50 meV and is of essential value when building graphene-based field-effect transistor devices. This effect is not only limited to hBN, but in general every substrate, breaking the sublattice symmetry of graphene, leads to a gap in the graphene band structure. Insulating materials,

especially hBN, are potentially efficient spin selective tunneling barriers [26], which is very interesting for spintronics applications.

However, in electronics, one needs to be able to make contacts to graphene, most likely with metals, in order to inject electrons, measure the physical quantities of graphene and make possible vdW structures ready for application. By placing graphene on a metallic substrate, it is possible to completely destroy the known linear band structure of graphene at the K point [25, 31], especially when graphene is chemisorbed on the metal, as for the ferromagnets cobalt and nickel. However, for graphene-based devices, it is not desirable to destroy the linear dispersion, since transport properties are based on it. The band structure can be preserved, if graphene is physisorbed on the metal, as it is for Cu, Au or Pt. Depending on the kind of metal, one can also p-/n-dope graphene, since the Dirac point of graphene gets shifted with respect to the Fermi level. This is a consequence of the different work functions in graphene and the metal, leading to charge transfer and doping [25]. It has also been shown that graphene on a copper surface experiences strong distance dependent SOC due to the hybridization of graphene π with copper d states [30]. The first-principles calculations for graphene on the Cu(111) surface match well with the measured angle-resolved photoemission spectroscopy (ARPES) band structure and can be fitted by a robust low energy model Hamiltonian in the vicinity of the K point. Experiments on ferromagnet/graphene interfaces [32, 33] show that one atom thick single layer of graphene is enough to efficiently protect ferromagnetic spin sources against oxidation and preserve the measurable spin-valve signal in agreement with theory [34, 35]. Concerning the spin properties, especially graphene has attracted a lot of attention due to its theoretical predicted very long spin relaxation times of $\tau \approx 1$ μs and lengths of $l_s \approx 100$ μm [36, 37]. Strong SOC is desirable, for the observation of many interesting phenomena, like spin-Hall effect. On the other hand, it is responsible for spin relaxation.

A possibility to preserve the conical band structure, is to form graphene/insulator/metal heterostructures. One can imagine, that the insulating layer protects graphene from strong proximity effects, such that the general conical dispersion of graphene stays untouched. Investigations on structures of graphene on the ferromagnetic insulator EuO shows a tunable magnetic proximity effect leading to spin dependent Fermi velocity v_{F}, hybridization gap and large spin polarizations of the order of 25% [38]. Also graphene/insulator/ferromagnet structures show a similar behavior. Ferromagnetic substrates induce weak proximity magnetism into graphene, while an insulating buffer layer preserves the graphene band structure. Experimental and theoretical investigations of Ni(111)/hBN/graphene structures [27, 39] show a very efficient spin-injection into graphene. They also find an inversion of the measured spin-valve signal due to increasing barrier thickness. Figure 1.1 shows the schematic diagram of the spin injection from a ferromagnetic electrode to graphene through the tunnel barrier hBN, acting as spin dependent tunnel barrier [27]. Spins, injected by the ferromagnet/hBN junction, accumulate in the graphene and lead to the splitting of the chemical potential. The spin polarization of graphene can then be detected nonlocally by another ferromagnet/hBN junction, placed at a distance of typical spin diffusion length (≈ 2 μm), as reported by *Kamalakar et al.* [26].

All these findings already show that there was progress towards a spin logic device, that could replace conventional electronic devices in near future [33, 40–42]. However, there is still a lot of work to do, since SOC could be also strong in these systems, affecting the spin-lifetimes in graphene significantly. The goal is to find the right balance between high spin-injection and polarization, but also long spin-lifetimes. Thus it is crucial to investigate possible magnetic

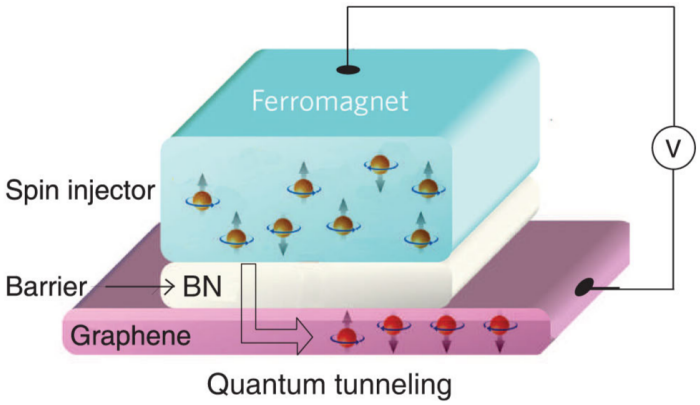

FIG. 1.1: Schematic diagram showing the spin injection from a ferromagnetic electrode to graphene through the tunnel barrier hBN, acting as spin dependent tunnel barrier, leading to spin polarized current in graphene; taken from Ref. [27].

and spin-orbit proximity effects from ferromagnets and insulators affecting graphene.

This thesis deals with the proximity induced exchange coupling, induced from the ferromagnets cobalt and nickel through different insulators, in graphene. In chapter 2 we first deal with every single layer on its own, to get a feeling and understanding of their properties. Especially we are interested if the density functional theory (DFT) calculations cover the essential features, like linear dispersion in graphene, size of the gap of insulators and spin magnetic moment of the ferromagnets. We give an overview on the essential properties, like crystal structure and application in research, describe the band structures and the density of states (DOS) in terms of spin and orbital decomposition. In chapter 3 we essentially deal with two kinds of heterostructures with the difference in the used ferromagnet. The structures are based on graphene and hBN, matched with the ferromagnets cobalt and nickel. We search for the energetically favorable stacking of the layers and explore the modification of the graphene band structure. We introduce an effective low energy model Hamiltonian in order to reproduce the graphene band structure and extract valuable exchange parameters from the DFT data, which are essential for experimentalists and research. We study the effects of a transverse electric field, change the insulator and ferromagnet thicknesses and look at possible modifications in the band structure. In chapter 4 we take a brief look at two other insulating barriers, namely Al_2O_3 and SiO_2, by replacing hBN.

Chapter 2

Single Layers

In this chapter we want to look at the individual single layers, which will be the building blocks of our vdW heterostructures. In order to understand, which characteristics originate from which layer, orbitals and states in the band structure and the DOS of the vdW systems, it is crucial to get an understanding for the characteristics of the single layers, since they are *closed* systems themselves and possess their special features.

As we are looking at graphene/insulator/ferromagnet heterostructures, there are several possibilities for the choices of the insulator and the ferromagnet. Our main focus will be on hBN as the insulator, since the lattice is also hexagonal and can be nicely matched to the one of graphene in a commensurable way. Other choices can be oxide insulators like SiO_2, Al_2O_3, TiO_2 and MgO. But we will not be able to cover all the combinations, since the computational effort for some systems, especially when large supercells are necessary to match the lattices, is too high. In addition to hBN, we look at SiO_2 and Al_2O_3, as they are typical barriers for spin injection and detection. The ferromagnets which we consider are cobalt and nickel, but also iron is a candidate to induce proximity magnetism in graphene. Cobalt is the most simple choice, since it already crystallizes in a hexagonal lattice. Also nickel can be easily matched with graphene, when we consider the (111)-plane of the fcc-lattice. Iron however, is problematic if we want to match the lattice with graphene in a commensurable way and keep the vdW system supercell small.

The fact that a material can magnetize graphene due to proximity is not only limited to ferromagnets. Recent investigations on ferromagnetic insulators, such as europium oxide (EuO) and yttrium iron garnet (YIG), show proximity induced magnetism in graphene [38, 43], leading to strong spin polarization of the π states of graphene. This manifests in the lifting of the spin degeneracy of the Dirac states, along with a spin dependent gap, due to sublattice symmetry breaking.

In this chapter we will only consider the different materials in their bulk crystal structures (monolayers for graphene and hBN) to get an understanding of the special characteristics. Later, when we come to heterostructures, we consider each individual crystal in a thin slab geometry stacked on top of each other. Of course, the number of atomic layers of the individual single materials and the stacking order among them will influence the proximity induced effects. A more detailed description of the calculations and the input parameters, which we used for the single layers, is given in appendix B.3.

2.1. Graphene

Carbon is an important element, since all living (organic) compounds contain it. Carbon atoms have an electronic configuration [He] $2s^2 2p^2$, and thus have 4 valence electrons, which makes it tetravalent to form covalent bonds. Usually, carbon is found in hydrocarbons, which are essential for industry (fossil fuels, plastics).

A highly discussed material, which exclusively consists of carbon atoms, is graphene. Its prominent properties, like high electron mobility, optical transparency and mechanical robustness [44], make it interesting for research and electronic applications. The lattice of graphene is shown in Fig. 2.1 with the lattice constant $a = \sqrt{3}a_0 \approx 2.46$ Å, where $a_0 = 1.42$ Å is the distance between next-nearest carbon atoms [45]. Graphene contains two nonequivalent carbon atoms in the unit cell and thus it is made up from two trigonal sublattices A and B. The reciprocal lattice is also hexagonal, containing the high symmetry points Γ, M and K. Figure 2.2 shows the band structure and the corresponding orbital resolved DOS of graphene.

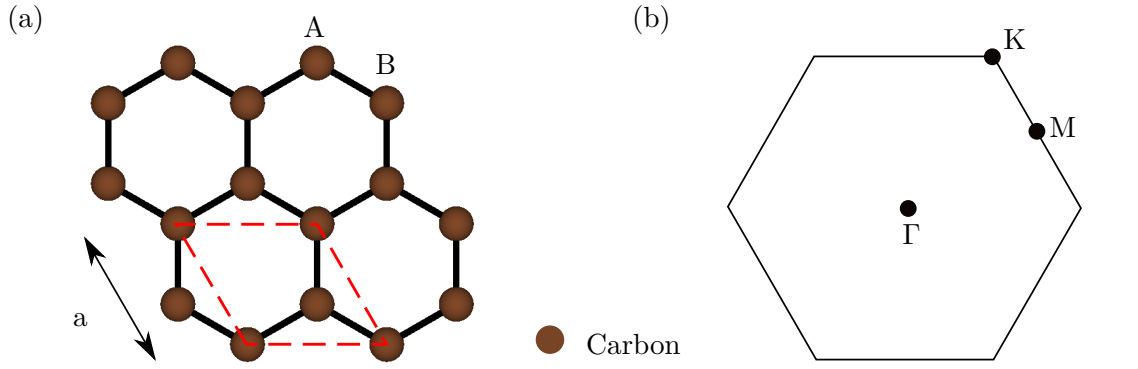

FIG. 2.1: Unit cell and Brillouin Zone of graphene. (a) Lattice of graphene with lattice constant $a = 2.46$ Å and labels for sublattice A and B. One unit cell is emphasized by the dashed line. (b) First Brillouin Zone of the reciprocal lattice. Γ, M, K are non-equivalent high symmetry points.

The s, p_x and p_y orbitals in graphene are forming sp^2 hybridized covalent σ-bonds in the plane, lying low in energy, which are responsible for the robustness of graphene. The remaining p_z orbitals which point out of plane are responsible for the π-bands near the Fermi energy and determine the electric transport properties [46]. The Fermi energy is located at the K point, where conduction and valence states touch, making graphene semi-metallic. The K point is called Dirac point, since the dispersion is linear in its vicinity and thus the particles show a similar behavior as massless Dirac fermions obeying the Dirac equation. The bands at the Γ point for energies larger than 3 eV show parabolic behavior, which originate form the vacuum spacing in z direction to simulate a single graphene layer.

There have also been tight-binding [45] and experimental [2] studies of the electronic structure of graphene, which match well with the DFT results presented here. Monolayers of graphene can be produced via mechanical exfoliation [44] or by chemical vapor deposition (CVD) on metal substrates [47]. Graphene has attracted a lot of attention due to its theoretical predicted very long spin relaxation times of $\tau \approx 1$ μs and lengths of $l_s \approx 100$ μm [36, 37]. However, theoretical and experimental studies show much larger SOC and thus spin relaxation due to adatoms or other sources, see for example Refs. [10, 12]. Adatoms, e.g. hydrogen [10], cause a local sp^3 corrugation of the lattice and locally enhance the SOC strength with SOC

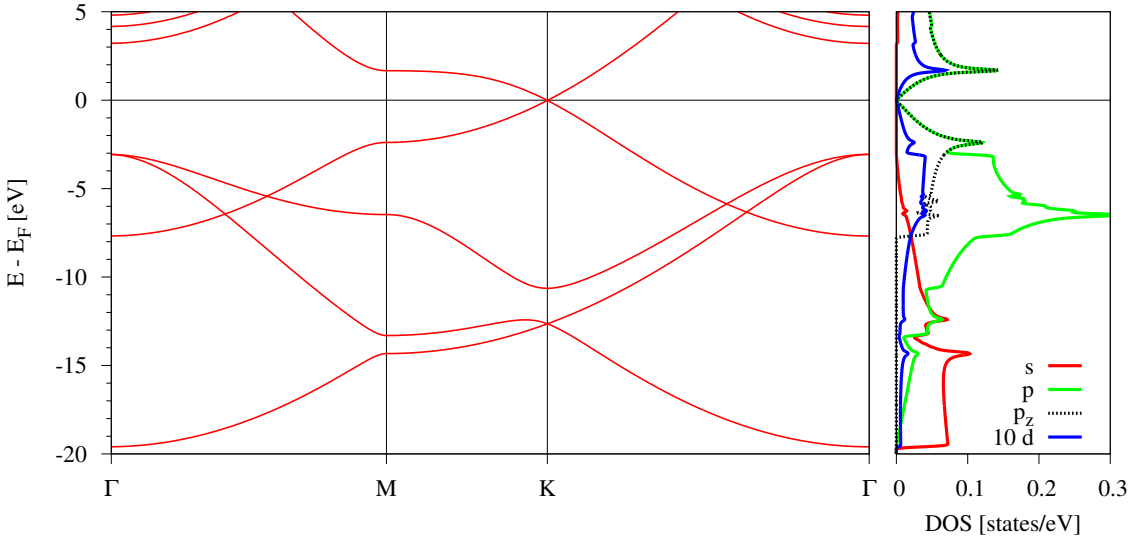

FIG. 2.2: Band structure and corresponding orbital resolved DOS of graphene. Left panel: Band structure along the high symmetry path Γ–M–K–Γ. Right panel: Orbital resolved DOS. DOS of d states is multiplied by a factor 10.

parameters of the order of 1 meV, giant compared to graphenes intrinsic SOC of 12 μeV [22]. Very recently, STM experiments confirmed that hydrogen adatoms cause a local magnetic moment on graphene [23], in agreement with theoretical predictions.

2.2. Hexagonal Boron Nitride

Almost equally interesting are other two dimensional materials. One of them is hexagonal boron nitride (hBN), which is similar to graphene, but an insulator. Boron atoms have an electronic configuration [He] $2s^2 2p^1$ and thus have 3 valence electrons. Nitrogen has the configuration [He] $2s^2 2p^3$ and 5 valence electrons. hBN has the same lattice as graphene and

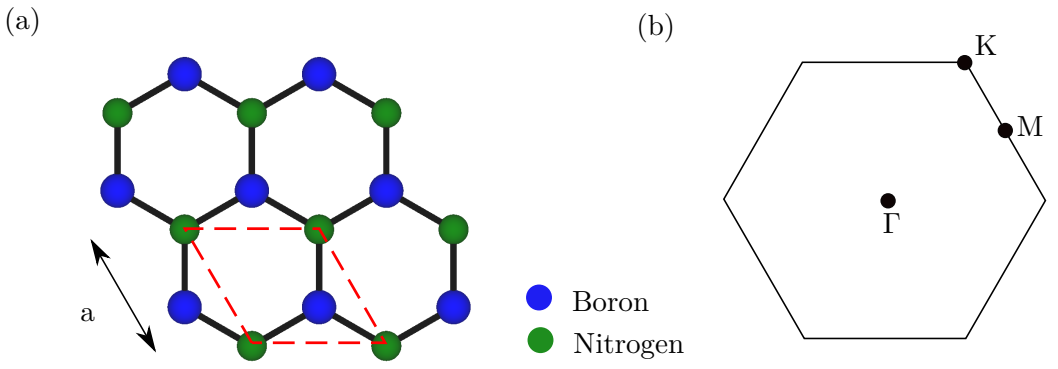

FIG. 2.3: Unit cell and Brillouin Zone of hBN. (a) Lattice of hBN with lattice constant $a = 2.504$ Å. One unit cell is emphasized by the dashed line. (b) First Brillouin Zone of the reciprocal lattice. Γ, M, K are non-equivalent high symmetry points.

is not formed by carbon atoms, but by boron and nitrogen atoms, located on the sublattice

sites A and B, respectively. It is not surprising that the two different atoms can form a honeycomb lattice as graphene, since their electronic configuration in sum is equal. However, due to the strong difference in electronegativity of boron and nitrogen [48], the atoms form an insulating material, as electrons are mainly localized around the nitrogen atom. Thus, hBN can be considered as the insulating analogue of graphite. The unit cell, reciprocal lattice and high-symmetry points are thus defined as for graphene, see Fig. 2.3. The lattice constant of hBN [49] is $a = 2.504$ Å, slightly bigger than the one of graphene and $c = 6.66$ Å, being the lattice constant, defining the interlayer distance in bulk hBN. Bulk hBN has an AA' stacking, meaning that boron (nitrogen) atoms of layer A are on top of nitrogen (boron) atoms of layer A'. The single layers in bulk hBN are held together by vdW bonds.

From the band structure, Fig. 2.4, we can see, that hBN is an insulator, since the calculated band gap is $E_g = 4.681$ eV, which deviates from Ref. [50], where they calculated it to 5.97 eV. The band gap is underestimated by roughly 30%, which is common in DFT, when it comes to insulators or semiconductors. The error in the value of the band gap can be fixed by using an appropriate exchange correlation functional [51]. We can see, that states near the Fermi level are mainly formed by nitrogen p_z orbitals, which are in principle similar to graphene's states near the Fermi level. Still, we have to keep in mind, that hBN is an insulator. The

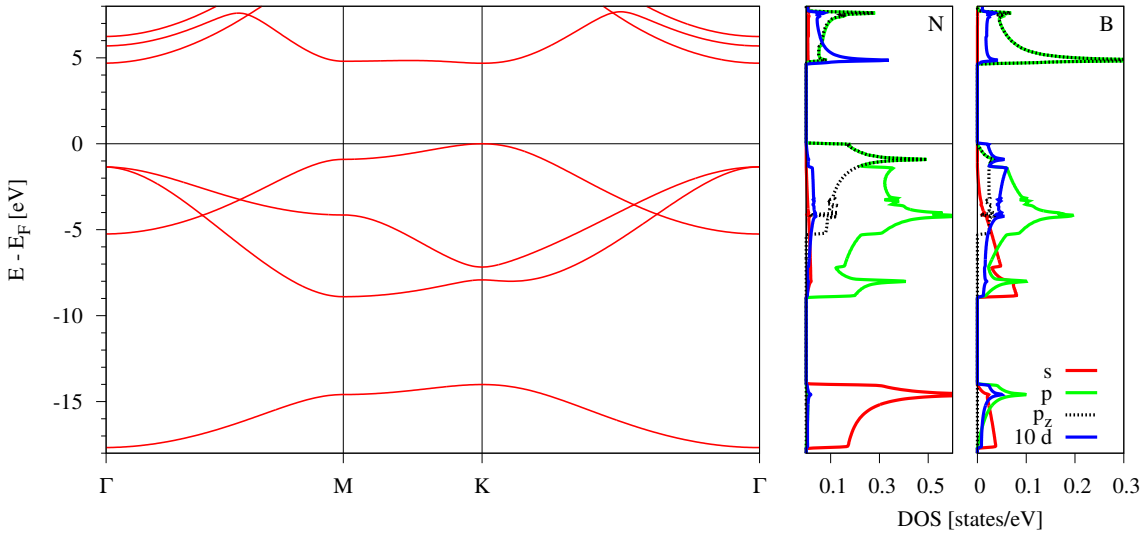

FIG. 2.4: Band structure and corresponding orbital resolved DOS of hBN. Left panel: Band structure along the high symmetry path Γ–M–K–Γ. Right panel: Orbital resolved DOS. DOS of d states are multiplied by a factor of 10. Labels B and N correspond to the boron and nitrogen atoms of the unit cell.

lowest valence band in Fig. 2.4 is almost exclusively formed by nitrogen s states, which hybridize with boron s and p orbitals. In general, s, p_x and p_y orbitals are lying low in energy in the window from -10 to -5 eV, forming the sp^2 hybridized covalent bonds in the plane. Comparing the contributions to the DOS of hBN and graphene, we can see some similarities, reflecting the fact of a hexagonal lattice for both systems.

There have also been tight-binding [52] and other DFT [49] studies of the electronic structure of hBN, which match well with the DFT results presented here, except for the value of the band gap energy. Like graphene, hBN can also be prepared by exfoliation or CVD [53, 54]. There are already investigations on hBN/metal junctions leading to Shottky barriers

[55] or of graphene/hBN junctions introducing a band gap in the graphene dispersion [24]. Compared to oxide insulators, hBN should be a much better candidate for spin devices, since the mobility of graphene is still very high when forming vdW heterostructures and it is potentially a good candidate as a spin filtering tunnel barrier [26, 27, 39, 56].

2.3. Silicon Dioxide

Silicon Dioxide (SiO_2, α-quartz) is one of the most found compounds on earth. It is the building brick of glass and several different gemstones, but it is also considered as very important in technology. It is used in semiconductor and microchip industry as the insulating material in metal-oxide-semiconductor (MOS) transistors or as a substrate material for growing various thin semiconductors or metals. X-cut quartz is a commonly used material in terahertz research due to its dielectric and nonlinear properties.

SiO_2 crystallizes in a trigonal crystal structure with lattice constants $a = 4.913$ Å and $c = 5.405$ Å. The spacegroup is Nr. 154 with the basis of silicon atoms at position $(0.470, 0.0, 0.0)$ and oxygen atoms at position $(0.414, 0.268, 0.119)$, see Ref. [57]. The unit cell contains three SiO_2 molecules, see Fig. 2.5(a). The electronic configuration of silicon is [Ne] $3s^2 3p^2$ and the one of oxygen is [He] $2s^2 2p^4$ and thus silicon forms covalent bonds with four oxygen atoms in a tetrahedral shape, see Fig. 2.5(c). Oxygen atoms serve as the connecting

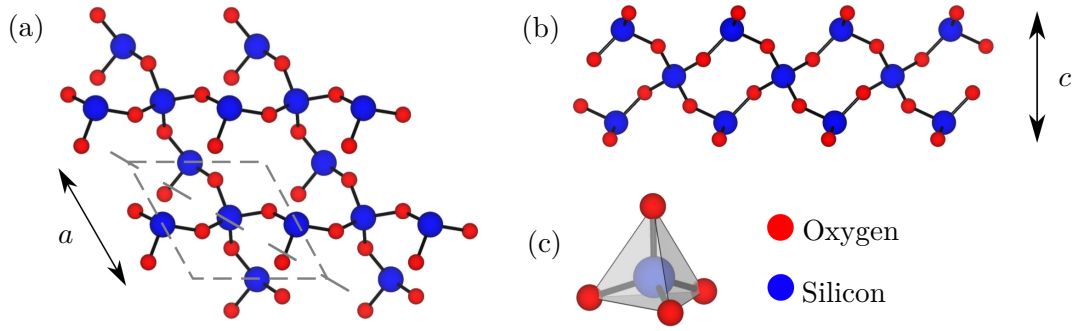

FIG. 2.5: Unit cell and structure of SiO_2. (a) Top view of the trigonal lattice with lattice constants $a = 4.913$ Å and $c = 5.405$ Å. One unit cell is emphasized by the dashed line. Dashed line along diagonal of the unit cell defines the plane of the side view shown in (b). (c) Single tetrahedron formed of one silicon atom and four hydrogen atoms.

bridge between two tetrahedrons and thus SiO_2 appears in many different crystalline forms which are obtained by linking the tetrahedrons together in different ways, but its best known form is amorphous silicon dioxide. Since the lattice constant is nearly twice as large as the one of graphene and the lattice has trigonal symmetry, it is an appropriate candidate for our studies.

Due to previous studies of the graphene/α-SiO_2(0001) interface [29, 58–60], we adopt an oxygen surface termination of SiO_2 at the interface with the graphene and place graphene at the hollow sites above SiO_2 following Ref. [29]. At the interface with the ferromagnets, we take a silicon surface termination of SiO_2. The problem is that from experiments, no unique surface termination can be determined and also the stacking configuration cannot be

predicted for sure and thus we have to rely on our choice.

The predicted band gap for amorphous SiO_2 [61] is $E_g = 8.9$ eV and $E_g = 8.4$ eV for α-quartz [62]. Our calculated value for the bulk α-SiO_2 band gap is $E_g = 6.008$ eV. Again the band gap is underestimated by the calculation. Using an appropriate exchange correlation potential (modified Becke-Johnson) [51], we can get a more accurate band gap of $E_g = 8.88$ eV, but for the heterostructure calculation it is not that important. Nevertheless, SiO_2 is a wide gap insulator. The calculated DOS, Fig. 2.6, is in agreement with Ref. [62]. The valence band

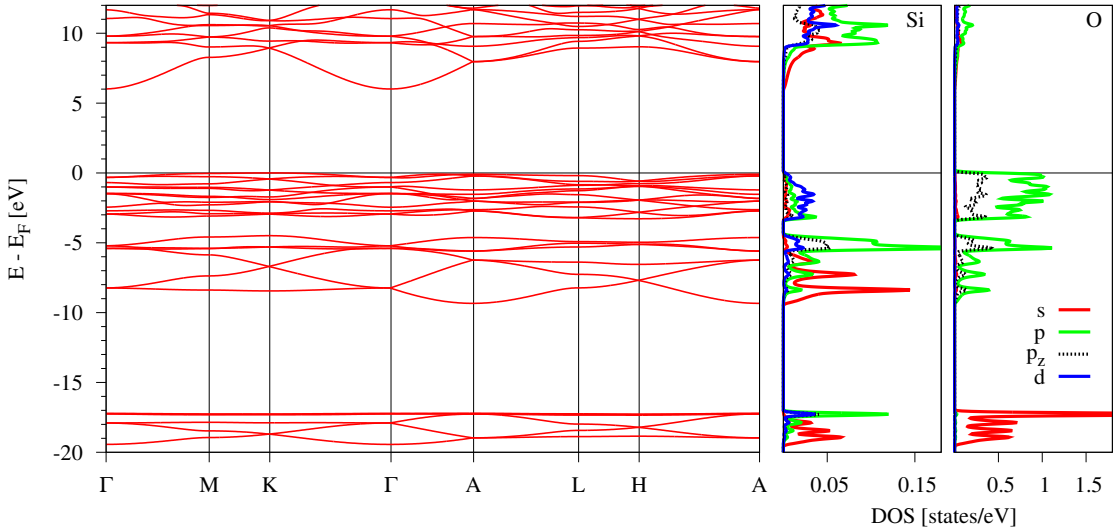

FIG. 2.6: Band structure and corresponding orbital resolved DOS of SiO_2. Left panel: Band structure along the high symmetry path Γ–M–K–Γ–A–L–H–A. Right panel: Atomic and orbital resolved DOS. Labels Si and O correspond to the silicon and oxygen atoms of the unit cell.

DOS can be separated in three regions which are also well separable in the band structure. We can see that the lowest energetic bands are formed by oxygen s orbitals, hybridizing with silicon s and p orbitals in an energy window from -20 to -17 eV. The valence bands near the Fermi level are almost exclusively formed by oxygens p orbitals with some weak interaction to silicon atoms. The part which is responsible for the covalent bonding is at the energy window from -10 to -4 eV arising mainly from oxygen p orbitals and silicon s and p orbitals, forming the sp^3-hybridization. The minimum of the valence band at roughly 6 eV is located at the Γ point and mainly formed by silicon s states. Higher valence bands have mainly silicon p character.

2.4. Aluminum Oxide

Aluminum Oxide (Al_2O_3, corundum) is also a widely used substrate for the growth of metallic or semiconducting thin films in molecular-beam epitaxy (MBE) or metal organic chemical vapor deposition (MOCVD). The (0001)-surface of Al_2O_3 was thus intensively studied during the years [63, 64], predicting an aluminum surface termination [65] with 1/3 monolayer of aluminum. However it is hard to say, which surface termination will be there in experiment. Usually for spin injection experiments, oxide insulators are used, but the barriers often

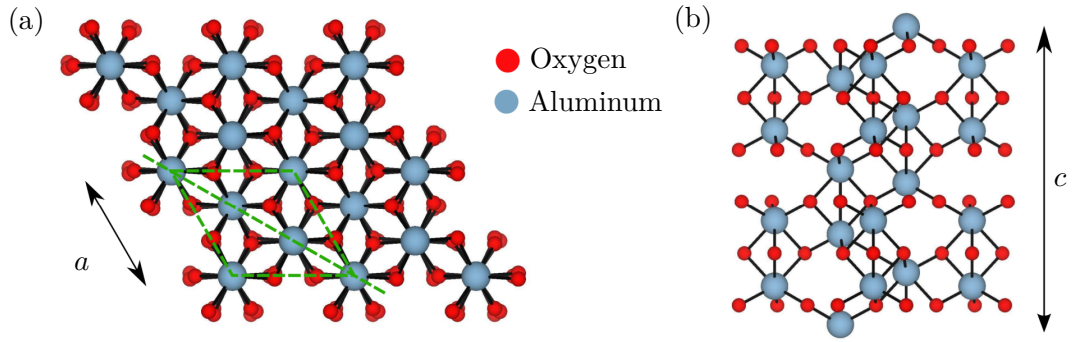

FIG. 2.7: Unit cell and structure of Al_2O_3. (a) Top view of the trigonal lattice with lattice constants $a = 4.758$ Å and $c = 12.98$ Å. One unit cell is emphasized by the dashed line. Dashed line along diagonal of the unit cell defines the plane of the side view shown in (b).

suffer from defects or interface roughness, which makes it hard to produce reproducible heterostructures [18, 66, 67]. By doping Al_2O_3 with titanium or chromium atoms, one can get crystals which are laser active (Sapphire and Ruby crystals) and can thus be used in laser physics to generate radiation.

Al_2O_3 crystallizes in a rhombohedral crystal structure [68] with lattice constant $a = 4.758$ Å and $c = 12.98$ Å. Rhombohedral systems can be treated as hexagonally symmetric, when

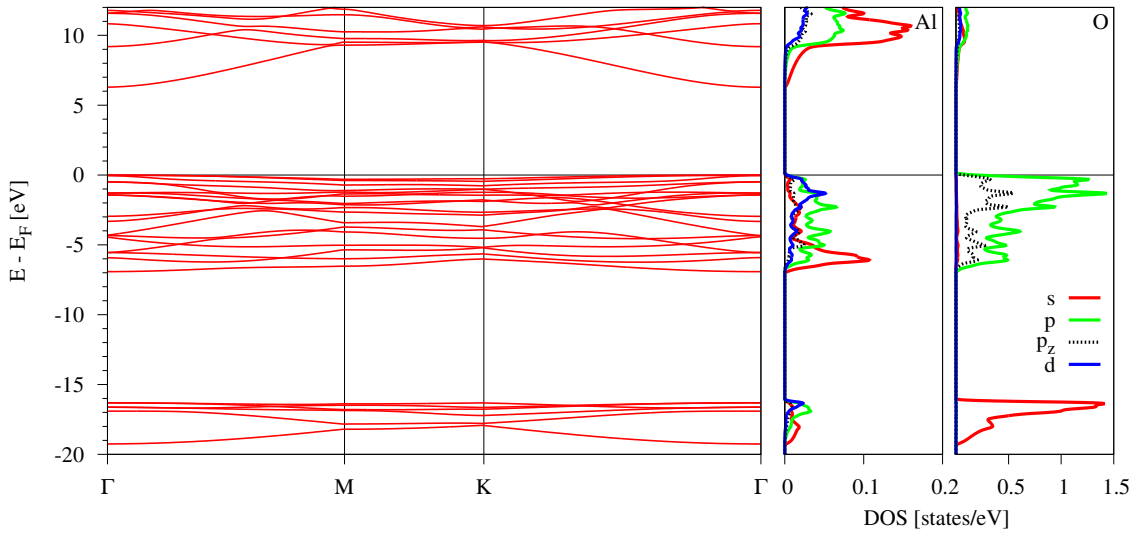

FIG. 2.8: Band structure and corresponding orbital resolved DOS of Al_2O_3. Left panel: Band structure along the high symmetry path Γ–M–K–Γ. Right panel: Atomic and orbital resolved DOS. Labels Al and O correspond to the aluminum and oxygen atoms of the unit cell.

using a larger unit cell, which is done in the following, see Fig. 2.7. Al_2O_3 belongs to the spacegroup Nr. 167 (Hematite group). The unit cell contains six molecules of Al_2O_3 in the hexagonal unit cell. The electronic configuration of aluminum is [Ne] $3s^2 3p^1$ as the direct neighbor of silicon in the periodic table. The predicted band gap is $E_g = 8.8$ eV [69] and our calculated one is $E_g = 6.291$ eV, again underestimated by roughly 30% due to the exchange

correlation potential. Figure 2.8 shows the band structure and the corresponding DOS of Al_2O_3. We can see that the lowest valence states are mainly formed by oxygen s orbitals with a small contribution of aluminum s and p states. The bonding hybridization takes place in the energy window around -6 eV, where oxygen p states mix with aluminum s and p states. The highest lying valence bands are mainly formed by oxygen p states as for SiO_2. From the analysis of the DOS and the band structure we see that the two oxide insulators Al_2O_3 and SiO_2 are very similar.

2.5. Cobalt

Cobalt is a gray ferromagnetic transition metal, which appears in two different modifications (hcp, fcc), depending on the temperature. It naturally appears in compounds, which contain cobalt and was mainly used to color glasses (cobalt-blue). Its name has been derived from the Latin word *cobaltum*, which means *goblin*, since at the time of its discovery people believed it to be jinxed. Today it is used in alloys for different kind of purposes. At room temperature

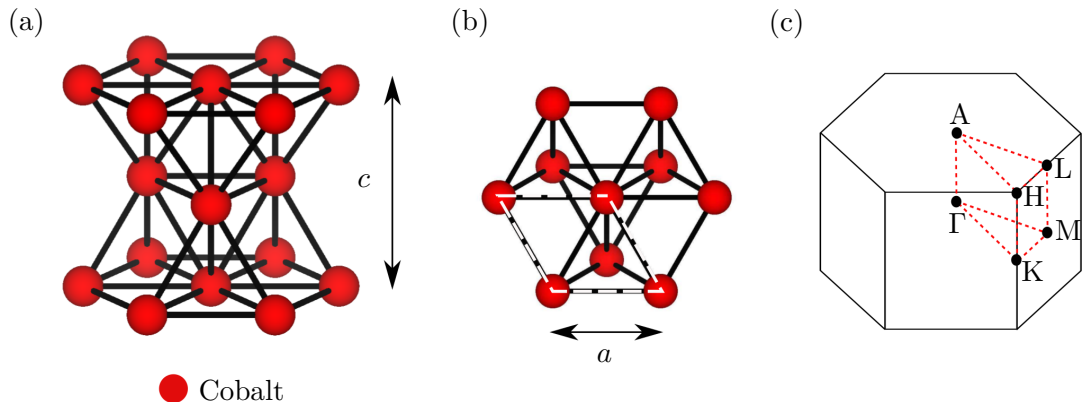

FIG. 2.9: Unit cell and First Brillouin Zone of cobalt. (a) 3D-representation of the hcp-lattice and (b) corresponding top view with lattice constants $a = 2.507$ Å and $c = 4.069$ Å. One unit cell is emphasized by the dashed line. (c) First Brillouin Zone of the reciprocal lattice. Γ, M, K, A, H, L are six non-equivalent high symmetry points.

cobalt crystallizes in a hexagonal-closed-packed (hcp) lattice. The lattice constants are $a = 2.507$ Å and $c = 4.069$ Å, see Fig. 2.9. Cobalt has a magnetic moment of roughly $\mu = 1.6 - 1.7\ \mu_B$ per atom [70]. The electronic configuration of cobalt is [Ar] $3d^7 4s^2$ and thus has 9 valence electrons.

The fact that the lattice constant of hcp-cobalt is close to the one of graphene and hBN makes it a perfect candidate to form heterostructures, since only a small mismatch needs to be compensated and small strain should be introduced. Since cobalt is a ferromagnet, we performed open shell calculations of ground state electronic properties. From the DOS in Fig. 2.10 we can see, that states near the Fermi level are mainly formed by d orbitals. We see, that the corresponding bands cross the Fermi level, which indicates metallic character, as expected. The bands which are formed by d states are less dispersive compared to bands which originate from s states, lying low in energy.

Comparing the spin contributions to the DOS, we can see, that states with spin up are lying lower in energy than states with spin down character, making cobalt ferromagnetic. Our

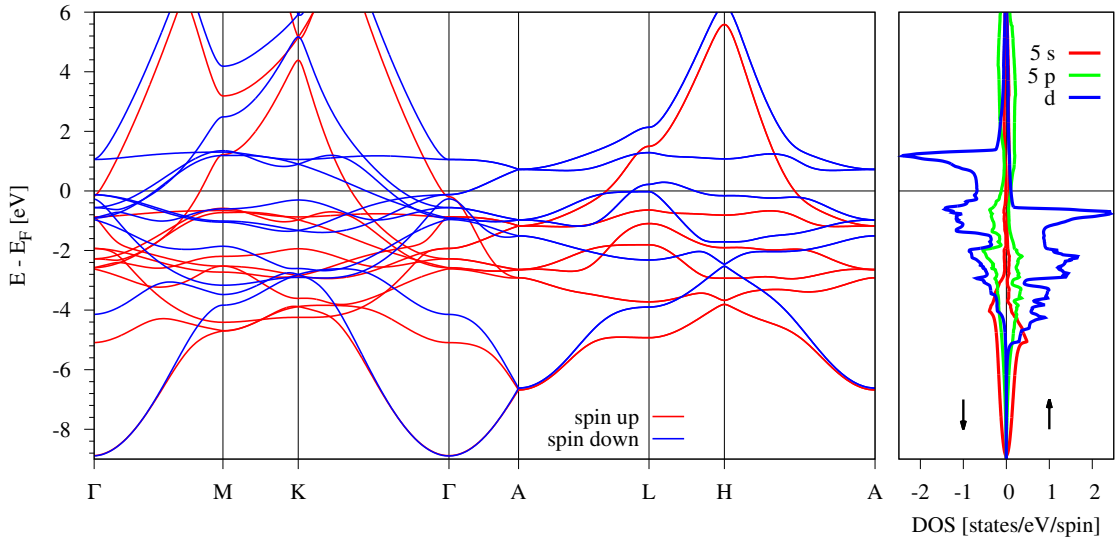

FIG. 2.10: Band structure and corresponding orbital resolved DOS of bulk hcp-cobalt. Left panel: Spin polarized band structure along the high symmetry path Γ–M–K–Γ–A–L–H–A of bulk cobalt. Spin up (down) bands are shown in solid red (blue). Right panel: Orbital and spin resolved DOS. The contributions of s and p states are increased by a factor of five. The arrows indicate different spin contributions of the DOS.

calculated value for the spin magnetic moment is $\mu = 1.63\ \mu_B$ per atom. Consequently the total magnetization per unit cell is $\mu_G = 3.26\ \mu_B$, since the hexagonal unit cell contains two atoms. The value is in agree with the predicted one. By analyzing the DOS we calculate the spin polarization, which is defined as the difference of the spin down and the spin up density normalized by the total density evaluated at the desired energy E, i.e., $p(E) = \frac{\rho_\downarrow - \rho_\uparrow}{\rho_\downarrow + \rho_\uparrow}\Big|_E$. In order to compare the two ferromagnets, we calculate the spin polarization at the Fermi level E_F to $p(E_F) \approx 67\%$. Thus ferromagnets can be used for spin injection, because the injected electrical current is spin polarized.

2.6. Nickel

Nickel is a silvery-white ferromagnetic transition metal. It is commonly found in iron meteorites, but it is still one of the rare metals on earth, usually found together with cobalt. Mainly it is used in alloys for corrosion-resistance (stainless steel) or metals directly get a nickel coating. Nickel crystallizes in a face-centered-cubic (fcc) lattice.

It has a magnetic moment of roughly $\mu = 0.6\ \mu_B$ [70]. The electronic configuration of nickel is [Ar] $3d^8 4s^2$ and thus has 10 valence electrons per atom. The expected magnetic moment should be the smallest among the three ferromagnets iron, cobalt and nickel which is indeed true, since the d shell is almost filled. In order to stack a hexagonal lattice on top of it, one needs to consider the (111)-plane, which then looks like a triangular lattice, see Fig. 2.11. The lattice constant of nickel is $a = 3.524$ Å and thus the lattice constant of the quasi hexagonal lattice of the (111)-plane is $\frac{1}{2}\sqrt{2}a = 2.492$ Å. The (111)-plane of nickel is thus a good basis in order to make heterostructures with graphene, since the lattice mismatch is small.

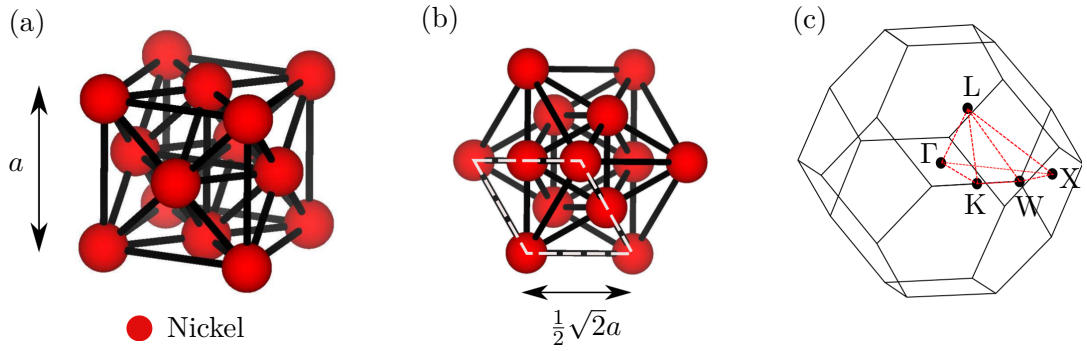

FIG. 2.11: Unit cell and First Brillouin Zone of nickel. (a) 3D-representation of the fcc-lattice, (b) (111)-plane of the fcc-lattice with lattice constant $a = 3.524$ Å. One unit cell is emphasized by the dashed line. (c) First Brillouin Zone of the reciprocal lattice. Γ, K, W, X, L are five non-equivalent high symmetry points of usual reciprocal lattice of a fcc-crystal.

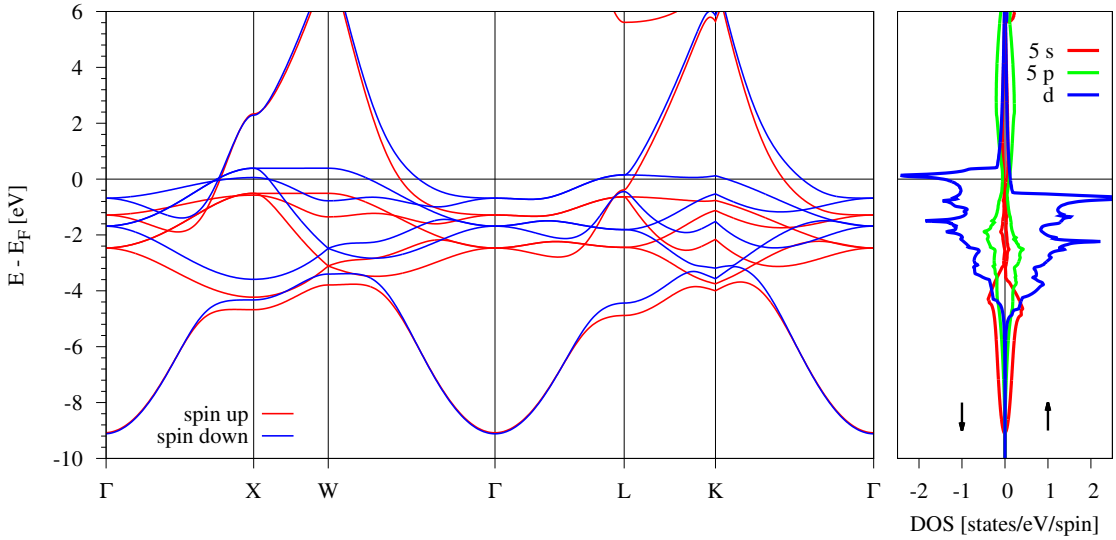

FIG. 2.12: Band structure and corresponding DOS of bulk fcc-nickel. Left panel: Spin polarized band structure along the high symmetry path Γ–X–W–Γ–L–K–Γ. Spin up (down) bands are shown in solid red (blue). Right panel: Orbital and spin resolved DOS. The contributions of s and p states are increased by a factor of five. The arrows indicate different spin contributions of the DOS.

The band structure in Fig. 2.12 for bulk nickel is calculated along the high symmetry path Γ–X–W–Γ–L–K–Γ, since the reciprocal lattice for a fcc-crystal is different from the reciprocal lattice of a hexagonal crystal; see Fig. 2.11. Our calculated value for the spin magnetic moment is $\mu = 0.64\ \mu_B$ per atom. The value is in agree with the predicted one.

We can see similarity between the band structures of cobalt and nickel. Bands near the Fermi energy are also mainly formed by d states, which cross the Fermi level, giving nickel a metallic character. The spin splitting of the bands in this case is smaller than for cobalt, leading to the smaller spin magnetic moment. The spin polarization at the Fermi level E_F is $p(E_F) \approx 80\%$, being larger than the one of cobalt, which can be directly seen by looking at the DOS.

2.7. Summary

Since we are interested in proximity induced exchange coupling in graphene, the strategy will be as follows. We take a thin film of the ferromagnet, put an insulator on top of it as the tunnel barrier, and place then graphene on top of that. The graphene/insulator/ferromagnet structures are considered in a slab geometry, where we add 15 Å of vacuum. Since the lattice constants are very different for some materials, we give here a short overview of the properties of the different materials. The DFT results for the band gap energies are in good agreement

Material	Graphene [71]	hBN [49, 72]	SiO_2 [57, 62]	Al_2O_3 [69]	Cobalt [73, 74]	Nickel [73, 74]
Lattice	hex.	hex.	trig.	rhomb.	hcp	fcc
a [Å]	2.463	2.504	4.913	4.758	2.507	3.524
c [Å]	6.712	6.66	5.405	12.98	4.069	—
E_g [eV] (EXP)	—	5.97	8.4	8.8	—	—
E_g [eV] (DFT)	—	4.681	6.008	6.291	—	—
μ [μ_B]	—	—	—	—	1.6	0.6

TAB. 2.1: Overview of the used materials with their corresponding lattices, lattice constants a, c, experimental (EXP) and calculated (DFT) band gap energies E_g for the insulators and magnetic moments μ of the ferromagnets. Lattice constants c for graphene and hBN, are for graphite and bulk hBN.

with others, see Refs. [24, 68, 75]. In comparison to the experiment, the calculated band gaps are underestimated by roughly 30%. For thin films (0.5 – 2 nm) of the insulator, the band gap is not necessarily the same as for the bulk, as can be seen in Ref. [58] for SiO_2. Later on, when we consider thin films of the ferromagnets, it can happen, that the magnetic moment is increased compared to the bulk value, as proposed in Ref. [31]. Studies on nickel revealed that surface atoms showed an increased magnetic moment of 7% compared to bulk atoms. Dealing with heterostructures is much more complicated, since we have to consider a lot of things, which influence the electronic properties of graphene. For example, the behavior of the heterostructure depends on the stacking order and thickness of the single layers. Moreover, there is always a mismatch in the lattice constant and thus we will introduce strain in the

Material combination	Graphene	Insulator	Ferromagnet	a [Å]	mismatch [%]
Gr + hBN + Co	1×1	1×1	1×1	2.489	0.83
Gr + hBN + Ni	1×1	1×1	1×1	2.480	0.75
Gr + SiO_2 + Co	2×2	1×1	2×2	4.920	0.68
Gr + SiO_2 + Ni	2×2	1×1	2×2	4.920	0.48
Gr + Al_2O_3 + Co	2×2	1×1	2×2	4.900	1.88
Gr + Al_2O_3 + Ni	2×2	1×1	2×2	4.900	1.67

TAB. 2.2: Overview of the smallest possible matchings for the lattices; given are the in-plane sizes of the required supercells. The heterostructure lattice constant a and the average lattice mismatch between the three materials and the heterostructure systems are given.

structure, by fixing a reasonable but assumed lattice constant.

In Tab. 2.1 we summarize the lattice constants, band gap energies and atomic magnetic moments for the individual bulk crystals. By matching the materials with their lattice structure and lattice constants, we are able to form vdW heterostructures on a commensurable hexagonal lattice as given in Tab. 2.2 with a mismatch of the lattices smaller than 2%. For example, graphene, hBN and cobalt match in a 1×1 unit cell with a commensurable lattice constant of $a = 2.489$ Å. The average mismatch between the heterostructure lattice constant and the single layer lattice constants is 0.83%. The smallest possible commensurable unit cell combinations are listed in Tab. 2.2.

Chapter 3

Heterostructures with hBN

There have already been several theoretical [24, 25, 28, 55, 76–83] and also experimental [27, 39, 53, 84–86] investigations based on metal/hBN, graphene/hBN or graphene/hBN/metal heterostructures. All of them reveal several striking properties, e.g. graphene grown on hBN shows a 4 times higher mobility compared to graphene grown on SiO_2 [84]. This is especially useful, when fast electron transport is necessary. Most of all for spintronics, since, even though an insulating/semiconducting substrate can induce strong proximity SOC [87, 88] and thus limit the spin lifetime in graphene, we can transport the information over a long distance before it gets lost. Investigations on graphene/hBN structures show an induced band gap of roughly 50 meV at the Dirac point in the graphene band structure, since the two carbon sublattices become inequivalent when interacting with the hBN-substrate [24]. This is useful, because we can give graphene semiconducting properties, which is especially attractive for field effect devices. When we want to make graphene applicable it is necessary to make metallic contacts. Placing graphene on a metal substrate results in doping of graphene [25], but the linear graphene dispersion can be strongly altered by a metallic substrate. Additionally experiments on ferromagnet/graphene interfaces [32, 33] show that one atom thick single layer of graphene is enough to efficiently protect ferromagnetic spin sources against oxidation and preserve the measurable spin-valve signal in agreement with theory [34, 35].

By forming graphene/insulator/ferromagnet structures, we can simultaneously protect graphene from the influence of the ferromagnet due to the insulating barrier, but exploit the magnetism offered from the ferromagnet. Thus it is crucial to investigate magnetic and spin-orbit proximity effects from ferromagnets/metals influencing graphene through an insulating layer, in detail. Investigations on structures of graphene on the ferromagnetic insulator EuO already show a tunable magnetic proximity effect leading to a spin dependent Fermi velocity v_{F}, hybridization gap and large spin polarizations of the order of 20% [38]. Experimental and theoretical investigations of Ni(111)/hBN/graphene structures [27, 39] show a very efficient spin-injection into graphene. They also find an inversion of the measured spin-valve signal due to the variation of the barrier thickness. Additionally, spins have also been successfully injected from cobalt by tunneling through oxide insulators into graphene [66].

In this section we consider graphene/hBN/ferromagnet structures to investigate the low energy physics around the graphene Dirac cone. At first, we search for the relaxed minimum energy configuration, then we calculate the physical relevant quantities like band structure and DOS and finally extract the strength of the exchange interaction by employing a low energy model Hamiltonian, which is able to describe the modified graphene band structure in the vicinity of the Dirac point.

3.1. Graphene/hBN/Cobalt

The lattice constant of graphene is $a = 2.46$ Å [45], the one of hBN [49] is $a = 2.504$ Å, slightly bigger than the one of graphene, and the one of hcp-cobalt is $a = 2.507$ Å [89]. Thus we fix an effective average lattice constant of $a = 2.489$ Å for the system, as a compromise to make the lattices commensurable and to keep the unit cell as small as possible. The lattice of graphene changes by only 1%, since we want to look at the electronic properties of graphene, especially. The main effect of a larger lattice constant is that in-plane sp^2 bonding gets weakened due to the increased distance between the atoms and thus low energy bands rise in energy. For a further analysis of the effects of the lattice constant on the electronic structure of graphene and hBN, look at appendix B.2.

Our starting point structure will be one single layer of graphene, one layer of hBN and three atomic layers of cobalt stacked on top of each other, taking the symmetry of the hexagonal lattices into account. The distance between the single layers at the beginning is $d = 3.2$ Å, assuming vdW-bonding. A vacuum spacing of 14 Å is added, to get a quasi-2D slab structure. Computational details are given in appendix B.3.

3.1.1. Lattice Structure

Initially, we need to find the minimum energy configuration of this layered structure, since there are a lot of possibilities to stack them. At first, we keep the layers of cobalt and hBN fixed on top of each other, as in Fig. 3.2(1). The distances between the layers are also kept fixed at $d = 3.2$ Å. We want to take a look at the different total energies of the system, when we change only the stacking order of graphene on top of hBN, since there are already three inequivalent possibilities; see Fig. 3.1. Of course, one could think of other possibilities, but

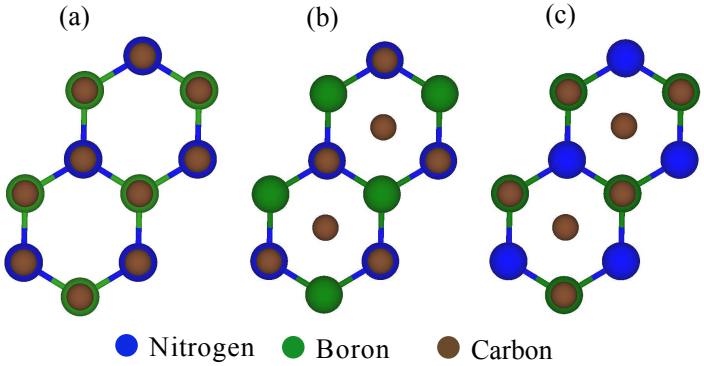

FIG. 3.1: Possible stackings of graphene on top of hBN. (a)-(c) show three inequivalent stacking possibilities of graphene on top of hBN for commensurable lattices. The vdW structure has C_{3v} symmetry.

from the symmetry point of view, these structures are favorable for commensurable lattices. The total energies and the forces for the different configurations from Fig. 3.1 are given in Tab. 3.1 where we can see that it is energetically favorable if carbon atoms are on top of boron and above the hBN-hexagon, in agreement with Ref. [24]. The forces are too high, since a relaxation of atomic positions has not been performed up to this point.

In the second step, we keep this minimum energy configuration between hBN and graphene

configuration	(a)	(b)	(c)
$E_{\text{tot}} - E_{\text{ref}}$ [meV]	-27.432	-37.248	-65.442
total force [mRy/a_0]	25.825	25.629	25.428

TAB. 3.1: Total energies of the different stacking possibilities of graphene on top of hBN with respect to the chosen reference energy $E_{\text{ref}} = -562.925$ Ry. The different configurations correspond to Fig. 3.1. The stacking of hBN on top of cobalt was configuration (1) in Fig. 3.2, which we kept fixed for these possibilities. The layer distances are fixed at $d = 3.2$ Å.

configuration	(1)	(2)	(3)	(1')	(2')	(3')
$E_{\text{tot}} - E_{\text{ref}}$ [meV]	-65.442	-67.129	-73.922	-115.13	-114.27	-74.702
total force [mRy/a_0]	25.428	25.173	24.593	22.467	22.578	24.594

TAB. 3.2: Total energies of the different stacking possibilities of hBN on top of cobalt with respect to the chosen reference energy $E_{\text{ref}} = -562.925$ Ry. The different configurations correspond to Fig. 3.2. The primed labels correspond to the same configurations, but with interchanged nitrogen and boron atoms. The stacking of graphene on hBN is configuration (c) in Fig. 3.1. The layer distances are fixed at $d = 3.2$ Å.

fixed, but take a look at the different stacking possibilities between cobalt and hBN. In general, there are again three possibilities of stacking a hexagonal structured layer on top of the hcp-cobalt for commensurable lattices, which are shown in Fig. 3.2, again taking into account the symmetry. The atoms in the unit cell of hBN are inequivalent and therefore the

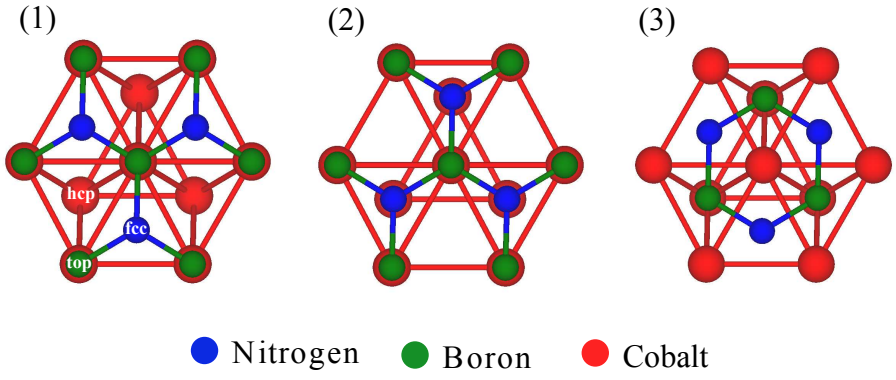

FIG. 3.2: Possible stackings of the hBN layer on top of cobalt. (1)-(3) show three inequivalent stacking possibilities for a commensurable lattice. By interchanging nitrogen and boron atoms, there are in total six possibilities.

number of possibilities doubles by interchanging nitrogen and boron atoms. From the total energies in Tab. 3.2, it seems to be crucial that the nitrogen atom is at top-site above the cobalt substrate. The boron atom can have two configurations, either fcc or hcp-site, which are very close in energy. We find that it is energetically favorable if nitrogen atoms are at top-site and boron atoms are at fcc-site above cobalt, in agreement with Refs. [28, 76, 78].

In general, three positions (top, hcp and fcc) can be distinguished within a hexagonal unit cell. Thus the different positioning possibilities of the carbon atoms above the substrate will

influence the strength of proximity magnetism. In Fig. 3.3, the energetically most favorable stacking is shown, following from our total energy analysis, where we assumed the lattices to be commensurable with the lattice constant $a = 2.489$ Å. Taking the hexagonal symmetry of the lattices into account, the vdW structure in total has C_{3v} symmetry. Since we know that hcp-cobalt is a ferromagnet, we consider open shell calculations for ground state electronic properties.

In the final step, we allow the atoms within the unit cell to relax in their z position (transverse to the layers), to find the optimized distances between the single layers. After relaxation of atomic positions we obtained layer distances of $d_{\mathrm{Co/hBN}} = 2.097$ Å between the cobalt and hBN and $d_{\mathrm{hBN/Gr}} = 3.010$ Å between hBN and graphene (measured between nitrogen and carbon/cobalt atoms, respectively, since the hBN layer is buckled) and a vacuum spacing of roughly 15 Å. The adjacent layer distances of this minimum energy

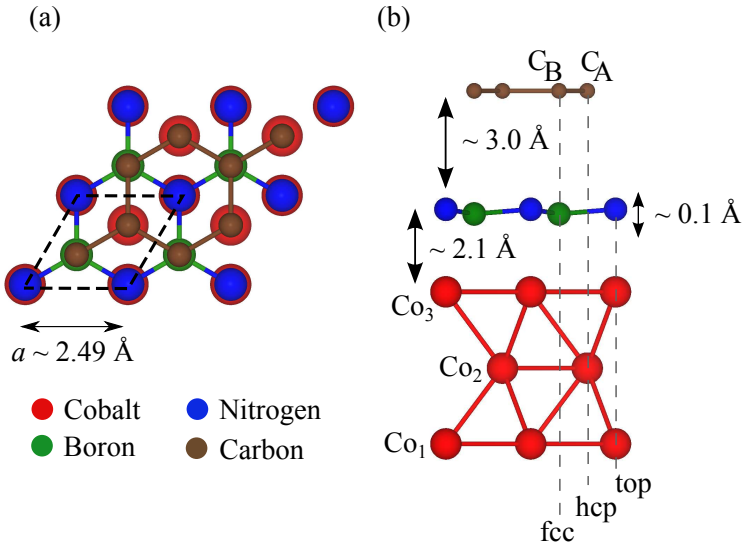

FIG. 3.3: Structure of graphene/hBN/cobalt, with labels for the different atoms. (a) Top view of the structure, with one unit cell emphasized by the dashed line. (b) Side view with stacking configuration: C_B over boron, C_A over hBN-hexagon. Nitrogen at top-sites and boron above fcc-sites of cobalt. The distances indicated are measured between graphene/cobalt and the nitrogen atom of hBN, since the hBN layer is corrugated by $\Delta z = 0.113$ Å. The boron atom is closer to the cobalt surface. Atoms Co_α, $\alpha = 1, 2, 3$ label the three cobalt layers.

configuration are in agreement with Refs. [24, 55, 90], which report $d_{\mathrm{hBN/Gr}} = 3.22 - 3.40$ Å and $d_{\mathrm{Co/hBN}} = 1.92 - 2.02$ Å. We also find, that the hBN-layer is not flat anymore but slightly buckled since the boron atom is closer to the cobalt surface by 0.113 Å compared to the nitrogen atom, in agreement with Refs. [55, 76].

It is worth to mention that the energy gain by using a spin-polarized ground state in the calculation compared to a non-polarized ground state is $\Delta E_{\text{sp-nsp}} \approx 0.7$ eV, which is very large compared to the thermal energy and cannot be neglected for the description of this system. The energy difference by changing the stacking of the atoms in the system, following from the total energies in Tabs. 3.1, 3.2, is comparable to the thermal energy $k_B T \approx 25$ meV. During the production of such layered structures, temperatures of 1000 K are common [53, 79] and thus the energetically favorable stacking cannot be predicted for sure at room temperature. Since the lattices of graphene, hBN and cobalt are incommensurable in reality, there will always be regions, where any of the mentioned stacking configurations appear.

Computationally it is very demanding to analyze incommensurable structures, since one has to consider large supercells. For graphene on hBN, moiré patterns have been observed [91, 92] for an incommensurable structure. As our results are in agreement with previous DFT calculations, the starting point for our considerations will be the structure shown in Fig. 3.3. Details of the calculations presented in the following are given in appendix B.3.

3.1.2. Effective Hamiltonian

First we want to have a look at the general band structure of the vdW system, in order to get a feeling, where the bands of our single layers come into play. In Fig. 3.4 we show the band structure divided into the two spin channels, where the different colors correspond to the different layers of the vdW heterostructure. We can see, that the bands of the individual layers are almost intact and get only slightly influenced by the other layers. Fortunately the graphene band structure, especially the linear dispersion at the K point, is preserved. Thus an effective low energy model Hamiltonian should be able to describe the dispersion in the vicinity of the K point.

Obviously hBN gets spin polarized, especially by looking at the highest lying valence band of hBN directly at the K point. From the spin up channel, we see that the maximum of

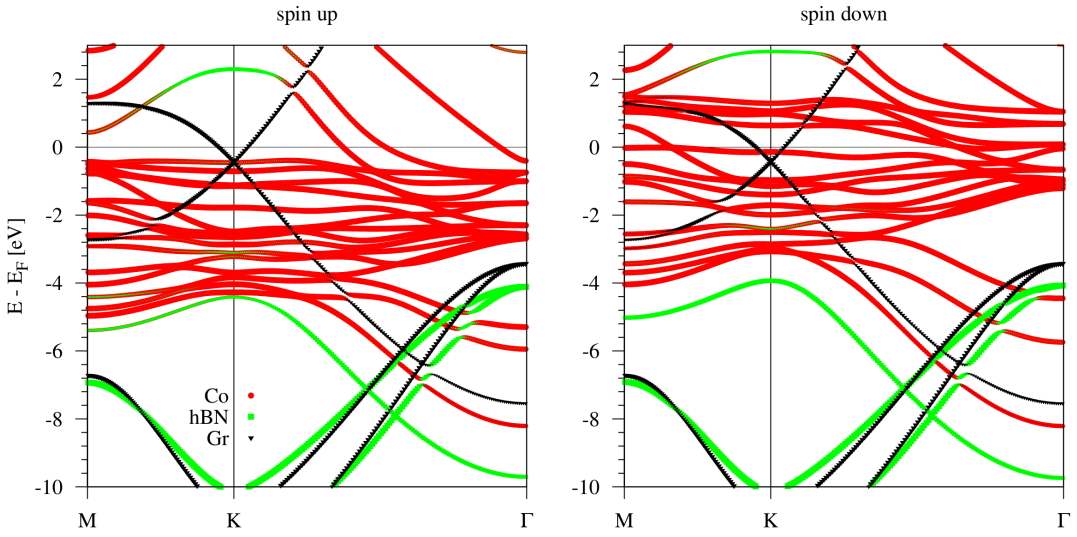

FIG. 3.4: Character plot of the spin polarized band structure of the graphene/hBN/cobalt heterostructure along the high symmetry path M–K–Γ. Left panel: Spin up character plot of the band structure. Different colors correspond to the different layers of the vdW heterostructure (red = cobalt, black = graphene, green = hBN). Right panel: Spin down character plot of the band structure.

this band is at −4.5 eV, while it is at −4 eV for the spin down channel, resulting in an exchange energy of roughly 0.5 eV. The same is true for the conduction band of hBN, which is also spin split. From the analysis of the single layer hBN, we know that the maxima of the valence bands are mainly formed by p_z orbitals, originating from the nitrogen atom. The main hybridization of hBN bands with the cobalt bands takes place near the Γ point. The d_{z^2} orbitals of cobalt hybridize with states of hBN and we can see anti-crossings of the bands in the energy window from −4 to −7 eV. Also at the K point cobalt bands show some character

of states from hBN at energies around −3 eV So indeed, the influence of cobalt on hBN is large, since the layer distance is quite small. By analyzing the cobalt bands for the different spin channels, we find an exchange energy of roughly 1.6 – 1.8 eV, which is in agreement with its atomic magnetic moment of 1.6 μ_B. The graphene π-bands are lying within the band gap of hBN, but get influenced by the cobalt d-bands lying around the Fermi level. In the following we will explicitly analyze, how the graphene bands are influenced by the cobalt bands near the Dirac point.

Two effects will play a role in this heterostructure that will influence graphene's band structure near the Dirac point. First, the influence of the substrate resulting in a small gap in the band structure of around 50 meV as for graphene/hBN structures [24] is due to the sublattice symmetry breaking. Second, due to the metal the Dirac point is shifted away from the system Fermi level because of the difference in the workfunctions of graphene and the metal, as in Refs. [24, 25]. Graphene gets either hole or electron doped, depending on the metal itself or on the applied electric field transverse to the structure [28]. As we can see in Fig. 3.4, the Dirac point of graphene is roughly $E_D \approx -0.5$ eV below the system Fermi level, making graphene electron doped. We call the energy E_D the Dirac point energy and it is a measure for the doping level. If one is interested in the real value of the doping, one would have to calculate the difference of the workfunctions of graphene and the vdW heterostructure, as has been done in Ref. [28]. From Ref. [25] we already know that, when graphene is placed on cobalt, the graphene bands are perturbed, especially the cone structure at K point is destroyed. In Fig. 3.4 we can see, that already one layer of hBN protects the Dirac cone region significantly.

Minimal p_z-model

Our main goal is to answer the question, how do hBN and the ferromagnetic substrate affect the graphene Dirac cone at K?

The band structure in Fig. 3.4 motivates us to introduce the following minimal Hamiltonian to describe the proximity induced exchange spin splitting in graphene, similarly to earlier derivations of effective Hamiltonians for the proximity SOC in graphene on transition metal dichalcogenides and on Cu(111) substrate [30, 88]. The basis of the Hamiltonian we use is *pseudospin* $\otimes$ *spin*, giving us the basis states $|A\uparrow\rangle$, $|A\downarrow\rangle$, $|B\uparrow\rangle$, and $|B\downarrow\rangle$.

Pristine graphene is described by the massless Dirac Hamiltonian $\mathcal{H}_0$ in the vicinity of K (K')

$$\mathcal{H}_0 = \hbar v_F(\tau\sigma_x k_x + \sigma_y k_y), \tag{3.1}$$

with v_F denoting Fermi velocity, k_x and k_y are the Cartesian components of the electron wave vector measured from K (K') and σ_x and σ_y are the Pauli matrices of pseudospin. Hamiltonian $\mathcal{H}_0$ describes gapless Dirac states with conical dispersion near Dirac points, with $\tau = \pm 1$ for K (K') point, shown in Fig. 3.5(a). Since graphene is on a hBN/ferromagnet substrate, the two different carbon atoms from different sublattices feel different effective potentials, which can be described by the Hamiltonian

$$\mathcal{H}_\Delta = \Delta\sigma_z s_0, \tag{3.2}$$

where σ_z is the Pauli matrix in pseudospin space, s_0 is the unit matrix in spin space and Δ is the proximity induced orbital gap. The Hamiltonian $\mathcal{H}_\Delta$ describes a mass term, which breaks

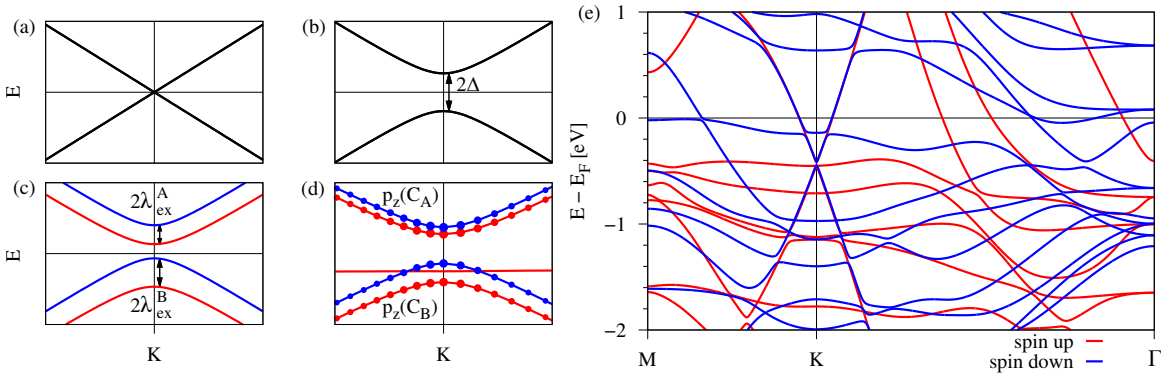

FIG. 3.5: Band structure topologies of the modified graphene Hamiltonian. (a) Band structure in the vicinity of the K point of the model graphene Hamiltonian $\mathcal{H}_0$, (b) $\mathcal{H}_0 + \mathcal{H}_\Delta$ and (c) $\mathcal{H}_0 + \mathcal{H}_\Delta + \mathcal{H}_{\text{ex}}$, with $\lambda_{\text{ex}}^{\text{A}} < \lambda_{\text{ex}}^{\text{B}} < \Delta$. The spin up (down) branch is shown in solid red (blue). (d) A zoom on the band structure of subfigure (e) of the DFT results of graphene/hBN/cobalt in the vicinity of the K point with emphasized characters of the corresponding graphene sublattice p_z orbitals, i.e. the upper (lower) two bands are formed by p_z orbitals of sublattice A (B).

the pseudospin symmetry and thus $\mathcal{H}_0 + \mathcal{H}_\Delta$ describes a gapped graphene spectrum with parabolic dispersion, shown in Fig. 3.5(b). The most crucial thing we want to investigate is the exchange splitting induced in the graphene bands by the ferromagnet. Fig. 3.5(d) shows the spin polarized band structure of graphene/hBN/cobalt near the Dirac point. To describe the proximity induced exchange splitting of the Dirac states, we introduce the Hamiltonian

$$\mathcal{H}_{\text{ex}} = \lambda_{\text{ex}}^{\text{A}} \left[(\sigma_z + \sigma_0)/2\right] s_z + \lambda_{\text{ex}}^{\text{B}} \left[(\sigma_z - \sigma_0)/2\right] s_z, \tag{3.3}$$

with $\lambda_{\text{ex}}^{\text{A}}$ and $\lambda_{\text{ex}}^{\text{B}}$ being the proximity induced exchange parameters for sublattice A and B, respectively. This term is similar to a sublattice resolved intrinsic SOC Hamiltonian [10, 12, 21, 30, 88, 93]. The dispersion of the Hamiltonian $\mathcal{H}_0 + \mathcal{H}_\Delta + \mathcal{H}_{\text{ex}}$, which should be able to describe the spin splitting of the band structure in the vicinity of the K point, is shown in Fig. 3.5(c). The minimal Hamiltonian in matrix form reads

$$\mathcal{H}_0 + \mathcal{H}_\Delta + \mathcal{H}_{\text{ex}} = \begin{pmatrix} \Delta + \lambda_{\text{ex}}^{\text{A}} & 0 & \hbar v_{\text{F}}(k_x - \mathrm{i}k_y) & 0 \\ 0 & \Delta - \lambda_{\text{ex}}^{\text{A}} & 0 & \hbar v_{\text{F}}(k_x - \mathrm{i}k_y) \\ \hbar v_{\text{F}}(k_x + \mathrm{i}k_y) & 0 & -\Delta - \lambda_{\text{ex}}^{\text{B}} & 0 \\ 0 & \hbar v_{\text{F}}(k_x + \mathrm{i}k_y) & 0 & -\Delta + \lambda_{\text{ex}}^{\text{B}} \end{pmatrix}. \tag{3.4}$$

Figure 3.5(e) shows the calculated band structure of the graphene/hBN/cobalt structure within DFT along the high symmetry path M–K–Γ in the energy window from −2 to 1 eV around the system Fermi level. Figure 3.5(d) shows a zoom around the K point of the DFT band structure, where we can see that the conduction (valence) Dirac states are mainly formed by p_z orbitals of sublattice A (B), supporting the need for a sublattice resolved exchange Hamiltonian.

The Hamiltonian $\mathcal{H}_0 + \mathcal{H}_\Delta + \mathcal{H}_{\text{ex}}$ is a minimal model using only carbon p_z orbitals, which can be used to fit the DFT-data directly at the K point and extract the pure band splittings. This Hamiltonian, we denote as the p_z-model, which is essentially useful for model charge and spin transport calculations. We would like to emphasize that the dispersion of the minimal p_z-model Hamiltonian in Fig. 3.5(c) is already very similar to the first-principles dispersion

in the vicinity of the Dirac point in Fig. 3.5(d).

The parameters Δ, $\lambda_{\mathrm{ex}}^{\mathrm{A}}$ and $\lambda_{\mathrm{ex}}^{\mathrm{B}}$ and the band splittings at the K point are related as follows for the p_z-model: splitting of the conduction bands $\Delta E_{\mathrm{cond}} = |2\lambda_{\mathrm{ex}}^{\mathrm{A}}|$, splitting of the valence bands $\Delta E_{\mathrm{val}} = |2\lambda_{\mathrm{ex}}^{\mathrm{B}}|$, and hybridization gap $\Delta E_{\text{cond-val}} = |2\Delta|$ as shown in Figs. 3.5(b),(c). The Dirac point is shifted in energy with respect to the system Fermi level, as can be seen in Fig. 3.5(e). The Dirac point energy E_{D}, defined for the p_z-model is calculated by averaging the four DFT-energies coming from the graphene Dirac bands at the K point and it will be our measure for the doping level.

Extended p_z-d-model

As we consider ferromagnetic substrates, flat bands originating from d orbitals are positioned around the Fermi energy. In the interesting range of energies near the Dirac point, p_z states of graphene hybridize with the d states, depending on their energetic position in the band structure. Similar effects occur in graphene on Cu(111) substrate [30], for example. When these d orbitals hybridize with p_z carbon orbitals in graphene, the effective exchange coupling gets strongly modified. Figure 3.5(e) shows that in the energy window of ± 400 meV from the Dirac point, three bands are interacting (crossing) with the Dirac states.

In order to capture the hybridization quantitatively, we add an additional ferromagnet Hamiltonian $\mathcal{H}_{\mathrm{FM}}$ to our model consisting of three d bands, which describes the hybridization of the ferromagnet d bands with the graphene states. The full effective Hamiltonian $\mathcal{H}_{p_z\text{-}d} = \mathcal{H}_0 + \mathcal{H}_\Delta + \mathcal{H}_{\mathrm{ex}} + \mathcal{H}_{\mathrm{FM}}$ in matrix form reads

$$\mathcal{H}_{p_z\text{-}d}= \begin{pmatrix} \tilde{\Delta}+\tilde{\lambda}_{\mathrm{ex}}^{\mathrm{A}} & 0 & \hbar v_{\mathrm{F}}(k_x - \mathrm{i}k_y) & 0 & \mathrm{u}_{\uparrow}^{\mathrm{A}} & \mathrm{v}_{\uparrow}^{\mathrm{A}} & \mathrm{w}_{\uparrow}^{\mathrm{A}} \\ 0 & \tilde{\Delta}-\tilde{\lambda}_{\mathrm{ex}}^{\mathrm{A}} & 0 & \hbar v_{\mathrm{F}}(k_x - \mathrm{i}k_y) & \mathrm{u}_{\downarrow}^{\mathrm{A}} & \mathrm{v}_{\downarrow}^{\mathrm{A}} & \mathrm{w}_{\downarrow}^{\mathrm{A}} \\ \hbar v_{\mathrm{F}}(k_x + \mathrm{i}k_y) & 0 & -\tilde{\Delta}-\tilde{\lambda}_{\mathrm{ex}}^{\mathrm{B}} & 0 & \mathrm{u}_{\uparrow}^{\mathrm{B}} & \mathrm{v}_{\uparrow}^{\mathrm{B}} & \mathrm{w}_{\uparrow}^{\mathrm{B}} \\ 0 & \hbar v_{\mathrm{F}}(k_x + \mathrm{i}k_y) & 0 & -\tilde{\Delta}+\tilde{\lambda}_{\mathrm{ex}}^{\mathrm{B}} & \mathrm{u}_{\downarrow}^{\mathrm{B}} & \mathrm{v}_{\downarrow}^{\mathrm{B}} & \mathrm{w}_{\downarrow}^{\mathrm{B}} \\ \mathrm{u}_{\uparrow}^{\mathrm{A}} & \mathrm{u}_{\downarrow}^{\mathrm{A}} & \mathrm{u}_{\uparrow}^{\mathrm{B}} & \mathrm{u}_{\downarrow}^{\mathrm{B}} & E_{\mathrm{u}} & 0 & 0 \\ \mathrm{v}_{\uparrow}^{\mathrm{A}} & \mathrm{v}_{\downarrow}^{\mathrm{A}} & \mathrm{v}_{\uparrow}^{\mathrm{B}} & \mathrm{v}_{\downarrow}^{\mathrm{B}} & 0 & E_{\mathrm{v}} & 0 \\ \mathrm{w}_{\uparrow}^{\mathrm{A}} & \mathrm{w}_{\downarrow}^{\mathrm{A}} & \mathrm{w}_{\uparrow}^{\mathrm{B}} & \mathrm{w}_{\downarrow}^{\mathrm{B}} & 0 & 0 & E_{\mathrm{w}} \end{pmatrix} \tag{3.5}$$

where E_j, $j = \mathrm{u,v,w}$ are the energies that correspond to the ferromagnet d states (with the spin specified by the DFT calculation), which interact with the Dirac states, and $j_{\uparrow,\downarrow}^{\mathrm{A,B}}$ are the effective hybridization parameters with the corresponding Dirac state, where the subscript (superscript) indicates the spin (pseudospin) state.

The proximity exchange ($\tilde{\lambda}_{\mathrm{ex}}$) and orbital gap ($\tilde{\Delta}$) parameters are in principle different from those of the minimal p_z-model Hamiltonian as they are renormalized due to the hybridization. The hybridization parameters vanish, if the Dirac states directly at K are reasonably far away from the ferromagnet d bands and an interaction does not affect them. As soon as the Dirac states at K are close to a d band or the hybridization is so large that it affects the spin splitting of the Dirac states, we can describe the hybridization with the corresponding interaction parameter. The full effective Hamiltonian $\mathcal{H}_{p_z\text{-}d}$ will be denoted as the p_z-d-model, and in the energy window of roughly ± 150 meV from the Dirac point energy, the band structure can be well described by this model, see Figs. 3.8 and 3.9. The p_z-d-model is of essential value for the description of the hybridization between the d bands with the graphene Dirac states, which can significantly enhance the effective proximity exchange splitting, as we

will discuss later. Like the minimal p_z-model, the p_z-d-model has to be shifted in energy, to match the DFT data and we call this energy E_0, which is an analog of E_D.

3.1.3. Results

One hBN layer

We start with presenting the results on the graphene/hBN/cobalt structure from Fig. 3.3, where we considered three layers of cobalt and one layer of graphene and hBN, respectively. From the spin and orbital resolved DOS in Fig. 3.6, we can see that the contributions to the DOS from spin up and spin down channels of boron and nitrogen are not equal. Indeed,

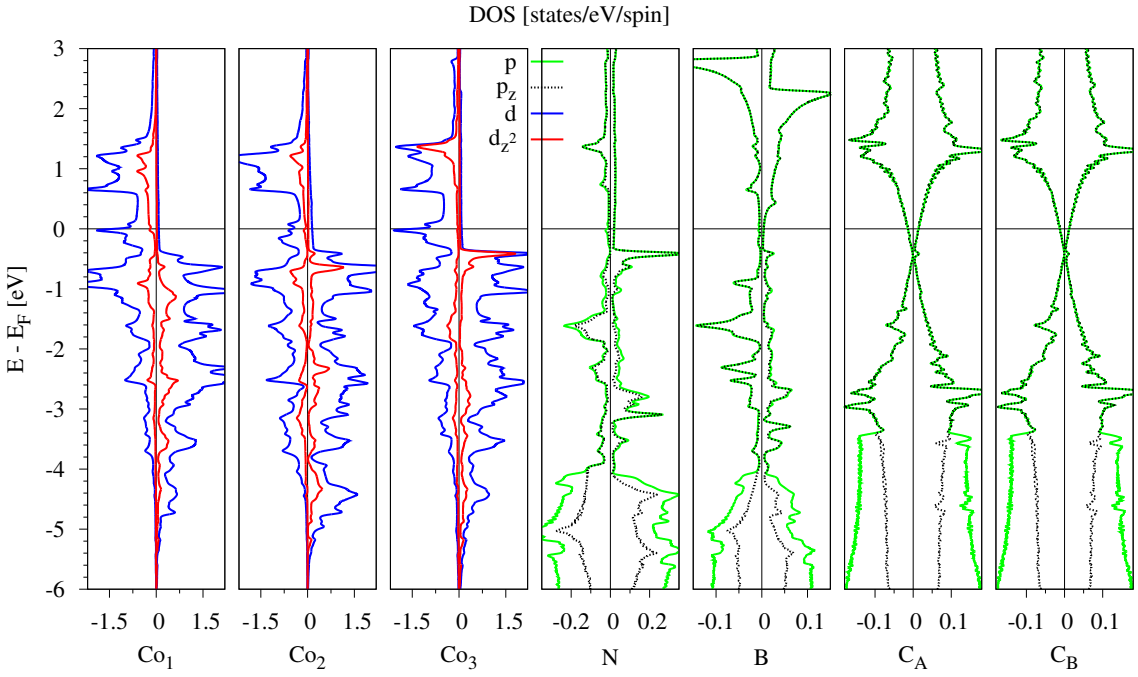

FIG. 3.6: Orbital and spin resolved DOS of all the atoms contained in one unit cell of the graphene/hBN/cobalt heterostructure. Atoms Co_α, $\alpha = 1, 2, 3$, which are ordered from vacuum to interface with hBN, label the cobalt layers as shown in Fig. 3.3(b). $\mathrm{C_A}$ and $\mathrm{C_B}$ correspond to the two different sublattices, where $\mathrm{C_B}$ is the one above the boron atom. Positive (negative) value of the DOS corresponds to spin up (down) and different colors correspond to projections on different orbitals.

boron shows a magnetic moment of $-0.04\ \mu_\mathrm{B}$ and nitrogen shows a magnetic moment of $0.02\ \mu_\mathrm{B}$. The ferromagnetic exchange of hBN with cobalt happens mainly in the energy window from -5 to 0 eV, as there can be strong interaction with the d orbitals from the ferromagnet. We have already seen that the exchange energy of the highest lying valence band of hBN is roughly 0.5 eV, induced by proximity magnetism from the cobalt. It is not really surprising that hBN gets polarized by the cobalt, since the nitrogen atoms sit directly on top of the cobalt atoms, see Fig. 3.3, maximizing the overlap of the orbitals. Especially we see that, if the d_{z^2} contribution to the DOS of Co_3 has a maximum, the p_z orbitals dominate the DOS of nitrogen. A clear band gap cannot be identified anymore in the DOS of hBN, in contrast to pristine hBN, since the electronic states of graphene and the ferromagnetic

substrate extend over the band gap of hBN.

The two carbon atoms C_A and C_B do not seem to get polarized at all from the DOS. However, cobalt induces a small positive spin magnetic moment in both carbon atoms of roughly 4×10^{-4} μ_B. Especially in the energy window between -2 to 0 eV, we can see an imbalance in the carbon DOS of the two spin channels. In this energy window also the DOS of hBN shows a strong imbalance coming from p_z orbitals, indicating the proximity nature of the polarization of Dirac states. The Dirac point of graphene is now located at roughly -0.5 eV below the system Fermi level, where we can see a very small peak in the spin up density of both carbon atoms, in contrast to pristine graphene. We also note that at this energy there is a large spin up contribution from p_z orbitals of nitrogen and from d_{z^2} orbitals of Co_3.

The cobalt atoms, of course, possess a magnetic moment, but there are deviations among them. The different atoms Co_1, Co_2, and Co_3 have magnetic moments of 1.71 μ_B, 1.59 μ_B, and 1.51 μ_B, and deviate from the bulk value of 1.66 μ_B. The magnetic moment of the cobalt atoms decreases from the vacuum side to the interface with hBN. Cobalt d states are localized in the energy window from -6 to 2 eV around the Fermi level.

Fig. 3.7 shows the spin polarized band structure with characters of the d orbitals of the different cobalt atoms Co_α, $\alpha = 1, 2, 3$. We can see, that mainly one of Co_3 spin up bands is

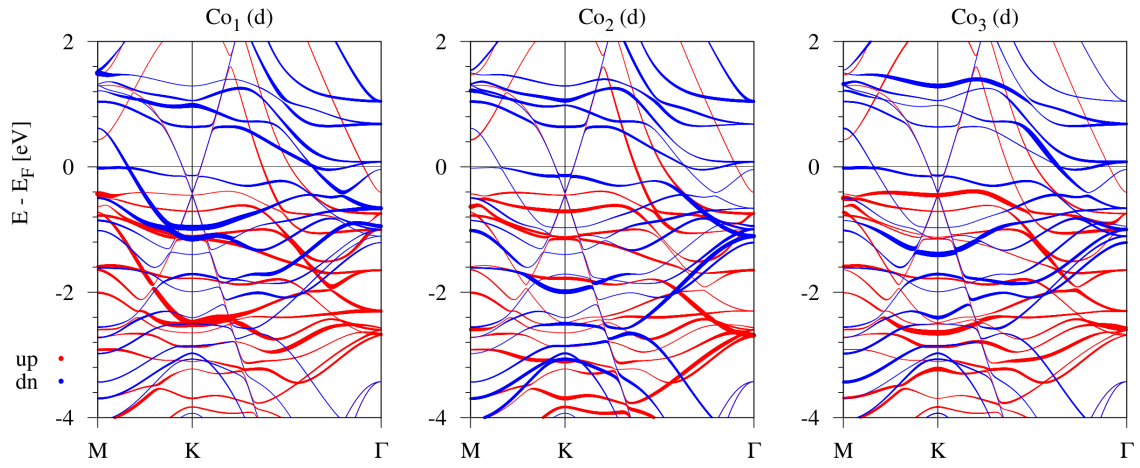

FIG. 3.7: Spin polarized band structure of graphene/hBN/cobalt heterostructure with character of the d orbitals of the different cobalt atoms Co_α, $\alpha = 1, 2, 3$. Spin up (down) bands are shown in solid red (blue). Thickness of the bands are weighted with the d orbital character of the individual cobalt atoms, corresponding to the three layers in Fig. 3.3(b).

located at the Dirac point. By further investigation, one can see that this band represents the highest lying spin up d band of cobalt and is mainly formed by its d_{z^2} orbital, as indicated in Fig. 3.8, which has a similar shape as a p_z orbital. The effective overlap of the cobalt d_{z^2} and the carbon p_z orbital can be large, giving a main contribution to the transport perpendicular to the vdW heterostructure.

In addition, two bands of Co_2 are located near the Dirac point energy. The lower spin up band is also formed by the d_{z^2} orbital, while the upper spin down band is formed by a combination of $d_{x^2-y^2}$ and d_{xy} orbitals, with its spin up counterpart at roughly -1.7 eV below the system Fermi level. What can also nicely be seen is the intrinsic exchange splitting of cobalt of roughly 1.6 eV, especially if we look at the Γ point. As expected, mainly cobalt

atoms Co_2 and Co_3 from the interface side with hBN influence the Dirac states at the K point, while the d bands from the cobalt atom Co_1 at the vacuum side are lying more far away from the Dirac point. Moreover, we notice a window in energy between 0 and 0.5 eV at the K point, where no d bands are located. By an external electric field, one could shift the Dirac point to this *free* energy window such that the graphene Dirac bands will not be crossed by any d bands and thus the band splittings at the K point will not get influenced by hybridization with d bands.

Since we are interested in the proximity induced exchange spin splitting in graphene, we fit our effective model Hamiltonians to the DFT calculated band structure, to get representative parameters for our structures. Fig. 3.8(a) shows the spin polarized band structure of the graphene/hBN/cobalt heterostructure for one layer of hBN. The graphene Dirac states for

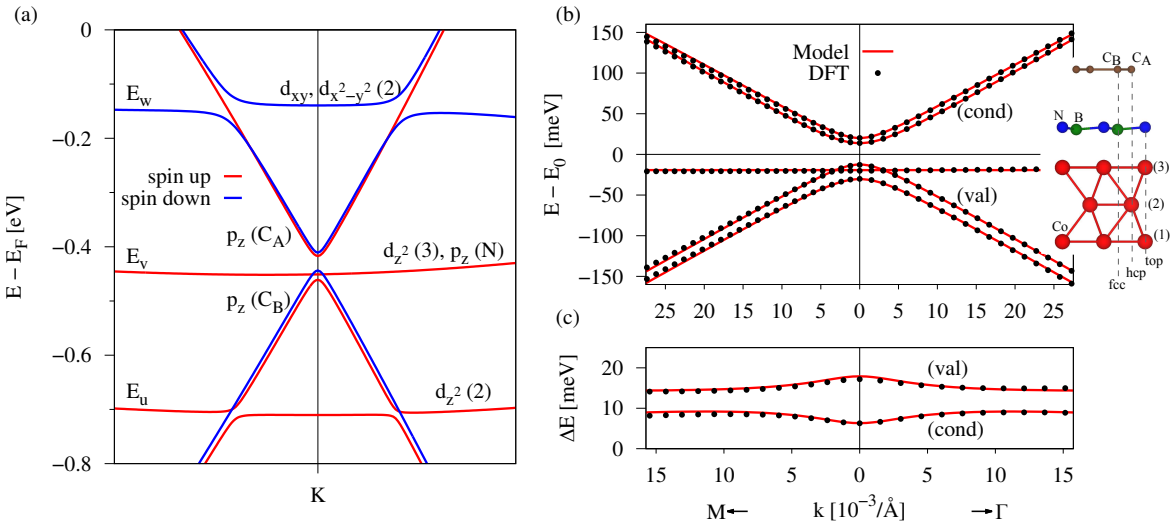

FIG. 3.8: Spin polarized band structure of graphene/hBN/cobalt heterostructure for one layer of hBN. (a) Band structure in the vicinity of the Dirac point with labels for the main orbital contributions from which the individual bands are formed, e.g. $d_{z^2}(3)$ corresponds to the d_{z^2} orbital of cobalt atom Co_3 from Fig. 3.3(b). Labels E_j, j = u,v,w are the energy bands, which correspond to the cobalt d states used to fit the p_z-d-model Hamiltonian in Eq. (3.5). The energies E_j, in Eq. (3.5), are measured with respect to the energy E_0. (b) The fit to the p_z-d-model with a side view of the structure. First principles data (dotted lines) are well reproduced by the p_z-d-model (solid lines). (c) The corresponding splittings of the valence (val) and conduction (cond) Dirac states of graphene. The main fit parameters are $E_0 = -430.89$ meV, $\tilde{\Delta} = 21.45$ meV, $\tilde{\lambda}^{\mathrm{A}}_{\mathrm{ex}} = -7.63$ meV, $\tilde{\lambda}^{\mathrm{B}}_{\mathrm{ex}} = 8.95$ meV, $E_{\mathrm{u}} = -279.41$ meV, $E_{\mathrm{v}} = -19.37$ meV, $E_{\mathrm{w}} = 282.31$ meV, $\mathrm{w}^{\mathrm{A}}_{\downarrow} = 48.44$ meV. The most relevant parameters are obtained, by minimizing the difference between the model and the DFT data for a fitting range from K towards Γ point for k points up to 20×10^{-3}/Å. By performing the fit towards M point, one would obtain slightly different parameters, at maximum deviating by 5%. From the band structure and from the fact that we limit our fitting range, we find that no additional hybridization parameters $j^{\mathrm{A,B}}_{\uparrow,\downarrow}$ are necessary to fit our band structure, except for the mentioned ones. The Fermi velocity to match the slope away from K point is $v_{\mathrm{F}} = 0.812 \times 10^6 \frac{\mathrm{m}}{\mathrm{s}}$, which corresponds to a nearest-neighbor hopping parameter of $t = 2.48$ eV, slightly smaller than the commonly used value of 2.6 eV [10, 12, 21], due to the larger lattice constant used here.

spin up are lying lower in energy than the spin down ones. The Dirac point energy is below the system Fermi level, corresponding to electron doping of graphene, since the Fermi level

crosses now the conduction band of graphene. This shift is induced by the metal as suggested in Ref. [25]. The cobalt bands hybridize with the graphene states in the vicinity of the K point and introduce exchange splitting. From the band structure in Fig. 3.8 we see that the linear dispersion of graphene is preserved. In addition, a gap forms and the spin degeneracy of the Dirac states gets lifted, allowing for semiconducting properties along with the usage of different spin channels by appropriate experimental setups. By comparing our DFT results to the p_z-d-model Hamiltonian $\mathcal{H}_{p_z\text{-}d}$, Eq. (3.5), we obtain the parameters given in Tab. 3.3, for cobalt as the ferromagnet and one layer of hBN. The fit of the p_z-d-model is shown by solid lines in Fig. 3.8(b) and agrees very well with the DFT data. The gap in the dispersion is found to be roughly 40 meV, while the band splittings are of the order of 10 meV, for one layer of hBN. We additionally employ our p_z-model valid directly at the K point. The parameters for the p_z-model are given in Tab. 3.4 and do not deviate much from the values obtained by the p_z-d-model, due to the rather weak influence of the hybridization of the d orbitals with the graphene Dirac states at the K point.

Two hBN layers

Figure 3.9 shows the calculated band structure and the fit to the p_z-d-model in the case of two layers of hBN and three layers of cobalt. The inset in Fig. 3.9(b) shows the geometry for two layers of hBN. The relative position of carbon atom C_A to hBN is not changed, while

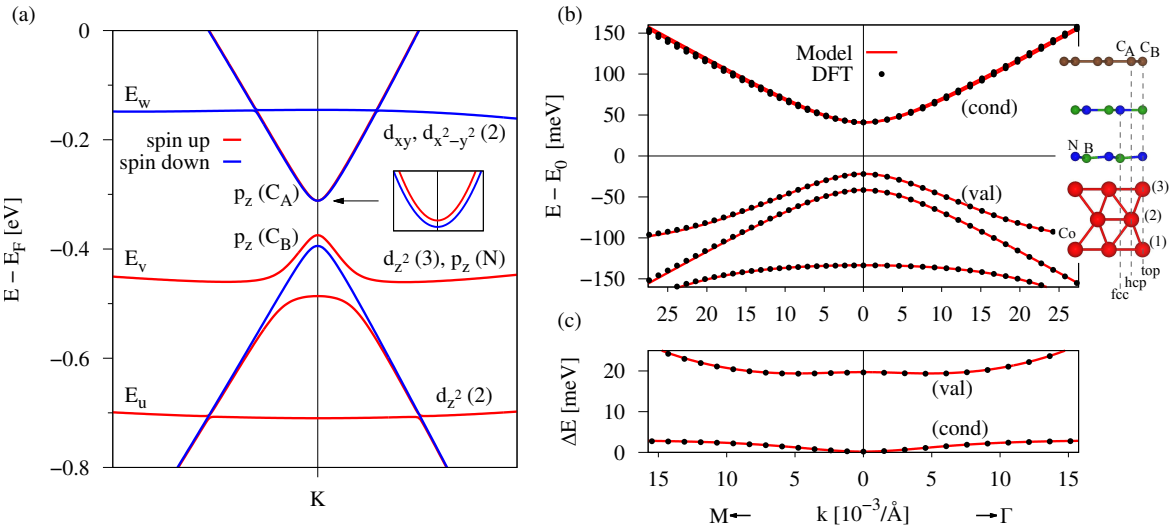

FIG. 3.9: Spin polarized band structure of graphene/hBN/cobalt heterostructure for two layers of hBN (AA' stacking). (a) Band structure in the vicinity of the Dirac point with labels for the main orbital contributions. Inset shows a zoom on the conduction Dirac states to visualize the reversal of the spin states. (b) The fit to the p_z-d-model with a side view of the structure for two layers of hBN. DFT data (dotted lines) are well reproduced by the p_z-d-model (solid lines). (c) The corresponding splittings of the valence and conduction Dirac states. The fit parameters are $E_0 = -352.65$ meV, $\tilde{\Delta} = 41.02$ meV, $\tilde{\lambda}^{\mathrm{A}}_{\mathrm{ex}} = 0.096$ meV, $\tilde{\lambda}^{\mathrm{B}}_{\mathrm{ex}} = -0.512$ meV, $E_{\mathrm{u}} = -357.12$ meV, $E_{\mathrm{v}} = -114.75$ meV, $E_{\mathrm{w}} = 207.34$ meV, $\mathrm{v}^{\mathrm{B}}_{\uparrow} = 41.67$ meV. The Fermi velocity to match the slope away from K point is $v_{\mathrm{F}} = 0.820 \times 10^6 \frac{\mathrm{m}}{\mathrm{s}}$. All other parameters are zero for the same fitting range as for the one layer case.

the position of the atom C_B is changed such, that it is again on top of the uppermost boron atom, which is the energetically favorable situation for graphene on hBN. The conduction

(valence) Dirac states are still formed by sublattice A (B), even though C_B has changed its position within the unit cell. The layer distance between the two hBN layers was relaxed to $d_{\mathrm{hBN/hBN}} = 2.977$ Å and the distance between the uppermost hBN layer and graphene is $d_{\mathrm{hBN/Gr}} = 3.114$ Å in the two hBN layer case. The corrugation of the lower hBN and the distance between hBN and cobalt did not change. Fig. 3.9(a) shows the spin polarized band structure of graphene/hBN/cobalt for two layers of hBN. In the band structure, now the spin up graphene Dirac states are no longer lying lower in energy than the spin down ones, leading to reversal of the sign of the exchange parameters $\lambda_{\mathrm{ex}}^{\mathrm{A}}$ and $\lambda_{\mathrm{ex}}^{\mathrm{B}}$. The band structure shows, that the doping level decreases by roughly 80 meV and the hybridization with the d band with energy E_{v}, coming from the top-cobalt layer, is strongly enhanced, in contrast to the case with one hBN layer. The fit to the p_z-d-model is shown by solid lines to the DFT data in Fig. 3.9(b) and the obtained parameters are given in Tab. 3.3 for cobalt as the ferromagnet and two layers of hBN. In Fig. 3.9(c) we can see that the band splitting at the K point for the conduction (valence) bands is smaller (larger) compared to the one hBN layer case. In addition, the proximity induced gap nearly doubles, and the hybridization to the d_{z^2} band originating from Co_3 is much stronger.

The inset in Fig. 3.9(b) shows that for the case of two hBN layers, carbon atom C_B (now in top position) has a direct connection to the cobalt atom in top position via a nitrogen and a boron atom of the two individual hBN layers. Localized at this cobalt atom Co_3 in top position, there is some density with d_{z^2} character (resulting in the band with energy E_{v}), which can propagate through this direct path and polarizes carbon atom C_B. This hybridization is described with the parameter $\mathrm{v}_{\uparrow}^{\mathrm{B}}$, shifting the coupled bands in energy and leading to the opening of a hybridization gap in the band structure, which also enhances the band splitting at the K point. The vertical stacking of the atoms facilitates the hybridization of the carbon p_z states with cobalt d states. For the case of one hBN layer there is no direct path connecting cobalt atoms in top-position and carbon atoms C_B and thus the hybridization is suppressed. Again, by employing our p_z-model directly at the K point, we can extract parameters, which correspond to the pure splittings of the Dirac bands at the K point, corresponding to the values of the splittings in Fig. 3.9(c). The values of $\tilde{\lambda}_{\mathrm{ex}}^{\mathrm{B}}$ and $\lambda_{\mathrm{ex}}^{\mathrm{B}}$, obtained from the two models are given in Tabs. 3.3, 3.4. They deviate by a factor of 20, which comes from the fact, that the minimal p_z-model describes dressed exchange parameters, whereas the p_z-d-model describes the bare exchange parameters. The dressed parameters contain both the interlayer exchange, as well as spin-selective hybridization of p_z and d orbitals. The bare exchange couplings $\tilde{\lambda}_{\mathrm{ex}}$ are much weaker than in the single hBN layer case, by an order of magnitude. However, the dressed coupling $\lambda_{\mathrm{ex}}^{\mathrm{B}}$ stays in magnitude similar (the sign changes). The reason is that the valence band spin splitting is dominated by the anti-crossing of $d_{z^2}(3)$ and $p_z(C_B)$ orbitals, affecting only the spin up component. The spin down valence band is not affected. As a result, the proximity spin splitting is in this case caused by shifting the spin up band relative to its spin down counterpart, by the spin-selective hybridization. *This mechanism of proximity exchange can lead to a giant enhancement of the proximity spin splittings.*

In conclusion, two mechanisms are responsible for the band splittings of the graphene Dirac states. One is the general magnetic exchange, coming from proximity magnetism of the ferromagnetic substrate, which is influenced by the barrier thickness. The thicker the barrier, the weaker is the general magnetic exchange splitting of the Dirac bands. Second, the hybridization of the graphene states with the d bands can additionally enhance the pure band splittings at the K point, as can be seen in Fig. 3.9. From the theory of magnetic interlayer coupling, we know that the interlayer exchange coupling is an oscillating function of the

spacer thickness [94, 95]. In our studies on graphene/insulator/ferromagnet structures, we observe a similar behavior in the proximity exchange.

Additional Considerations

Here we address some outstanding questions related to our above analysis. How do additional insulating layers perform? Can we control the doping level by an external electric field? Is the proximity exchange affected? Are the band splittings we see representative for a thick ferromagnetic substrate (are three Co layers enough)? How is the proximity effect affected by the Hubbard U, which shifts the d orbital levels?

In the following we consider only the dressed band splittings λ_{ex}, obtained by the minimal p_z-model directly at the K point. Bare splittings are hardly affected by electric fields, and their behavior with respect to the number of layers is that of a damped oscillator.

Dependence of the number of hBN layers. Figure 3.10 shows the dependence of the proximity gap Δ and the two exchange parameters $\lambda_{\mathrm{ex}}^{\mathrm{A}}$ and $\lambda_{\mathrm{ex}}^{\mathrm{B}}$ on the number of hBN layers between cobalt and graphene. We can see that the exchange parameters change sign by

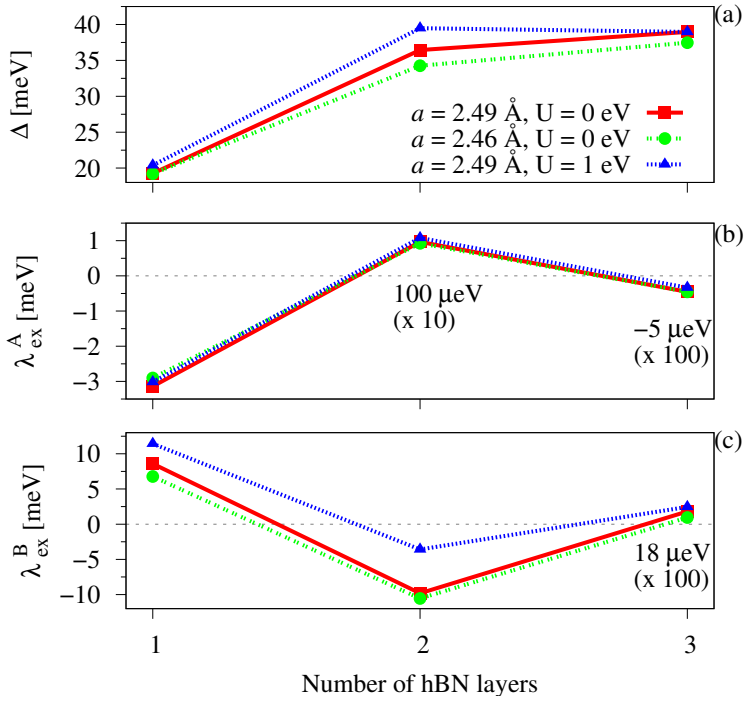

FIG. 3.10: Influence of additional number of hBN layers on the proximity induced parameters for the graphene/hBN/cobalt structure, using the p_z-model at the K point. Dependence of (a) the proximity gap Δ, (b) the exchange parameters $\lambda_{\mathrm{ex}}^{\mathrm{A}}$, and (c) $\lambda_{\mathrm{ex}}^{\mathrm{B}}$ on additional hBN layers for different lattice constants or an additional Hubbard parameter of $U = 1.0$ eV. Parameter values for 2 (3) layers of hBN were increased by a factor of 10 (100) for better visualization as indicated.

adding an additional insulating layer. The proximity gap Δ nearly doubles for two layers of hBN and stays essentially unchanged when a third layer is added, since the local environment

of graphene does not change anymore. The parameters obtained by the p_z-model are listed in Tab. 3.4 for $a = 2.489$ Å. For four layers of hBN, again the parameters change sign, but they are even smaller than for three layers of hBN and thus not included here. The parameters $\lambda_{\mathrm{ex}}^{\mathrm{A}}$ and $\lambda_{\mathrm{ex}}^{\mathrm{B}}$ are already in the μeV regime for three hBN layers, which is a result of the strong barrier. The two layer hBN case is special for the case of $\lambda_{\mathrm{ex}}^{\mathrm{B}}$, since this exchange parameter has a similar magnitude as for the single layer hBN case, due to the strong hybridization with the d orbitals close to the K point. We note that the distances for the three layer case are similar to the two layer case. We only have one additional distance between the two hBN layers directly below graphene, which was relaxed to $d_{\mathrm{hBN/hBN}} = 3.088$ Å.

As we have already seen, also the bands of hBN are spin split. To get a magnitude of the exchange splitting of the individual hBN layers, we look at the graphene/hBN/cobalt structure with three layers of hBN. In the band structure we can identify the highest (lowest) lying valence (conduction) bands, which are spin split, of the three individual layers, similar as in Fig. 3.4. From that, we extract the band splittings of conduction ΔE_{cond} and valence ΔE_{val} bands of the individual hBN layers at the K point. We notice that the spin up bands of hBN are always lying lower in energy than the spin down ones at the K point. The obtained values are especially important for people who study spin and charge transport, as well as tunneling in these kind of vdW structures. Due to the spin splitting of the bands, hBN can additionally act as a spin filter for tunneling electrons, as reported in Ref. [27].

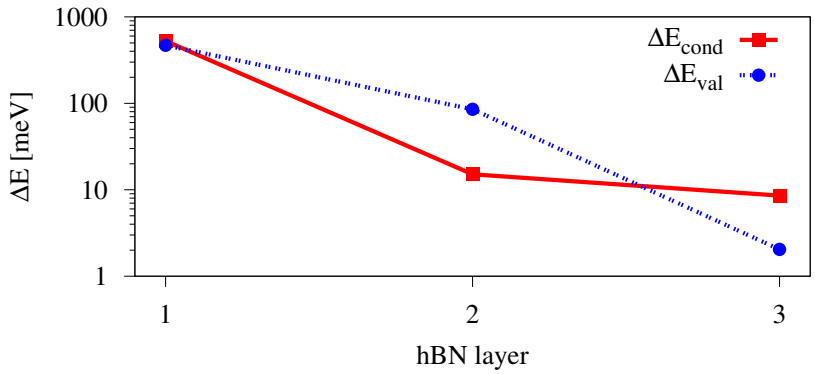

FIG. 3.11: Conduction ΔE_{cond} and valence ΔE_{val} band splittings of the three individual hBN layers at the K point. Values are obtained by identifying the spin split hBN conduction and valence bands of the three individual layers in the band structure of graphene/hBN/cobalt heterostructure for three layers of hBN. Spin up bands of hBN are always lying lower in energy than the spin down ones at the K point.

In Fig. 3.11 we show the valence and conduction band splittings at the K point of the three hBN layers. We find that the exchange splitting of the first hBN layer (closest to the cobalt surface) is roughly 0.5 eV. The splittings of the second and third layer decrease by one order of magnitude, respectively, due to the distance related decay of the proximity magnetism.

Lattice constant effects. Since we have artificially set the lattice constant for all the (well lattice matched) materials to be the same, we now consider its effect on the proximity structure. We use the graphene constant $a = 2.46$ Å, by simply changing the in-plane lattice constant of the slab to this value without changing the vertical distances between the layers, which should be more favorable for the description of the graphene dispersion. The results in

this case do not deviate much from the case with our adopted $a = 2.489$ Å, as can be seen in Fig. 3.10, but the Fermi velocity for $a = 2.46$ Å and one hBN layer is $v_F = 0.827 \times 10^6$ m/s, corresponding to a larger nearest-neighbor hopping parameter of $t = 2.56$ eV.

Hubbard U. Since the exact position of the d bands is crucial to see the giant proximity exchange in the case of two hBN layers, we consider what happens when we apply a Hubbard U parameter to the calculation, shifting the d orbital levels. From recent studies of graphene on copper [30] we know that the copper bands have to be shifted down in energy by $U = 1.0$ eV to match the measured band structure from ARPES (Angle Resolved Photo Emission Spectroscopy) experiments. From other DFT studies [96–100], mainly on metal-oxides, it is not possible to get a unique value for U. Thus, we apply $U = 1.0$ eV, as a generic representative value. The results are again in Fig. 3.10 and can be compared with the calculations without a Hubbard U parameter. We can see that the parameters Δ and λ_{ex}^{A} stay almost unchanged. However, λ_{ex}^{B}, representing the valence Dirac band splitting is strongly affected, especially in the case for two hBN layers (it is not affected for three layers). By applying the Hubbard U, we shift the band with energy E_v, in Fig. 3.9, down in energy away from the Dirac states and thus the splitting at the K point decreases. The energetic position of the d bands with respect to the Dirac point strongly influences the pure band splittings at the K point, if the hybridization is large. In the absence of experimental guidance into the exact relative position of d levels in our system, we can thus only predict the general trends and rough magnitudes for the valence proximity splitting. If the d bands are indeed close to the Dirac point, their influence will be giant, and one can expect ramifications in spin tunneling and spin injection.

Electric field effects. Figure 3.12 shows the influence of the electric field on the proximity parameters Δ, λ_{ex}^{A}, λ_{ex}^{B} and the Dirac point energy E_D. We model our electric field by a

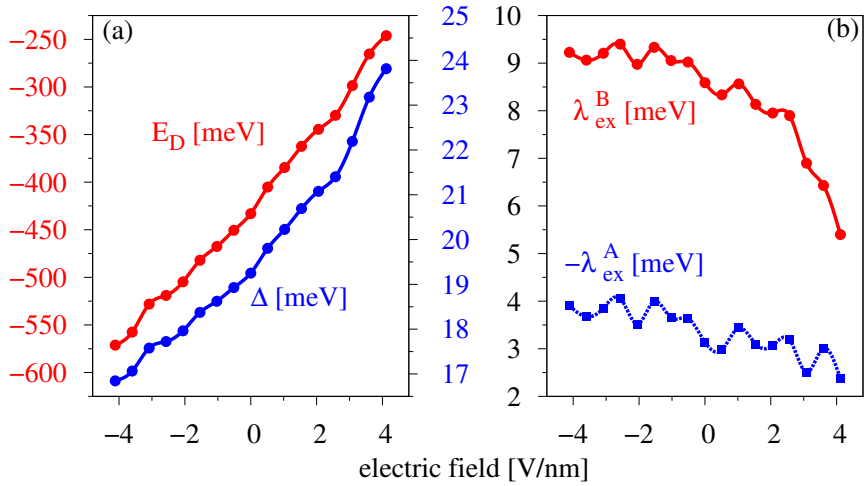

FIG. 3.12: Influence of the electric field on the proximity induced parameters for the graphene/hBN/cobalt structure for one hBN layer, using the p_z-model at the K point. Dependence of the (a) Dirac energy E_D, the proximity gap Δ, and (b) the exchange parameters λ_{ex}^{A} and λ_{ex}^{B} on the applied transverse electric field.

saw-like potential oriented perpendicular to the slab structure. A positive field points towards graphene and depletes its conduction electrons (lowers the magnitude of E_D). We can see that

E_D and Δ show the same trend with electric field. In general, by increasing the electric field the doping level decreases, i.e. one just shifts the Dirac point with respect to the Fermi level. The proximity gap Δ also increases with increasing electric field reflecting the charge transfer away from graphene. The continuous shift of the doping level with the applied electric field allows to shift the Fermi level to the desired position. The general trend of the proximity parameters is, that both tend to decrease with increasing electric field. For moderate field strengths of ±2 V/nm, the parameters and thus the band splittings at the K point are almost unaffected.

As we have seen in the two hBN layer case, the valence band splitting is strongly affected by hybridization with a d level. By applying an electric field, we can tune the energetic position

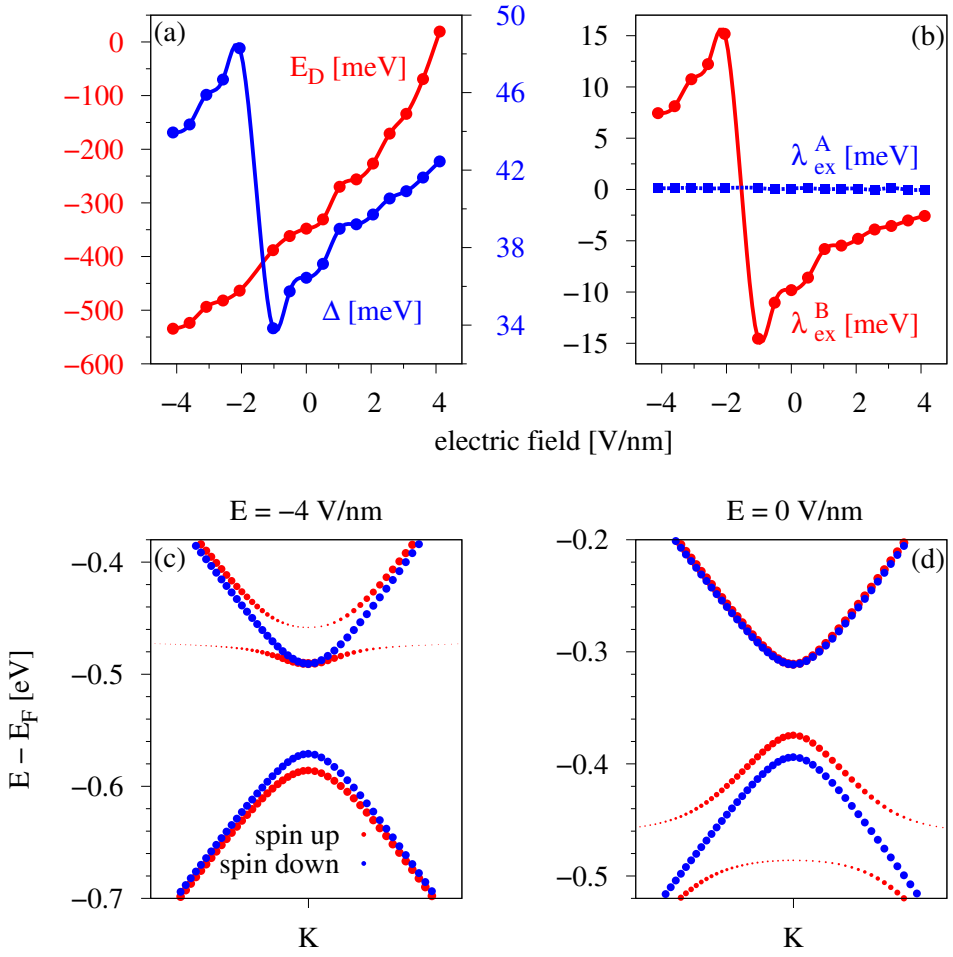

FIG. 3.13: Influence of the electric field on the proximity induced parameters for the graphene/hBN/cobalt structure for two hBN layers, using the p_z-model at the K point. Dependence of the (a) Dirac energy E_D, the proximity gap Δ, and (b) the exchange parameters λ_{ex}^A and λ_{ex}^B on the applied transverse electric field. (c) and (d) show the calculated spin resolved band structure projected on the graphene states in the vicinity of the Dirac point for two differently chosen field strengths, to visualize the reversal of the valence spin states at the K point.

of the Dirac point with respect to the d levels, which should also strongly affect the spin splitting of the graphene Dirac bands. In Fig. 3.13 we show the influence of the electric field on the proximity parameters for two layers of hBN. We can see that the Dirac point energy

E_D increases with electric field, as for the monolayer hBN case. The proximity parameter λ_{ex}^A stays roughly constant in magnitude around 100 μeV. In Figs. 3.13(c) and (d), we show the calculated spin resolved band structure of the graphene/hBN/cobalt heterostructure for two hBN layers, projected on the graphene states in the vicinity of the Dirac point for different field strengths. The spin up graphene valence band at the K point is lying lower in energy than the spin down one for $E = -4$ V/nm and vice versa for $E = 0$ V/nm. Therefore the parameter λ_{ex}^B is positive (negative) for fields smaller (larger) than roughly -1.5 V/nm, see Fig. 3.13(b). At the transition field strength of -1.5 V/nm, we cannot exactly state, whether λ_{ex}^B is positive or negative. The reason for this reversing spin states is the resonant d level. At a certain energetic configuration between Dirac point and d level, adjusted by the external electric field, the hybridization of the d level with graphene valence p_z states vanishes (for fields smaller than -1.5 V/nm) and the spin splitting changes sign. This allows to control the sign of the injected spin by applying an electric field, shifting the Dirac bands through the resonant d level. Of course, this effect can only be observed, if the d bands are indeed close to the Dirac point. Also the proximity gap Δ jumps in magnitude at the same field strength of roughly -1.5 V/nm, since the parameters Δ and λ_{ex}^B of the p_z-model are connected. Apart from the jump, the gap parameter increases with increasing field strength.

Additional cobalt layers. Finally we analyze the influence of additional cobalt layers on the band structure, see Fig. 3.14. As we increase the number of cobalt layers, also more d

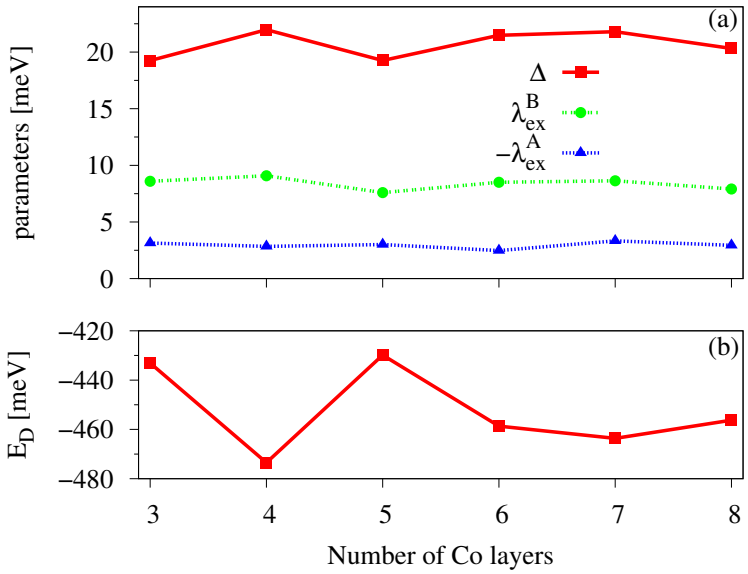

FIG. 3.14: Influence of additional number of cobalt layers on the band structure for the graphene/hBN/cobalt system for one hBN layer, using the p_z-model at the K point. Dependence of the (a) the proximity gap Δ, and the exchange parameters λ_{ex}^A and λ_{ex}^B and (b) Dirac energy E_D on additional number of cobalt layers.

bands are introduced in the dispersion. Consequently, in the vicinity of the K point in Fig. 3.5(e) graphene states can be disturbed by these additional cobalt bands. We can see that the band splittings of the graphene Dirac states at the K point do not get influenced much by additional layers, since the parameters λ_{ex}^A and λ_{ex}^B stay almost constant, but the Dirac energy, which is our measure for the doping level, seems to saturate only after 6 cobalt layers are present. We conclude that three cobalt layers suffice to obtain representative proximity

parameters, and 6 cobalt layers are needed to fix the relative positioning of the bands.

3.2. Graphene/hBN/Nickel

Similar to the approach with cobalt, we now use nickel as the ferromagnet. Nickel crystallizes in a face-centered-cubic (fcc) lattice and has a magnetic moment of roughly 0.6 μ_B, smaller than the one of hcp-cobalt which is 1.6 μ_B [101]. Thus we expect the effects of proximity induced magnetism to be smaller for the nickel substrate. In order to stack a hexagonal lattice on top of it, we consider the (111)-plane. The lattice constant of nickel [102] is $a = 3.524$ Å and thus the lattice constant of the quasi hexagonal lattice of the (111)-plane is $\frac{1}{2}\sqrt{2}a = 2.492$ Å, see Fig. 2.11.

As a result the Ni(111)-plane is suitable for making heterostructures with graphene as the lattice mismatch is small. Remember that the lattice constant of graphene is $a = 2.46$ Å [45] and the one of hBN [49] is $a = 2.504$ Å. Thus we fix an effective lattice constant of $a = 2.48$ Å for the systems with nickel, to arrange the single layers in a commensurable way. We again start with vdW-bonded layers, with $d = 3.2$ Å and a vacuum spacing of 14 Å.

3.2.1. Lattice Structure

We perform a similar total energy analysis as for the case of cobalt, again taking into account the symmetry of the hexagonal lattices. The energetically favorable stacking of graphene

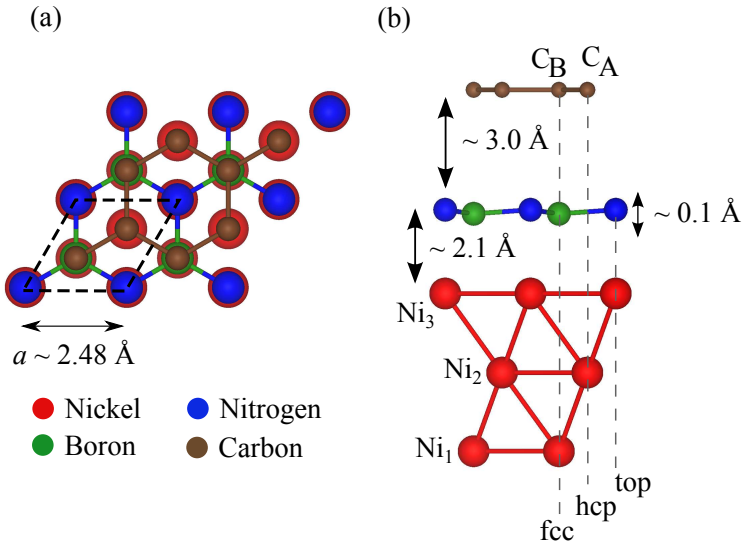

FIG. 3.15: Structure of graphene/hBN/nickel, with labels for the different atoms. (a) Top view of the structure, with one unit cell emphasized by the dashed line. (b) Side view with stacking configuration: C_B over boron, C_A over hBN-hexagon. Nitrogen at top-site above nickel and boron above fcc-site of nickel. The distances indicated are measured between graphene/nickel and the nitrogen atom of hBN, since the hBN layer is buckled by $\Delta z = 0.101$ Å, as the boron atom is closer to the nickel surface. Atoms Ni_α, $\alpha = 1, 2, 3$ label the three nickel layers.

on hBN has already been investigated in section 3.1.1. In this case, the lowest energy configuration is, when nitrogen atoms are at top-site above nickel and boron atoms are at fcc-site above nickel. Carbon atoms sit on top of boron atoms and at the hollow site, above the center of a hexagonal ring of hBN, see Fig. 3.15, in agreement with previous DFT-studies [24, 28, 55]. After relaxation of atomic positions we obtained layer distances of $d_{\mathrm{Ni/hBN}} = 2.105$ Å between the nickel and hBN and $d_{\mathrm{hBN/Gr}} = 3.015$ Å between hBN and graphene (measured between graphene/nickel and the nitrogen atoms, respectively, since the hBN layer is buckled). The layer distances of this minimum energy configuration are in agreement with Refs. [24, 55, 90], which report $d_{\mathrm{hBN/Gr}} = 3.22 - 3.40$ Å and $d_{\mathrm{Ni/hBN}} = 1.96 - 2.12$ Å. The hBN-layer is not flat anymore but slightly buckled by 0.101 Å, in agreement with Refs. [55, 76]. The vacuum in z direction for these composite systems is roughly 15 Å after relaxation in order to simulate quasi-2D systems. For hBN we use an AA' stacking (B over N, N over B), being the energetically favorable one.

In Fig. 3.16 we show the DFT calculated band structure divided into the two spin channels, where the different colors correspond to the different layers of the vdW heterostructure with one layer of hBN and three layers of nickel. We can see, that the bands of the individual

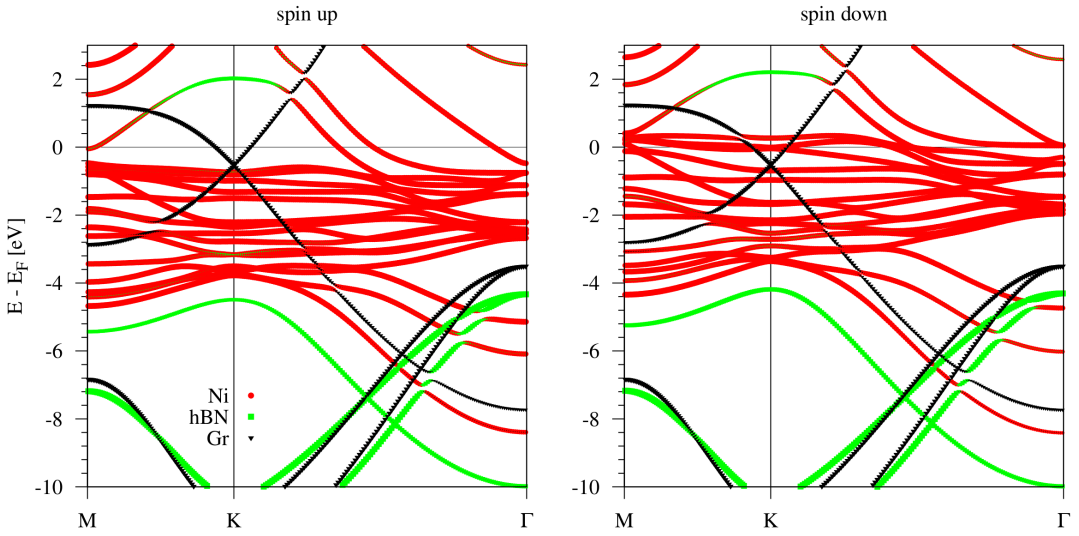

FIG. 3.16: Character plot of the spin polarized band structure of the graphene/hBN/nickel heterostructure. Left panel: Spin up character plot of the band structure. Different colors correspond to the different layers of the vdW heterostructure (red = nickel, black = graphene, green = hBN). Right panel: Spin down character plot.

layers are intact and get only slightly influenced by the other layers as for the cobalt case. The hBN layer gets spin polarized, with an exchange energy of roughly 0.3 eV of the highest lying valence band at the K point. The main influence of the ferromagnet is on the nitrogen p_z orbitals, where the overlap to the nickel d_{z^2} orbital is maximal.

The graphene π-bands are lying within the band gap of hBN, but get influenced by the nickel d-bands lying around the Fermi level. By analyzing the nickel bands for the different spin channels, we find an exchange energy of roughly 0.6 – 0.8 eV, which is in agreement with the bulk atomic magnetic moment of 0.6 μ_{B} for nickel. The band structure, Fig. 3.16, shows that our model Hamiltonian Eq. (3.5), can be used to describe the physics in the vicinity of the K point, as the linear dispersion is preserved and three d bands are located near the Dirac point energy.

3.2.2. Results

One hBN layer

We begin our analysis of the graphene/hBN/nickel heterostructure by investigating the DOS, see Fig. 3.17. There is clear similarity to the cobalt case, but also small and interesting differences. We see that the contributions from the spin channels are not equal for boron and nitrogen leading to a magnetization of these atoms. The energy window, where hBN

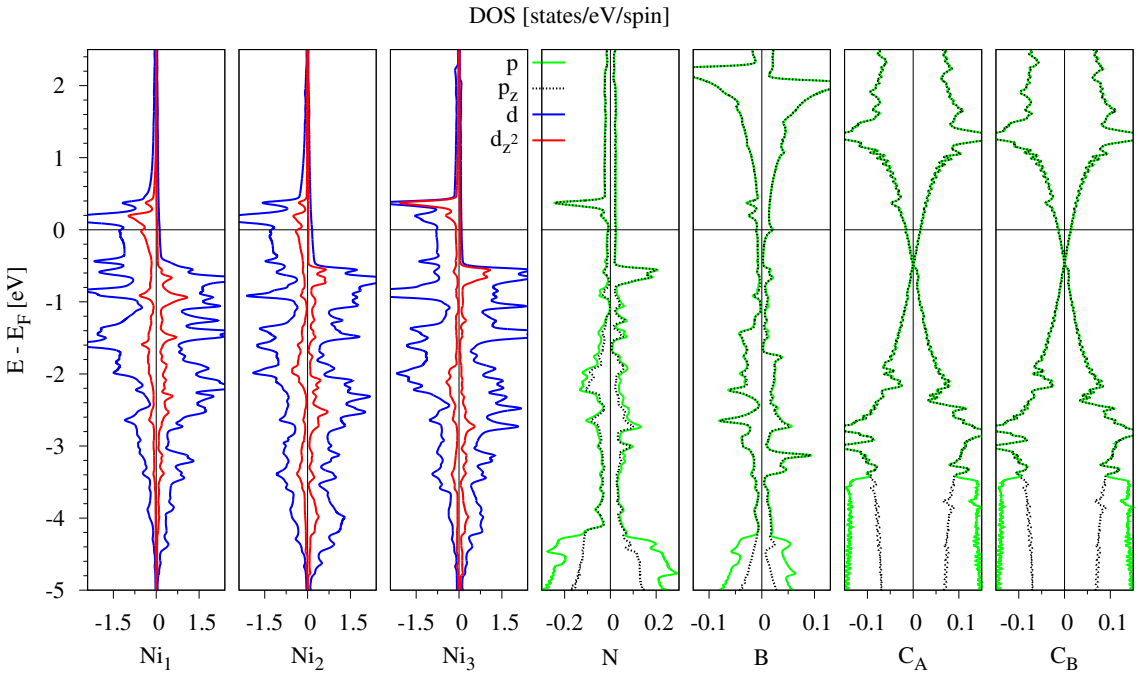

FIG. 3.17: Orbital and spin resolved DOS of all the atoms contained in one unit cell of the graphene/hBN/nickel heterostructure. Atoms Ni_α, $\alpha = 1, 2, 3$, which are ordered from vacuum to interface with hBN, label the nickel layers as shown in Fig. 3.15(b). $\mathrm{C_A}$ and $\mathrm{C_B}$ correspond to the two different sublattices, where $\mathrm{C_B}$ is the one above the boron atom. Positive (negative) value of the DOS corresponds to spin up (down) and different colors correspond to projections on different orbitals.

interacts with nickel is from -5 to 0 eV, where nickel d orbitals strongly contribute to the DOS. Consequently hBN gets polarized and the boron atom has a magnetic moment of $-0.02\ \mu_\mathrm{B}$, nitrogen has a magnetic moment of $0.03\ \mu_\mathrm{B}$. The carbon atoms get proximity polarized by the ferromagnet with a value for the magnetic moment of roughly $6 \times 10^{-4}\ \mu_\mathrm{B}$, surprisingly larger than for the case with cobalt. In an energy window around -2 eV, we can see an imbalance of the two spin channels contributing to the carbon DOS. The Dirac point is again roughly -0.5 eV below the system Fermi level, indicating electron doping of graphene. At this energy we can see a peak in the spin up DOS coming from carbon and nitrogen p_z orbitals and from the Ni_3 d_{z^2} orbitals. Additionally at the energy 0.5 eV we notice an imbalance of the two spin channels contributing to the carbon DOS, where spin down contributions of nitrogen p_z orbitals and of Ni_3 d_{z^2} orbitals are dominant. In total we see that, the d_{z^2} orbital DOS of Ni_3 has a peak at roughly ± 0.5 eV and at precisely these energies we see that nitrogen and carbon atoms show a peak in the corresponding spin channel p_z orbital DOS. The nickel atoms Ni_1, Ni_2, and Ni_3, see Fig. 3.15(b), have magnetic moments

of 0.71 μ_B, 0.70 μ_B, and 0.59 μ_B. Nickel atoms at the vacuum interface show an increased magnetic moment, while nickel atoms at the hBN interface show a smaller magnetic moment compared to the bulk value of 0.6 μ_B. Nickel d states extend in the energy window from -5 to 1 eV, which is about 2 eV narrower in comparison to the cobalt substrate due to the magnetic moment and the exchange splitting that is smaller than for cobalt.

We further analyze the origin of the bands near the Dirac energy, which are essentially states coming from the ferromagnet. Figure 3.18 shows the spin polarized band structure of graphene/hBN/nickel structure with characters for the d orbitals of the different nickel atoms Ni_α, $\alpha = 1, 2, 3$. At the Γ point we can estimate the intrinsic exchange splitting of

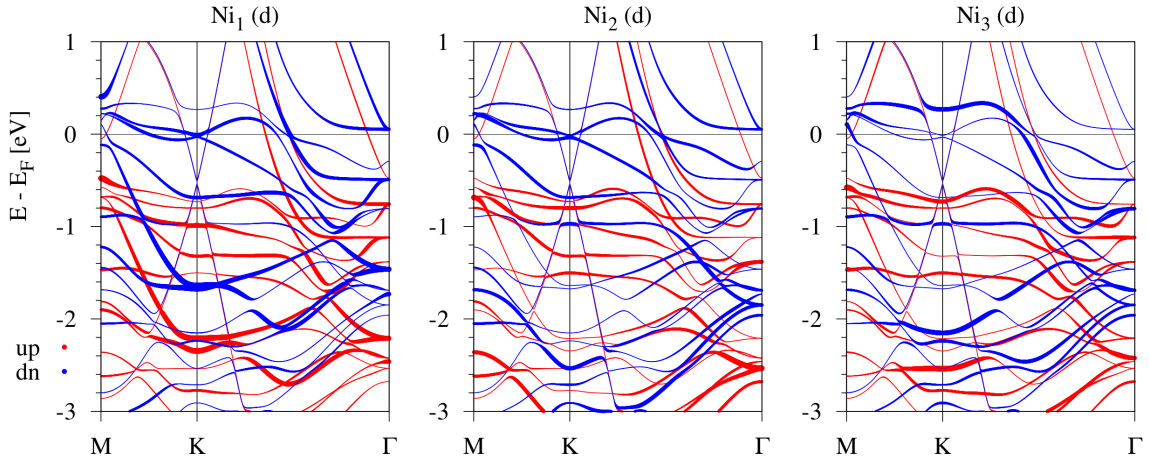

FIG. 3.18: Spin polarized band structure of graphene/hBN/nickel heterostructure with character of the d orbitals of the different nickel layers Ni_α, $\alpha = 1, 2, 3$. Spin up (down) bands are shown in solid red (blue). Thickness of the bands are weighted with the character of the d orbitals of the different nickel atoms.

nickel to be 0.6 eV in agreement with the magnetic moment. The band structure also shows, very similar to the case with cobalt, three d bands in the vicinity of the Dirac point, possibly influencing the graphene band structure. The spin down d band is mainly originating from all d orbitals of atoms Ni_1 and Ni_2, see Fig. 3.17, except for d_{z^2} orbitals, in contrast to the cobalt case, due to the different lattices of nickel and cobalt. The two highest lying spin up bands originate from d_{z^2} orbitals of Ni_2 and Ni_3, similar as for the cobalt substrate. In contrast to cobalt, the three d bands of nickel are all crossing the valence Dirac states and the energy window from -0.5 to 0 eV at the K point is free from nickel d bands. We apply our model Hamiltonian, Eq. (3.5), to describe the low energy graphene band structure near the Dirac point.

Figure 3.19(a) shows the calculated spin polarized band structure of the graphene/hBN/nickel heterostructure for one layer of hBN. The graphene Dirac states for spin up are lying lower in energy than the spin down ones, as for the cobalt case. By comparison between nickel and cobalt we notice that the Dirac point energy E_D for nickel is about 100 meV lower in energy than for cobalt, but the proximity induced band splittings are smaller, as expected due to the smaller magnetic moment of nickel. In general the band structures are quite similar with the difference that nickel d states do not influence the Dirac states as much as cobalt does, which manifests in smaller values of the hybridization parameters $j^{A,B}_{\uparrow,\downarrow}$ for nickel. Most of all, we notice that there is no d band crossing the conduction Dirac states in the chosen energy and k-region. The fit to the p_z-d-model is shown by solid lines to the DFT data in

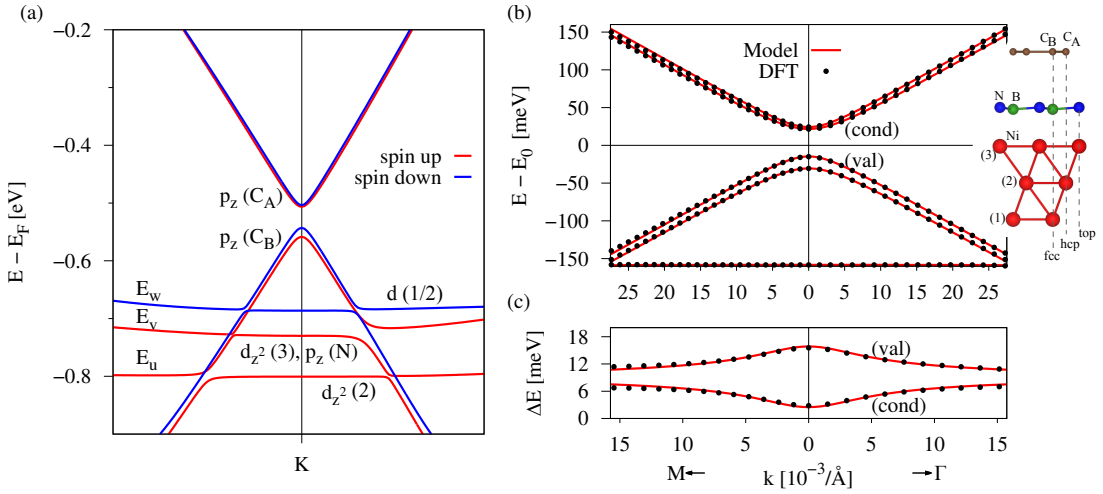

FIG. 3.19: Spin polarized band structure of the graphene/hBN/nickel heterostructures for one layer of hBN. (a) Band structure in the vicinity of the Dirac point with labels for the main orbital contributions. Labels E_j, j = u,v,w are the energy bands, which correspond to the nickel d states used to fit the p_z-d-model Hamiltonian in Eq. (3.5). (b) The fit to the p_z-d-model with a side view of the structure. First principles data (dotted lines) are well reproduced by the model (solid lines). (c) The corresponding splittings of the valence (val) and conduction (cond) Dirac states of graphene. The fit parameters are $E_0 = -527.98$ meV, $\tilde{\Delta} = 22.98$ meV, $\tilde{\lambda}^{\mathrm{A}}_{\mathrm{ex}} = -1.25$ meV, $\tilde{\lambda}^{\mathrm{B}}_{\mathrm{ex}} = 8.17$ meV, $E_{\mathrm{u}} = -272.58$ meV, $E_{\mathrm{v}} = -201.27$ meV, $E_{\mathrm{w}} = -158.17$ meV, $\mathrm{v}^{\mathrm{B}}_{\uparrow} = 10.15$ meV, $\mathrm{w}^{\mathrm{B}}_{\downarrow} = 4.19$ meV. The Fermi velocity to match the slope away from K point is $v_{\mathrm{F}} = 0.81 \times 10^6 \frac{\mathrm{m}}{\mathrm{s}}$. The fit parameters are again obtained in the same way as for the cobalt case.

Fig. 3.19(b). We see that the p_z-d-model Hamiltonian, Eq. (3.5), describes our first-principles results very well for the fit parameters given in Tab. 3.3. Similar to the cobalt case, the gap in the dispersion is roughly 40 meV and the band splittings are of the order of 10 meV. We additionally employ our p_z-model, Eq. (3.4), to extract the pure band splittings. The parameter values for the p_z-model are given in Tab. 3.4. Due to the weak hybridization with d orbitals, the minimal model parameters are very close to the parameters of the p_z-d-model.

Two hBN layers

Figure 3.20 shows the calculated band structure and the fit to the p_z-d-model in the case of two layers of hBN and three layers of nickel. Again the positions of carbon $\mathrm{C_A}$ has not changed with respect to the hBN layers, while position of $\mathrm{C_B}$ was changed to be on top of the uppermost boron atom. The layer distance between the two hBN layers was relaxed to $d_{\mathrm{hBN/hBN}} = 2.995$ Å and the distance between the uppermost hBN layer and graphene is $d_{\mathrm{hBN/Gr}} = 3.110$ Å in the two layer case. The corrugation of the lower hBN layer and the distance between hBN and nickel did not change. The inset in Fig. 3.20(b) shows the geometry for two layers of hBN.

Figure 3.20(a) shows the spin polarized band structure of graphene/hBN/nickel for two layers of hBN. The spin up graphene Dirac states are no longer lying lower in energy than the spin down ones, leading to reversal of the sign of the exchange parameters, just as for cobalt, see section 3.1.3. The fit parameters for the p_z-d-model are given in Tab. 3.3. The fit to

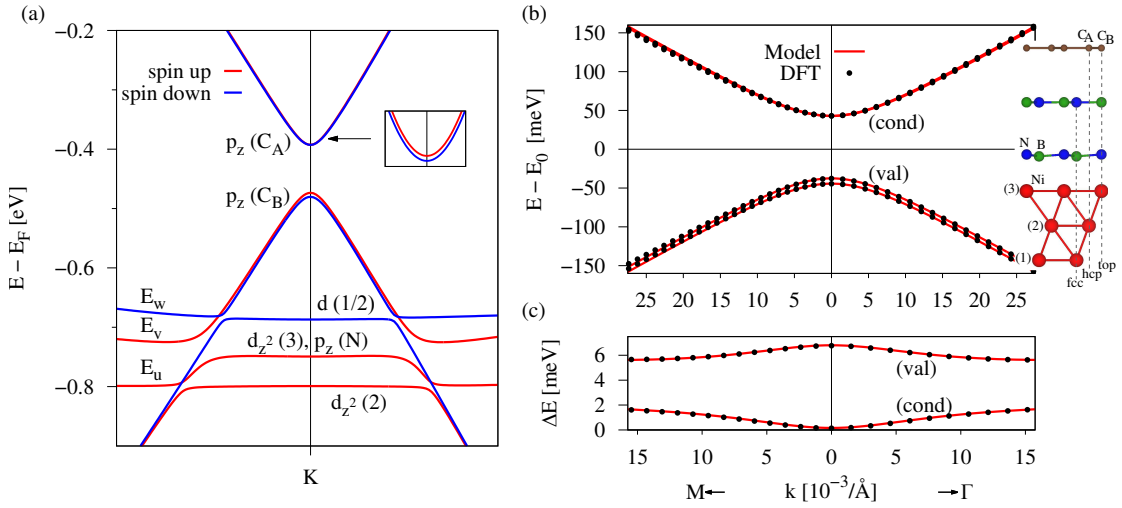

FIG. 3.20: Spin polarized band structure of graphene/hBN/nickel heterostructures for two layers of hBN (AA' stacking). (a) Band structure in the vicinity of the Dirac point with labels for the main orbital contributions. Inset shows a zoom on the conduction Dirac states to visualize the reversal of the spin states. (b) The fit to the p_z-d-model with a side view of the structure for two layers of hBN. First principles data (dotted lines) are well reproduced by the p_z-d-model (solid lines). (c) The corresponding splittings of the valence and conduction Dirac states. The fit parameters are $E_0 = -435.76$ meV, $\tilde{\Delta} = 42.88$ meV, $\tilde{\lambda}^{\mathrm{A}}_{\mathrm{ex}} = 0.080$ meV, $\tilde{\lambda}^{\mathrm{B}}_{\mathrm{ex}} = -1.44$ meV, $E_{\mathrm{u}} = -363.36$ meV, $E_{\mathrm{v}} = -309.27$ meV, $E_{\mathrm{w}} = -251.05$ meV, $\mathrm{v}^{\mathrm{B}}_{\uparrow} = 32.67$ meV. The Fermi velocity to match the slope away from K point is $v_{\mathrm{F}} = 0.824 \times 10^6 \frac{\mathrm{m}}{\mathrm{s}}$. All other parameters are zero for the same fitting range as for the one layer case.

the p_z-d-model is shown in Fig. 3.20(b). We can see, that the band splittings for both the conduction and valence Dirac states are smaller than in the single hBN layer case, as expected due to the additional insulating layer, while the proximity induced gap Δ nearly doubles, and the hybridization to the nickel $d_{z^2}(3)$ state is much larger. From the geometry in Fig. 3.20(b), we notice that carbon $\mathrm{C_B}$ has a direct connection with nickel atoms in top position via a nitrogen and a boron atom of the two individual hBN layers, which is responsible for the strong hybridization with the d band with energy E_{v}. This hybridization drives the strong proximity exchange in the valence band of graphene. By employing our p_z-model directly at the K point we extract parameters describing the pure splittings of the Dirac bands, corresponding to the values of the splittings in Fig. 3.20(c). The parameters from the p_z-model are given in Tab. 3.4. The values of $\tilde{\lambda}^{\mathrm{B}}_{\mathrm{ex}}$ and $\lambda^{\mathrm{B}}_{\mathrm{ex}}$, obtained from the two models are given in Tabs. 3.3, 3.4. In the case for nickel and two layers of hBN, they are of similar magnitudes, in contrast to the cobalt case, since the d band with energy E_{v} is relatively far away from the Dirac point energy, so that the hybridization effects on the band splittings at the K point are similar in monolayer and bilayer hBN structures. There is no resonant d level as in the cobalt case.

Additional Considerations

In the following, we consider the effective band splittings directly at the K point, which correspond to the exchange couplings in the minimal p_z-model.

Dependence of the number of hBN layers. Figure 3.21 shows the dependence of the proximity gap Δ and the two exchange parameters $\lambda_{\mathrm{ex}}^{\mathrm{A}}$ and $\lambda_{\mathrm{ex}}^{\mathrm{B}}$ on the number of hBN layers between nickel and graphene. Similar to cobalt the exchange parameters decrease by one order of magnitude and change sign by adding an additional insulating layer. The proximity gap Δ doubles for two layers of hBN and stays constant, since effectively the local environment for graphene does not change anymore by adding hBN layers. For completeness,

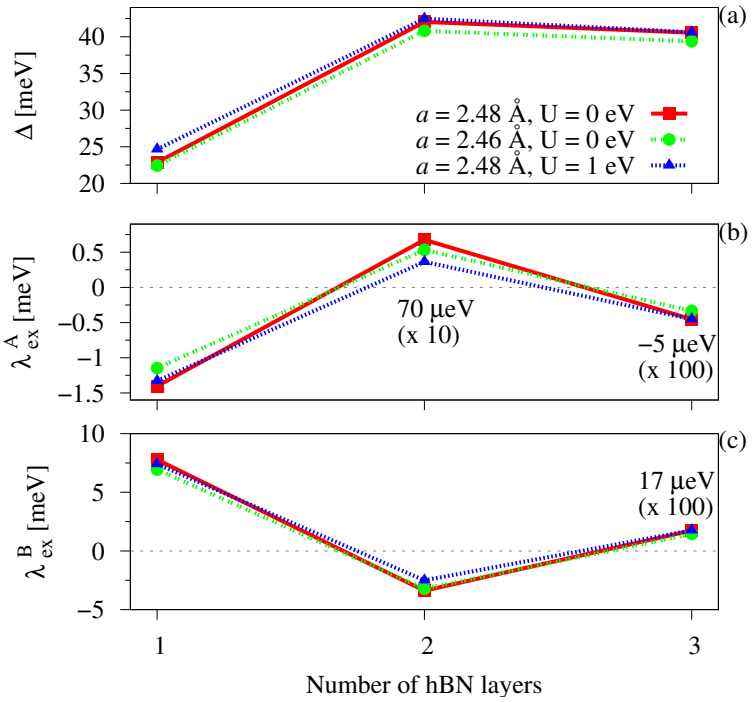

FIG. 3.21: Influence of additional number of hBN on the proximity induced parameters for the graphene/hBN/nickel structure, using the p_z-model at the K point. Dependence of (a) the proximity gap Δ, (b) the exchange parameters $\lambda_{\mathrm{ex}}^{\mathrm{A}}$, and (c) $\lambda_{\mathrm{ex}}^{\mathrm{B}}$ on additional hBN layers for different lattice constants or an additional Hubbard parameter of $U = 1.0$ eV. Parameter values for 2 (3) layers of hBN were increased by a factor of 10 (100) for better visualization as indicated.

the distances for the three layer case are similar to the two layer case. We have only one additional distance between the two hBN layers directly below graphene, which was relaxed to $d_{\mathrm{hBN/hBN}} = 3.073$ Å.

Also the bands of hBN are spin split, and similar as for the cobalt substrate, we look at the graphene/hBN/nickel structure with three layers of hBN. In the band structure we can identify the highest (lowest) lying valence (conduction) bands, which are spin split, of the three individual layers. From that, we extract the band splittings of conduction ΔE_{cond} and valence ΔE_{val} bands of the individual hBN layers at the K point. We notice that the spin up bands of hBN are always lying lower in energy than the spin down ones. In Fig. 3.22 we show the valence and conduction band splittings at the K point of the three layers. We notice that the splittings are very similar, but smaller in magnitude, compared to the cobalt case.

Lattice constant effects. We also look how the band structure of the slabs change when we use the graphene lattice constant, $a = 2.46$ Å, by simply changing the in-plane lattice constant to this value without changing the vertical distances between the layers. The results

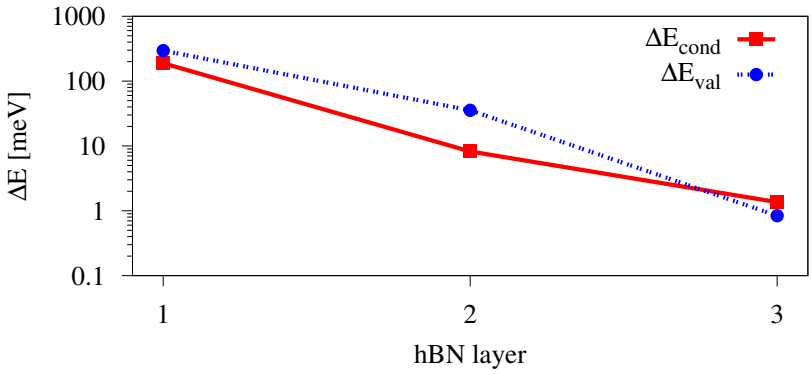

FIG. 3.22: Conduction ΔE_{cond} and valence ΔE_{val} band splittings of the three individual hBN layers at the K point. Values are obtained by identifying the spin split hBN conduction and valence bands of the three individual layers in the band structure of graphene/hBN/nickel heterostructure for three layers of hBN. Spin up bands of hBN are always lying lower in energy than the spin down ones at the K point.

in this case do not deviate much from the case with $a = 2.48$ Å, as can be seen in Fig. 3.21. The Fermi velocity for $a = 2.46$ Å and one hBN layer is $v_{\text{F}} = 0.822 \times 10^6$ m/s, corresponding to a larger nearest-neighbor hopping parameter of $t = 2.52$ eV.

Hubbard U. We now introduce a Hubbard parameter $U = 1.0$ eV to compare the results on the calculations of different number of layers of hBN with the ones with $U = 0$ eV. However, the influence of the additional on-site term on the band structure and the parameters is negligible, see Fig. 3.21, in contrast to the cobalt case. The band structures for the nickel case and for one/two layers of hBN, see Figs. 3.19, 3.20, show that the splittings of the Dirac bands at the K point, without a Hubbard U parameter, are already almost not affected by hybridization with d bands. Thus, if we shift away the d bands from the Dirac point by applying a Hubbard U parameter, the band splittings are almost unaffected.

Electric field effects. Figure 3.23 shows the influence of the electric field on the proximity parameters and the doping level for one hBN layer. We can see that E_{D} and Δ show the same trend with electric field. By increasing the electric field the doping level decreases. The proximity gap Δ also increases with increasing electric field reflecting the charge transfer away from graphene. The continuous shift of the doping level with the applied electric field allows to shift the Fermi level to the desired position. Compared to the case of cobalt, the proximity parameters for nickel change more smoothly with applied electric field. The magnitude of the proximity parameter $\lambda_{\text{ex}}^{\text{A}}$, on average, stays constant and the parameter $\lambda_{\text{ex}}^{\text{B}}$ slowly decreases with electric field, but for moderate fields the band splittings are almost unchanged. The electric tunability of the proximity exchange in this case is rather weak.

Figure 3.24 shows the influence of the electric field on the proximity parameters and the doping level for two hBN layers. We can see that E_{D} and Δ show the same trend with electric field, as for the single layer hBN, but the orbital gap parameter Δ is roughly twice as large as in the case with monolayer hBN. As we have already seen, the two proximity parameters λ_{ex} change their sign, by adding the second hBN layer. The magnitude of the proximity parameter $\lambda_{\text{ex}}^{\text{A}}$ stays roughly constant with electric field, but is one order of magnitude smaller

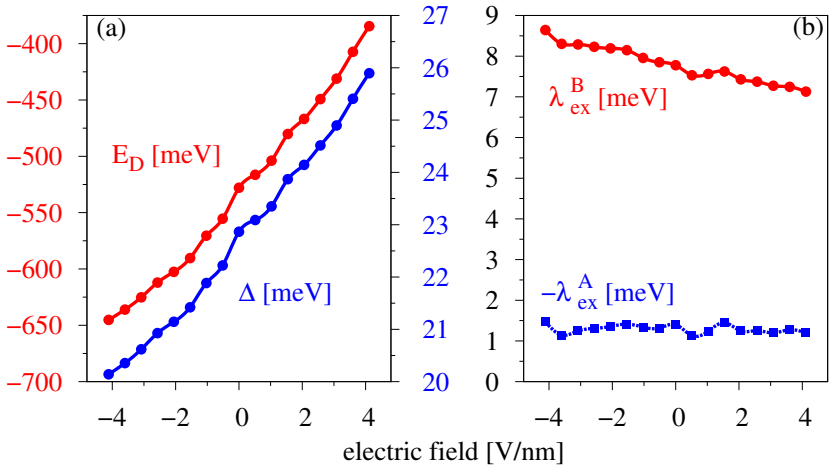

FIG. 3.23: Influence of the electric field on the proximity induced parameters for the graphene/hBN/nickel structure for one hBN layer, using the p_z-model at the K point. Dependence of the (a) Dirac energy E_D, the proximity gap Δ, and (b) the exchange parameters $\lambda^\mathrm{A}_\mathrm{ex}$ and $\lambda^\mathrm{B}_\mathrm{ex}$ on the applied transverse electric field.

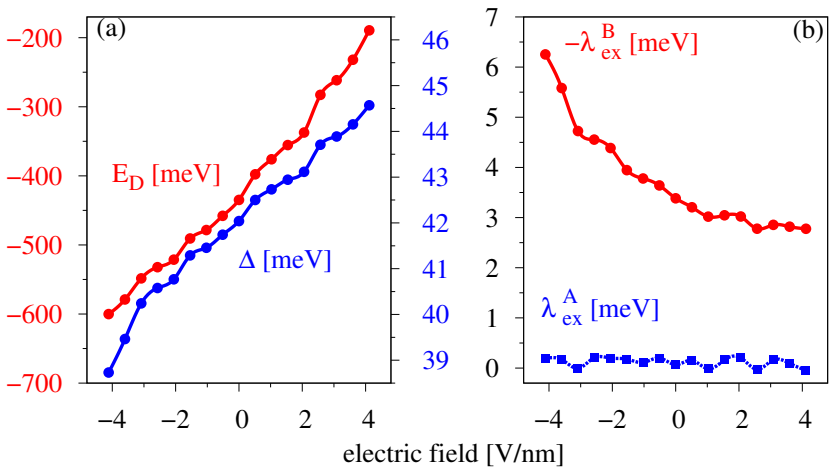

FIG. 3.24: Influence of the electric field on the proximity induced parameters for the graphene/hBN/nickel structure for two hBN layers, using the p_z-model at the K point. Dependence of the (a) Dirac energy E_D, the proximity gap Δ, and (b) the exchange parameters $\lambda^\mathrm{A}_\mathrm{ex}$ and $\lambda^\mathrm{B}_\mathrm{ex}$ on the applied transverse electric field.

than in the monolayer hBN case. The proximity parameter $\lambda^\mathrm{B}_\mathrm{ex}$ decreases with increasing electric field. For negative (positive) fields, the Dirac point is shifted in energy towards (away from) the hybridizing d levels, which cross the valence Dirac states, see Fig. 3.20, and $\lambda^\mathrm{B}_\mathrm{ex}$ is increasing (decreasing). We note that the magnitude of $\lambda^\mathrm{B}_\mathrm{ex}$ in the bilayer hBN case is comparable to the monolayer hBN case.

Additional nickel layers. Finally we analyze the influence of additional nickel layers on the band structure, see Fig. 3.25. As we increase the number of nickel layers, also more d bands are introduced in the dispersion. Consequently, in the vicinity of the K point graphene Dirac states can be disturbed by these additional nickel bands. We can see that the band splittings of graphene at the K point do not get influenced much by additional layers, since

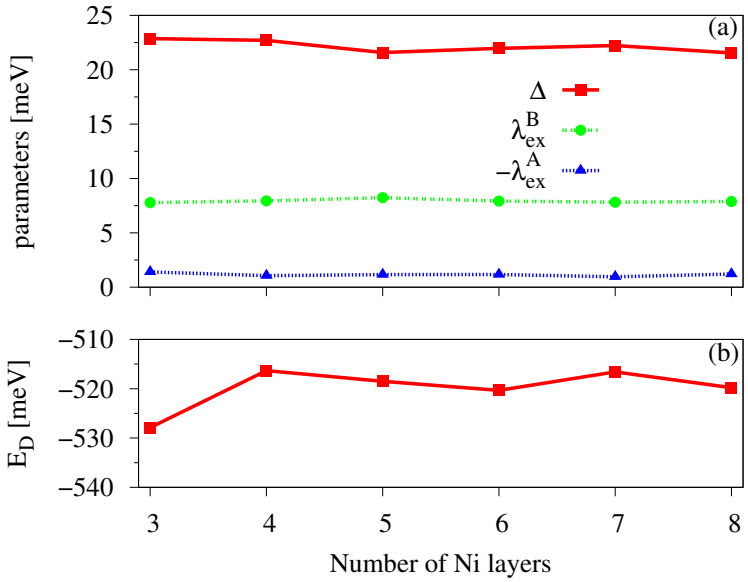

FIG. 3.25: Influence of additional number of cobalt layers on the band structure for the graphene/hBN/nickel system for one hBN layer, using the p_z-model at the K point. Dependence of the (a) the proximity gap Δ, and the exchange parameters $\lambda_{\mathrm{ex}}^{\mathrm{A}}$ and $\lambda_{\mathrm{ex}}^{\mathrm{B}}$ and (b) Dirac energy E_{D} on additional number of cobalt layers.

the parameters stay at the same order. In this case, already 4 layers of nickel show a *steady* situation for the Dirac energy E_{D}. The effect on the proximity parameters is negligible.

3.3. Summary

We have investigated the proximity induced exchange interaction induced by the ferromagnets cobalt and nickel into graphene through the insulator hBN. We found proximity induced exchange splittings of the order of 10 meV together with a proximity gap of 40 meV for one layer of hBN. As we go from one to two insulating layers, proximity induced exchange interaction does not only get weaker by one order of magnitude, but the signs of the exchange parameters reverse and the proximity gap doubles. This reversal of the signs continues for up to 4 layers of hBN; the gap stays essentially constant. The proximity induced splittings decrease by one order of magnitude for each additional layer. It is fascinating that the ferromagnetism in graphene is proximity induced by the ferromagnetic slab and that the strength of the proximity exchange behaves like a damped oscillator with respect to the number of hBN layers between graphene and the ferromagnet.

By changing the in-plane lattice constant of the slab vdW structure to the more reasonable graphene lattice constant, band splittings are not affected. An additional on-site Hubbard U term, can affect the band splittings of the Dirac states at the K point significantly, since hybridization effects of d bands with graphene p_z states play an important role, especially when a resonant d level is near the Dirac point, as in the case of cobalt and two layers of hBN. In addition we found that, by applying an electric field, we can continuously shift the doping level and tune the proximity gap. The exchange splittings of the bands are almost unaffected for one hBN layer, but if a resonant d level is near the Dirac point, we can control the sign of

the spin splitting, as we have seen for the valence Dirac band in the case with cobalt and two hBN layers. This allows to control the spin polarization in graphene, by an external electric field, if the d levels are indeed near the Dirac point. By adding ferromagnetic layers to the system we are able to *stabilize* the doping level, but we find that three ferromagnetic layers are enough to study the proximity effects.

Table 3.3 (3.4) summarizes the results on the presented structures for the different ferromagnets cobalt and nickel and for 1–3 layers of hBN, necessary to fit the DFT data of the corresponding structure with the p_z-d-model (p_z-model) Hamiltonian. We find that the results for both ferromagnets are quite similar, but in general the hybridization strength of cobalt is a bit larger compared to nickel, which is a consequence of the different atomic magnetic moments. When there are at least three layers of hBN between the ferromagnet and graphene, there is essentially no difference between cobalt and nickel anymore, since all hybridization effects are strongly suppressed.

FM	hBN [layer]	E_0 [meV]	$\tilde{\Delta}$ [meV]	$\tilde{\lambda}_{\mathrm{ex}}^{\mathrm{A}}$ [meV]	$\tilde{\lambda}_{\mathrm{ex}}^{\mathrm{B}}$ [meV]	E_{u} [meV]	E_{v} [meV]	E_{w} [meV]	IA [meV]	$v_{\mathrm{F}}/10^5$ [m/s]
Co	1	-430.89	21.45	-7.63	8.95	-279.41	-19.37	282.31	48.44 ($\mathrm{w}_{\downarrow}^{\mathrm{A}}$)	8.12
	2	-352.65	41.02	0.096	-0.512	-357.12	-114.75	207.34	41.67 ($\mathrm{v}_{\uparrow}^{\mathrm{B}}$)	8.20
	3	-301.07	38.83	-0.005	0.018	-408.70	-166.03	155.10	-	8.21
Ni	1	-527.98	22.98	-1.25	8.17	-272.58	-201.27	-158.17	10.15 ($\mathrm{v}_{\uparrow}^{\mathrm{B}}$), 4.19 ($\mathrm{w}_{\downarrow}^{\mathrm{B}}$)	8.10
	2	-435.76	42.88	0.080	-1.44	-363.36	-309.27	-251.05	32.67 ($\mathrm{v}_{\uparrow}^{\mathrm{B}}$)	8.24
	3	-361.54	40.42	-0.005	0.017	-437.30	-384.53	-324.91	-	8.26

TAB. 3.3: Summary of the most relevant parameters for all relevant structures ($a = 2.489$ Å and $U = 0$ eV) for the different ferromagnets (FM) cobalt and nickel for 1–3 layers of hBN, respectively. Proximity gap $\tilde{\Delta}$, energy shift E_0, exchange parameters $\tilde{\lambda}_{\mathrm{ex}}^{\mathrm{A}}$ and $\tilde{\lambda}_{\mathrm{ex}}^{\mathrm{B}}$, energies E_{u}, E_{v}, E_{w} of the interacting ferromagnet bands (measured with respect to E_0) and the interaction parameters (IA) necessary to fit the DFT data of the corresponding structure with the p_z-d-model Hamiltonian $\mathcal{H}$, Eq. (3.5).

FM	hBN [layer]	E_{D} [meV]	Δ [meV]	$\lambda_{\mathrm{ex}}^{\mathrm{A}}$ [meV]	$\lambda_{\mathrm{ex}}^{\mathrm{B}}$ [meV]
Co	1	-433.10	19.25	-3.14	8.59
	2	-348.03	36.44	0.097	-9.81
	3	-301.10	38.96	-0.005	0.018
Ni	1	-527.89	22.86	-1.40	7.78
	2	-434.82	42.04	0.068	-3.38
	3	-361.57	40.57	-0.005	0.017

TAB. 3.4: Summary of the parameters for all relevant structures ($a = 2.489$ Å and $U = 0$ eV) for the different ferromagnets (FM) cobalt and nickel for 1–3 layers of hBN, respectively. Proximity gap Δ, Dirac point energy E_{D}, exchange parameters $\lambda_{\mathrm{ex}}^{\mathrm{A}}$ and $\lambda_{\mathrm{ex}}^{\mathrm{B}}$ necessary to fit the DFT data of the corresponding structure with the minimal p_z-model Hamiltonian at the K point.

Two mechanisms are responsible for the band splittings of the graphene Dirac states. One is the general magnetic exchange, coming from proximity magnetism of the ferromagnetic

substrate, which is influenced by the barrier thickness. The thicker the barrier, the weaker is the general magnetic exchange splitting of the Dirac bands, since we increase the effective distance to the ferromagnetic substrate. Second, the hybridization of the graphene states with the d bands can additionally enhance the band splittings significantly. The strength of the hybridization depends on the energetic position of the d levels with respect to the Dirac point energy and from the fact, if there is a direct channel which can transport the magnetism from the ferromagnet to graphene, i.e. the effective overlap of the d_{z^2} orbitals with the p_z orbitals of graphene.

Chapter 4

Heterostructures with Oxide Insulators

In this chapter we consider the oxide insulators Al_2O_3 and SiO_2 to be the tunneling barriers between the ferromagnets and graphene. Oxide insulators usually appear in an amorphous structure and thus things like surface termination and energetically favorable stacking are hard to predict. As there are no DFT calculations on these structures so far, we are only presenting results on the structures as defined in the following. In order to keep the barrier between the ferromagnets and graphene as thin as possible, we take the oxide insulator thickness to be smaller than 5 Å. We know that we then need roughly one monolayer[1] of SiO_2, but only half a monolayer of Al_2O_3.

The (0001)-surface of Al_2O_3 was intensively studied during the years [63, 64], predicting an aluminum surface termination [65] with 1/3 monolayer of aluminum. Therefore we take this surface termination on the interfaces with graphene and the ferromagnets. Due to previous studies of the graphene/α-SiO_2(0001) interface [29, 58–60], we adopt an oxygen surface termination of SiO_2 at the interface with the graphene and place graphene at the hollow sites above SiO_2 following Ref. [29]. At the interface with the ferromagnets, we take a silicon surface termination of SiO_2. The problem is that from experiments, no unique surface termination can be determined and also the stacking configuration cannot be predicted for sure and thus we have to rely on our choice. In contrast to the hBN case, we also do not know how to stack the layers. Thus we simply start by putting the single layers (graphene, insulator and ferromagnet) on top of each other in a way, where we think that it is energetically favorable. To create the unit cells, we need to consider 2×2 supercells of graphene and the ferromagnets, which can then be matched with a 1×1 cell of the oxide insulators. For the vdW heterostructures we use in-plane lattice constants of $a = 4.92$ Å for SiO_2 and $a = 4.90$ Å for Al_2O_3. All atoms within the whole unit cell were allowed to adjust their x, y and z positions during the relaxation process, such that forces were reduced below 5×10^{-4} [Ry/a_0]. The vacuum distance of the vdW structures after relaxation is roughly 15 Å and the layer distances, which are very similar to the cases with hBN, are given in the corresponding section. The k-point sampling for the reduced Brillouin Zone in the oxide insulator cases was 54×54. All other computational details are the same as for the hBN case and can be found in appendix B.3

We will not perform an analysis of the structures in detail, as has been done in the cases for hBN, but to get a magnitude for the proximity induced magnetism, we extract the band splittings directly at the K point. The values of the proximity splittings in the graphene bands

[1] The lattice constants c of SiO_2 and Al_2O_3 are 5.405 Å and 12.98 Å. Thus we cut the unit cell such that we get the necessary thickness of roughly 5 Å for the barrier.

are only representative for the presented structures, as the stacking influences the strength of proximity induced effects. Lattice structures and band structure plots are shown for the cases with nickel as the ferromagnet only, since results are very similar for structures with cobalt. In general we expect the magnitude of the proximity magnetism to be small, since the effective thickness of the barriers between the ferromagnet and graphene is comparable to the case with two or three layers of hBN.

Unfortunately, we were not able to perform the relaxation of atomic positions for the structures with SiO_2 and thus we do not have any results for these cases. However, we expect that proximity effects are very similar for both oxide insulators. Results for the oxide insulator Al_2O_3 combined with the two ferromagnets cobalt and nickel, respectively, are listed in Tab. 4.1.

4.1. Graphene/Al_2O_3/Ferromagnet

We begin the analysis on the structures with the oxide insulators with Al_2O_3. After relaxation of atomic positions, we obtained the structure shown in Fig. 4.1 with the thickness of the Al_2O_3 layer itself to be 4.70 Å. The distance between graphene and Al_2O_3 was relaxed to $d_{\mathrm{Gr/Al_2O_3}} = 2.99$ Å and the distance between nickel and Al_2O_3 is $d_{\mathrm{Ni/Al_2O_3}} = 2.15$ Å. Both distances are slightly larger by roughly 0.03 Å in the cobalt case.

We can see that the structure now has an oxygen surface between graphene and Al_2O_3 even though we started with an aluminum surface termination with 1/3 monolayer of aluminum on both sides [65]. The weak interaction with graphene, allowed the surface aluminum atom on the graphene side to be pulled back towards Al_2O_3. On the interface side with nickel, the aluminum surface termination is still intact due to the strong interaction with the nickel surface. The structure with cobalt as the ferromagnet is very similar to the one with nickel. The two different carbon sublattices can be distinguished, by defining C_A at the hcp-sites

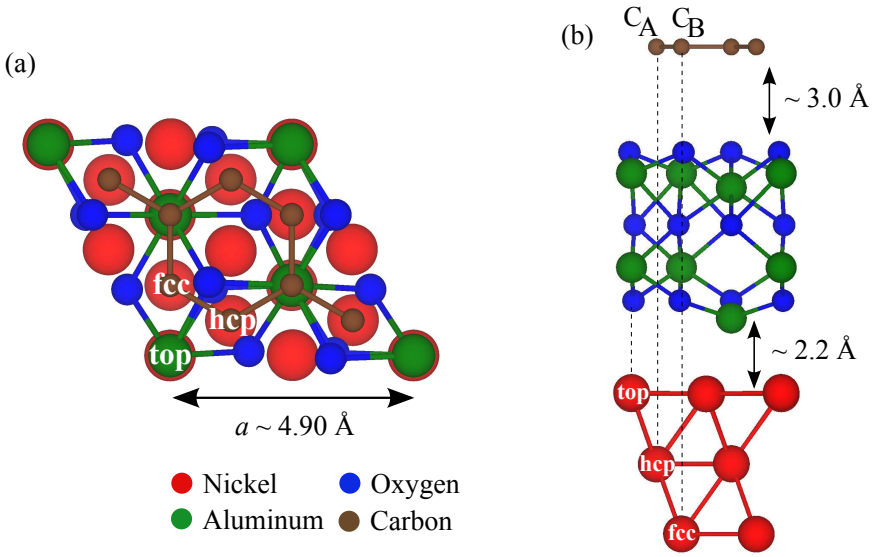

FIG. 4.1: Structure of graphene/Al_2O_3/nickel, with labels for the different atoms. (a) Top view of the structure shows one unit cell with the lattice constant $a = 4.90$ Å. (b) Side view with stacking configuration and layer distances as indicated.

and C_B at the fcc-sites above the nickel surface in Fig. 4.1(b). In Fig. 4.1(a) we can see that both sublattices are above an aluminum atom and above three nickel atoms in the unit cell. Thus, the sublattices A and B in total have almost the same effective environment and we expect only a small orbital gap in the spectrum, since sublattice symmetry should not be broken as strong as in the hBN case. Also the proximity induced band splittings should be small, since the thickness of the insulator is quite large.

We want to have a look at the general band structure of the system. In Fig. 4.2 we show the calculated spin polarized band structure of the graphene/Al_2O_3/nickel heterostructure divided into the two spin channels. What is very astonishing is that the graphene Dirac point is roughly 1 eV above the system Fermi level and Dirac states do not get influenced by any bands in a very large k and energy window around the Dirac point. By using our definition of the doping level, graphene is p-doped in the case of Al_2O_3 in contrast to hBN. The linear dispersion is nicely preserved and it seems that the graphene π-states do not get influenced, even though there is the Al_2O_3/nickel substrate below. Bands of the nickel are again located around the Fermi level and valence states of the Al_2O_3 layer are below -1.5 eV. Of course, d bands of the ferromagnet hybridize with states from the insulator. Since we are interested in proximity effects in graphene, we will not analyze this complete chaos in the band structure and immediately look at the graphene Dirac states.

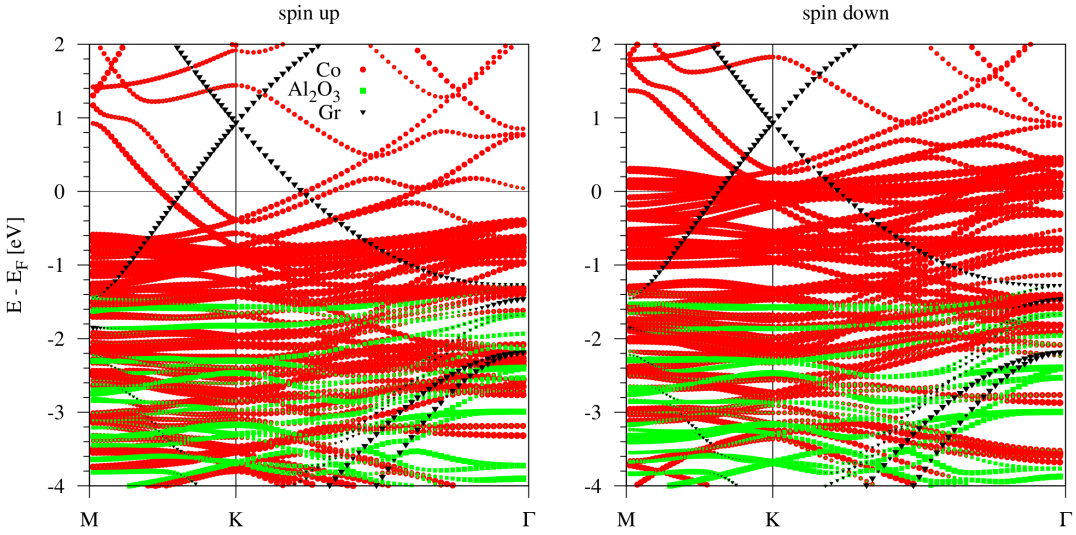

FIG. 4.2: Character plot of the spin polarized band structure of the graphene/Al_2O_3/nickel heterostructure along the high symmetry path M–K–Γ. Left panel: Spin up character plot of the band structure. Different colors correspond to the different layers of the vdW heterostructure (red = nickel, black = graphene, green = Al_2O_3). Right panel: Spin down character plot of the band structure.

In Fig. 4.3(a) we show a zoom on the calculated spin polarized band structure for the graphene/Al_2O_3/nickel heterostructure. Similar to one layer of hBN, we can see that the spin up Dirac states are lower in energy than spin down ones. However, the band gap and the splittings are very small. The fact, that no states influence the graphene Dirac bands allows to apply the p_z-model at the K point. We have to admit, that the conduction and valence Dirac states are no longer formed by a specific sublattice exclusively, as in the hBN case. Thus the sublattice resolved exchange Hamiltonian $\mathcal{H}_{\text{ex}}$ is in principle not valid as defined and the exchange parameters $\lambda_{\text{ex}}^{\text{A}}$ and $\lambda_{\text{ex}}^{\text{B}}$ do not represent the proximity magnetism

induced on a certain sublattice. However, the band structure can be nicely reproduced by the p_z-model for k points up to 10×10^{-3}/Å away from the K point, see Fig. 4.3(b),(c). The gap is roughly 2 meV, small compared to the hBN cases, since the two sublattices are effectively almost equal, as already mentioned. The band splittings are roughly 200 μeV, being comparable to the case with two or three layers of hBN. The proximity parameters

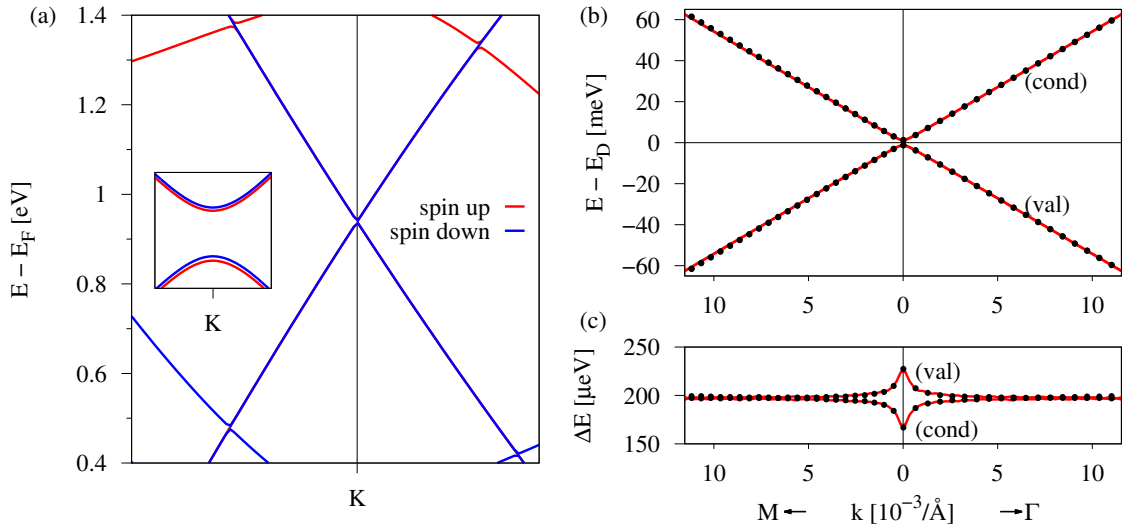

FIG. 4.3: Spin polarized band structure of graphene/Al_2O_3/nickel heterostructure. (a) Band structure in the vicinity of the Dirac point. Inset shows a zoom on the Dirac states to visualize the splitting of the spin states. (b) The fit to the p_z-model. First principles data (dotted lines) are well reproduced by the p_z-model (solid lines). (c) The corresponding splittings of the valence (val) and conduction (cond) Dirac states of graphene. The fit parameters are $E_D = 938.82$ meV, $\Delta = 1.28$ meV, $\lambda_{ex}^A = -0.083$ meV, $\lambda_{ex}^B = 0.114$ meV. The parameters are obtained, by applying the p_z-model at the K point. The Fermi velocity to match the slope away from K point is $v_F = 0.823 \times 10^6 \frac{m}{s}$.

obtained by the p_z-model, for the case of cobalt and nickel are listed in Tab. 4.1. We find that the band splittings are very similar in the case of cobalt. Due to the larger atomic magnetic moment in cobalt, the total band structure is a little bit different, namely spin up and spin down d bands of cobalt are more split in energy and thus spin down d bands are located around the Dirac point energy, in contrast to nickel. However, the spin down d bands of cobalt almost do not influence the graphene Dirac states due to the thick Al_2O_3 barrier and the situation is effectively the same as for nickel.

4.2. Summary

In summary we have investigated the oxide insulator Al_2O_3 as the barrier between the ferromagnets nickel/cobalt and graphene. The proximity induced band splittings in graphene are of the order of 200 μeV, the gap in the spectrum is around 2 meV. The parameters, obtained by applying the p_z-model at the K point, are listed in Tab. 4.1 for the heterostructures with the oxide insulator Al_2O_3. The mechanism that leads to the splitting of the bands is the general magnetic exchange, which depends on the barrier thickness and the strength of the

FM	OI	E_{D} [meV]	Δ [meV]	$\lambda_{\mathrm{ex}}^{\mathrm{A}}$ [meV]	$\lambda_{\mathrm{ex}}^{\mathrm{B}}$ [meV]	$v_{\mathrm{F}}/10^5$ [m/s]
Co	Al_2O_3	881.86	1.02	-0.055	0.066	8.23
Ni	Al_2O_3	938.82	1.28	-0.083	0.114	8.23

TAB. 4.1: Summary of the parameters for all relevant structures for the different ferromagnets (FM) cobalt and nickel with the oxide insulator (OI) Al_2O_3, respectively. Proximity gap Δ, Dirac point energy E_{D}, exchange parameters $\lambda_{\mathrm{ex}}^{\mathrm{A}}$ and $\lambda_{\mathrm{ex}}^{\mathrm{B}}$ and Fermi velocity v_{F} necessary to fit the DFT data of the corresponding structure with the minimal p_z-model Hamiltonian.

atomic magnetic moment of the ferromagnet. No hybridization effects with d bands from the ferromagnet influence the spin splittings of the Dirac bands.

In the case of SiO_2, we expect the strength of the proximity effects to be very similar to the presented case with Al_2O_3. In principle, also other insulating barriers like MgO or TiO_2 can be used for this kind of vdW structures, as reported in Refs. [66, 103–105]. However, hBN seems to be one of the most interesting candidates as the tunneling barrier.

Chapter 5

Summary and Outlook

In total we have investigated the magnetic proximity effect in graphene/insulator/ferromagnet structures. We have seen, that a gap opens at the Dirac point and that the Dirac bands of graphene get spin split, even if the insulating barrier is relatively thick, as for the oxide insulator Al_2O_3. Especially hBN is a promising candidate for vdW structures, since we have found a damped oscillation in the proximity exchange in graphene with respect to the number of hBN layers between graphene and the ferromagnet. In addition to that, hBN acts as a spin filtering tunnel barrier, which is especially attractive for the spin injection in graphene. By systematically studying several modifications of the vdW structure (number of ferromagnetic and insulating layers) as well as in the DFT input (electric field, Hubbard U), we provide reasonable proximity parameters that can be used in model charge and spin transport calculations. Moreover, we found that a resonantly coupled d level from the ferromagnet, near the Dirac point energy, can lead to a giant enhancement of the proximity spin splitting which can be tailored by electric field.

This whole study on proximity effects in graphene/insulator/ferromagnet structures can be continued by including SOC, which could further enhance the splitting of the Dirac bands, not only due to the SOC splitting in general, but also due to a possible spin-mixing hybridization of the d bands with the graphene Dirac states. As we have already started to study vdW structures with Al_2O_3, one could also think about using other oxide insulators (MgO, TiO_2). Moreover, other interesting materials exist, that can be used to create vdW structures. Especially transition metal dichalcogenides and topological insulators are intensively studied in current research.

Appendix A

Reminder on DFT

A.1. Many-particle systems

Typically, in condensed matter physics, we deal with a large number of atoms ($N \sim 10^{23}$) and to investigate properties of a solid one has to combine techniques of quantum mechanics and statistical physics. The difficulty comes from the large number of constituents and their possible interactions. To describe the microscopic properties of a solid, one needs to know the Hamiltonian of this system containing all kinetic and interaction terms

$$\mathcal{H} = \mathcal{T}_\mathrm{e} + \mathcal{T}_\mathrm{n} + \mathcal{V}_\mathrm{ee} + \mathcal{V}_\mathrm{nn} + \mathcal{V}_\mathrm{en}, \tag{A.1}$$

where every individual term contains at least a sum over N particles. By solving the corresponding Schrödinger equation, we can extract eigenstates and eigenenergies, necessary to calculate quantities of interest.

It would be nice to solve the exact equation, but this is nearly impossible due to the large amount of constituents in a solid. One needs to develop methods which can handle this Hamiltonian as accurate as possible, without neglecting anything of importance. Since the mass of the nucleus in an atom is much larger than the electron mass $\frac{\mathrm{m_e}}{\mathrm{M_I}} \sim 10^{-4}$ one can consider the electrons to be in a system, with a positive charge distribution from nuclei with fixed positions (Born-Oppenheimer approximation). The Hamiltonian A.1 reduces to

$$\mathcal{H} = \mathcal{T}_\mathrm{e} + \mathcal{V}_\mathrm{ee} + \mathcal{V}_\mathrm{ext} + E_c, \tag{A.2}$$

and because of the fixed position of the nuclei, their kinetic energy is zero. The interaction term between the nuclei reduces to a constant E_c, only leading to a shift in energy. The actual influence of the nuclei on the electrons is contained in the *external* potential $\mathcal{V}_\mathrm{ext}$, containing all kinds of interactions, depending on the system. The Hamiltonian we now have to consider is

$$\mathcal{H} = \mathcal{H}_\mathrm{el} + \mathcal{V}_\mathrm{ext}, \tag{A.3}$$

with a system-independent part $\mathcal{H}_\mathrm{el}$ and a part $\mathcal{V}_\mathrm{ext}$ which contains all the system-relevant information. Therefore we now have a wave function $\Psi(\{\boldsymbol{r}_i\})$, which only depends on the coordinates $\boldsymbol{r}_i$ of the electrons, since the positions of the nuclei are fixed. By this simple assumption life is already much easier.

A.2. Density functional theory

Still, the Hamiltonian contains too much terms, to be solvable as in a simple single particle Schrödinger equation. For solids, one commonly uses *Density Functional Theory* (DFT). This method was established by P. Hohenberg and W. Kohn (HK) in 1964. The most important quantity in this formalism is the electronic density $\rho(\boldsymbol{r})$

$$\rho(\boldsymbol{r}) = \sum_{i=1}^{N} |\phi_i(\boldsymbol{r})|^2, \tag{A.4}$$

contrary to the formalism of Schrödinger, where the wave function $\Psi(\boldsymbol{r}_i)$ plays the central role. The theorems of HK [106] prove that the density, which only depends on three parameters $\boldsymbol{r}$, provides the same information as the wave function, depending on $3N$ parameters $\boldsymbol{r}_i$.

Kohn and Sham (KS) developed out of the HK theorems methods for treating an inhomogeneous system of interacting electrons, the so called Kohn-Sham equations [107]. These are self-consistent equations with exchange and correlation effects contained in a suitable way. By minimizing the ground state energy functional written in the form

$$E[\rho] = \int \rho(\boldsymbol{r}) \mathcal{V}_{\text{ext}}(\boldsymbol{r}) d\boldsymbol{r} + \frac{1}{2} \int \frac{\rho(\boldsymbol{r})\rho(\boldsymbol{r}\,')}{|\boldsymbol{r} - \boldsymbol{r}\,'|} d\boldsymbol{r} d\boldsymbol{r}\,' + G[\rho] \tag{A.5}$$

one can derive equations, which are analogous to single particle equations. These Kohn-Sham equations read

$$\left[-\frac{\hbar^2}{2m} \nabla^2 + \left(\int \frac{\rho(\boldsymbol{r}\,')}{|\boldsymbol{r} - \boldsymbol{r}\,'|} d\boldsymbol{r}\,' + V_{\text{xc}}(\boldsymbol{r}) + V_{\text{ext}}(\boldsymbol{r}) \right) \right] \phi_i(\boldsymbol{r}) = \varepsilon_i \phi_i(\boldsymbol{r}), \tag{A.6}$$

where

$$V_{\text{xc}}(\boldsymbol{r}) = \frac{\delta E_{\text{xc}}}{\delta \rho}. \tag{A.7}$$

Now one has to solve, in a self-consistent way, single-particle equations for all the ϕ_i's, which actually describe quasi-particles with their energies ε_i. But by construction it is guaranteed, that the density of these quasi-particles is equal to the true electron density.

A.3. Exchange-Correlation functional

No approximations have been made so far, apart from the Born-Oppenheimer one, but the exchange-correlation energy E_{xc} is unknown and hence the search for functionals is central in DFT-research. Of course it has to be approximated, to make our theory applicable. Two different exchange-correlation functionals are extensively used in calculations, namely LDA (local density approximation) and GGA (generalized gradient approximation). For a slow varying density $\rho(\boldsymbol{r})$, $E_{\text{xc}}[\rho]$ can be written as

$$E_{\text{xc}}^{\text{LDA}}[\rho] = \int \rho(\boldsymbol{r}) \varepsilon_{\text{xc}}^{\text{HEG}}(\rho(\boldsymbol{r})) d\boldsymbol{r}, \tag{A.8}$$

with $\varepsilon_{\text{xc}}^{\text{HEG}}(\rho(\boldsymbol{r}))$ being the exchange-correlation energy density (energy per electron) of a uniform electron gas of density ρ [107]. This we call LDA, because the dependence of the

functional on the density is only local. $\varepsilon_{\mathrm{xc}}^{\mathrm{HEG}}(\rho(\boldsymbol{r}))$ is a function of ρ and we obtain an exchange-correlation potential of the form

$$V_{\mathrm{xc}}^{LDA}(\boldsymbol{r}) = \frac{\delta E_{xc}}{\delta \rho} = \varepsilon_{\mathrm{xc}}^{\mathrm{HEG}}(\rho(\boldsymbol{r})) + \rho(\boldsymbol{r}) \frac{\partial \varepsilon_{\mathrm{xc}}^{\mathrm{HEG}}(\rho(\boldsymbol{r}))}{\partial \rho(\boldsymbol{r})}. \tag{A.9}$$

It is surprisingly accurate for realistic systems, but it fails in systems that are dominated by electron-electron interaction effects (like heavy fermion systems), because there is no resemblance to a uniform electron gas [108].

A first step to improve LDA is to take also the density of the neighboring volumes into account. Therefore $\varepsilon_{\mathrm{xc}}$ should also depend on the gradient of the density, which is then called GGA. The exchange-correlation energy is now of the form

$$E_{\mathrm{xc}}^{\mathrm{GGA}}[\rho] = \int \rho(\boldsymbol{r}) \varepsilon_{\mathrm{xc}}(\rho(\boldsymbol{r}), \nabla\rho(\boldsymbol{r})) d\boldsymbol{r}, \tag{A.10}$$

where $\varepsilon_{\mathrm{xc}} \neq \varepsilon_{\mathrm{xc}}^{\mathrm{HEG}}$, is a function that depends on the density $\rho(\boldsymbol{r})$ and the gradient of the density $\nabla\rho(\boldsymbol{r})$. One can choose $\varepsilon_{\mathrm{xc}}$ in different ways, to get different GGA's. This freedom does not exist for LDA, because there is only one correct expression for $\varepsilon_{\mathrm{xc}}^{\mathrm{HEG}}$. The most appropriate and most reliable GGA's were proposed in 1996 by Perdew, Burke and Ernzerhof (GGA-PBE) [109].

A.4. Basis sets

The final step in DFT is, that one needs to solve equations of the form

$$\mathcal{H}_{\mathrm{sp}} \phi_i = \varepsilon_i \phi_i, \tag{A.11}$$

where $\mathcal{H}_{\mathrm{sp}}$ is a single particle Hamiltonian and ϕ_i are the Kohn-Sham single-particle orbitals. In general, one first needs to define a ground state density. But before we can define a density, we need a basis set ϕ_p^b, so that we can expand the wave function within the chosen basis set

$$\phi_i = \sum_{p=1}^{P} c_p^i \phi_p^b, \tag{A.12}$$

because we do not know how the ϕ_i's look like, which define the density. For an exact definition of ϕ_i, one needs an infinite basis set ($P \to \infty$), because the ϕ_i belong to a function space with infinite dimension. As this is not practical, we limit the number P, but accept, that we can only generate functions which are close to the exact ϕ_i. Having chosen a basis, the problem reduces to an eigenvalue problem and the search for the expansion coefficients c_p^i. If we choose a basis set, that is similar to the ϕ_i, the number P reduces, and we can still accurately describe the wave function (efficiency). This assumes, that one already knew the solution right before starting the calculation, which is in general not the case. So additionally the basis set should work for the majority of problems (unbiased).

Two different basis sets exist, which are mixed to combine their good properties. One are the plane waves, which accurately describe weakly bound/free electrons and the other ones are local orbitals/atomic like functions, which accurately describe heavily bound electrons.

It would be nice, if the basis functions are mathematically simple. Solids or crystals have a periodic structure and hence a periodic Hamiltonian and so we can choose the basis set to be plane waves. The wave function writes

$$\phi_{\boldsymbol{k}}^{n}(\boldsymbol{r}) = \sum_{\boldsymbol{K}} c_{\boldsymbol{K}}^{n,\boldsymbol{k}} \exp(i(\boldsymbol{k}+\boldsymbol{K})\boldsymbol{r}). \tag{A.13}$$

In this notation, $i = (n, \boldsymbol{k})$ and $p = \boldsymbol{k} + \boldsymbol{K}$. Remember that we have to limit our basis set. We choose $K \leq K_{max}$, that corresponds to a sphere with radius $R = K_{max}$ around the origin of reciprocal space. All reciprocal lattice vectors smaller than K_{max} are taken into the basis set. Determining the eigenvalue problem, yields for each eigenvalue $\varepsilon^{n,\boldsymbol{k}}$ an eigenvector $[c_{\boldsymbol{K}}^{n,\boldsymbol{k}}]_{P\times 1}$ of P values for $c_{\boldsymbol{K}}^{n,\boldsymbol{k}}$. The P eigenvalues each with their own set of coefficients, and each leading to another eigenfunction $\phi_{\boldsymbol{k}}^{n}$. So we found P different eigenfunctions, all with the same $\boldsymbol{k}$ but with different band index n. When we repeat the calculations for every $\boldsymbol{k}$, that is contained in the first Brillouin zone, we get the band structure. The number of $\boldsymbol{k}$'s defines the sampling. To make this ansatz applicable, we look at the wave function of a simple atom. The most oscillating part is near the nucleus, so one needs to modify something in this region. One can use atomic like functions in combination with plane waves or one can modify the potential (pseudopotential method). Chemistry happens in the outer shells, and for the description in the inner shells, we replace the potential through a pseudopotential, to reach smooth tails of the wave functions there. Going to the outer region, the potential evolves into the true potential.

Even though the pseudopotential method is useful, one cannot appropriately describe properties of the system near the nucleus. We have to search for another basis set, that describes the electrons properly, which means they are more or less *free* far away from the nuclei and near the nuclei they behave as bound to the atom. Therefore we use a combination of plane waves and atomic like functions. For this we divide the space into two regions. The so called muffin tin sphere S_α with radius R_α around each atom, and the remaining space outside of them called the interstitial region I; see Fig. A.1. The augmented plane wave (APW) basis set is defined as in Ref. [110]

$$\phi_{\boldsymbol{K}}^{\boldsymbol{k}}(\boldsymbol{r}, E) = \begin{cases} \frac{1}{\sqrt{V}} \exp(i(\boldsymbol{k}+\boldsymbol{K})\boldsymbol{r}), & \boldsymbol{r} \in I \\ \sum\limits_{l,m} A_{lm}^{\alpha,\boldsymbol{k}+\boldsymbol{K}} u_l^\alpha(r', E) Y_m^l(\theta', \phi'), & \boldsymbol{r} \in S_\alpha \end{cases} \tag{A.14}$$

The position inside the spheres is given with respect to the center of each sphere by $\boldsymbol{r}\,' = \boldsymbol{r} - \boldsymbol{r}_\alpha$. $u_l^\alpha(r', E)$ are the solutions of the radial part of the Schrödinger equation for a free atom α and $Y_m^l(\theta', \phi')$ are spherical harmonics. Inside S_α the basis is a linear combination of atomic functions ($A_{lm}^{\alpha,\boldsymbol{k}+\boldsymbol{K}}$ are coefficients) and should therefore be close to the actual eigenfunctions. One requirement is that the plane waves match the atomic functions in value, over the complete surface of the sphere, in order to determine the coefficients uniquely.

In order to describe the eigenstates accurately with this basis one needs to set the free parameter E, in $u_l^\alpha(r', E)$, equal to the band energy $\varepsilon_{\boldsymbol{k}}^n$ and therefore we have to start with a guessed value for $\varepsilon_{\boldsymbol{k}}^n$ before we start solving the secular equation. The APW method contains one difficulty, as we do not know the eigenenergies $E = \varepsilon_{\boldsymbol{k}}^n$ yet, to construct the basis set, because this is what we are actually searching for. For this the basis of Linearized Augmented Plane Waves (LAPW) exists in order to overcome this obstacle. We make a Taylor expansion

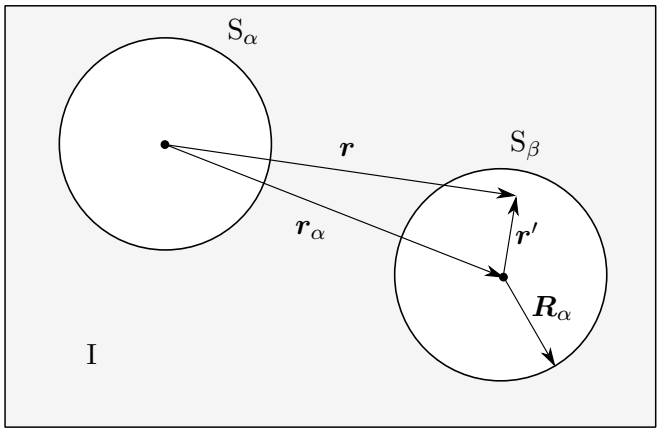

FIG. A.1: Definition of muffin tin sphere S$_\alpha$ with radius R_α around each atom and interstitial region I, taken from Ref. [110].

of $u_l^\alpha(r', E)$ around a specific energy E_0

$$u_l^\alpha(r', \varepsilon_{\boldsymbol{k}}^n) = u_l^\alpha(r', E_0) + (E_0 - \varepsilon_{\boldsymbol{k}}^n)\left.\frac{\partial u_l^\alpha(r', E)}{\partial E}\right|_{E=E_0} + \mathcal{O}\left[(E_0 - \varepsilon_{\boldsymbol{k}}^n)^2\right], \tag{A.15}$$

and take the first two terms into account, to create the LAPW basis

$$\phi_{\boldsymbol{K}}^{\boldsymbol{k}}(\boldsymbol{r}, E) = \begin{cases} \frac{1}{\sqrt{V}}\exp(i(\boldsymbol{k}+\boldsymbol{K})\boldsymbol{r}), & \boldsymbol{r} \in I \\ \sum\limits_{l,m}(A_{lm}^{\alpha,\boldsymbol{k}+\boldsymbol{K}} u_l^\alpha(r', E_0) + B_{lm}^{\alpha,\boldsymbol{k}+\boldsymbol{K}} \dot{u}_l^\alpha(r', E_0))Y_m^l(\theta', \phi'), & \boldsymbol{r} \in S_\alpha \end{cases} \tag{A.16}$$

where $\dot{u}_l^\alpha = \left.\frac{\partial u_l^\alpha(r', E)}{\partial E}\right|_{E=E_0}$. An additional coefficient must be introduced, because we do not know the energy difference $E_0 - \varepsilon_{\boldsymbol{k}}^n$. To determine $A_{lm}^{\alpha,\boldsymbol{k}+\boldsymbol{K}}$ and $B_{lm}^{\alpha,\boldsymbol{k}+\boldsymbol{K}}$ we need the matching, at the sphere boundary, to the plane waves in value and slope. In order to accurately describe the band structure, we should choose a set of $E_{1,l}^\alpha$ (for every band l) and not an universal E_0 in Eq. A.16. The limitation criteria here is the product $R_\alpha^{min} K_{max}$, where R_α^{min} is the smallest muffin tin radius. A well bound electron to the nucleus is called a core state and participates not in chemical bonding. It is therefore contained in the muffin tin sphere. States outside the sphere take part in chemical bonding and are called valence states and are treated by LAPW. Low lying valence states are called semi-core states. If we want to describe these, we do not know how to choose $E_{1,l}^\alpha$, because we do not know in which band these states sit. We can add another type of basis function to LAPW, a local orbital (LO), to solve this dilemma. A few more types of basis sets exist, such as the APW+lo, which combines the good features of APW and LAPW+LO; see e.g. Ref. [110].

Appendix B

Computational Implementation and Details

B.1. Program packages

The **Atomic Simulation Environment** (ASE) is a set of tools and Python modules for setting up, manipulating, running, visualizing and analyzing atomic simulations [111]. It was used to create the slab structures with the corresponding distances and to set up the input data of the calculations. We created the structures of the single layers and for the vdW heterostructures, single layers were stacked in a suitable way.

XCrySDen is a crystalline and molecular structure visualization program aiming at display of isosurfaces and contours, which can be superimposed on crystalline structures and interactively rotated and manipulated [112]. It was used to view the structures we generated and to produce the k-path for band structure calculations. After relaxation of atomic positions it was used to measure the distances between the single layers in the vdW systems.

VESTA is a 3D visualization program for structural models, volumetric data such as electron/nuclear densities, and crystal morphologies [113]. It was used to visualize the crystal structures, visualize spin polarizations or other volumetric data. All figures showing crystal structures were produced with VESTA.

QUANTUM ESPRESSO (QE) is an integrated suite of Open-Source computer codes for electronic-structure calculations and materials modeling at the nanoscale. It is based on density-functional theory, plane waves, and pseudopotentials. It is able to calculate ground state properties, perform structural optimizations, quantum transport and many more [114]. It was used for structural relaxation of the systems and the calculation of electronic properties, such as band structure and DOS. We calculated the ground state properties of the single layers, as well as for the vdW structures.

The program package **WIEN2k** allows to perform electronic structure calculations of solids using density functional theory (DFT). It is based on the full-potential (linearized) augmented plane-wave ((L)APW) + local orbitals (lo) method, one among the most accurate schemes for band structure calculations. WIEN2k is an all-electron scheme including relativistic effects and has many features [115]. It was used to compare and check the results obtained from QE-suite.

B.2. Lattice constant analysis

Since we deal with vdW heterostructures and all the single layers have a different lattice constant, we have to analyze the influence of the lattice constant on the electronic properties of the single layers, in order to get a reasonable structure. By calculating the band structure and ground state total energy of graphene for several different lattice constants, we can see that the lowest energy is obtained for a lattice constant of $a = 2.46$ Å, as expected for graphene, see Fig. B.1. However, when we take a lattice constant of $a = 2.49$ Å, the total

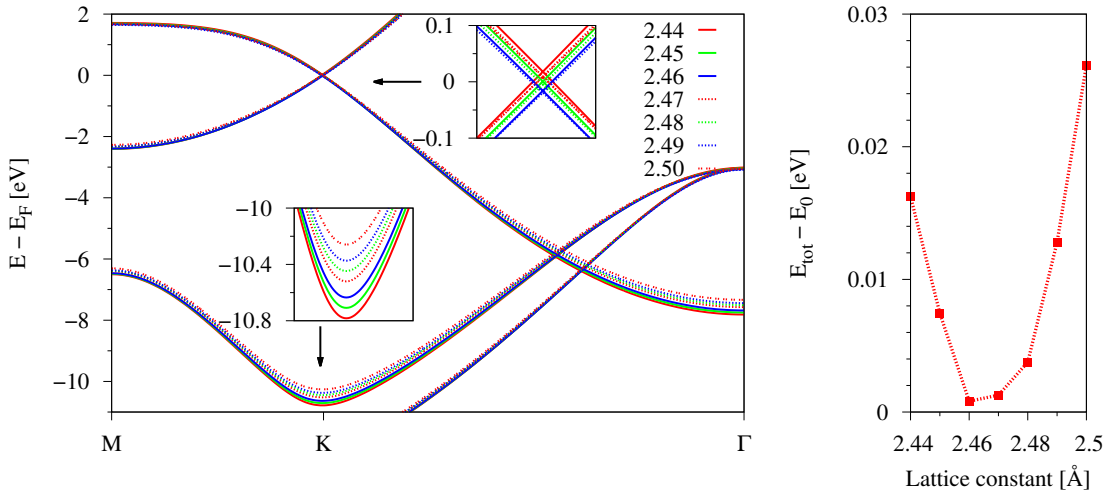

FIG. B.1: Influence of the lattice constant on the graphene band structure and the total energy. Left panel: Band structure for the different lattice constants. Insets show zooms on the corresponding region, indicated by the arrow, respectively. Right panel: Total energy as a function of the lattice constant a, normalized by reference energy E_0.

energy of the system changes only by 14 meV; in other words the energy per carbon atom is changed by 7 meV, which can be considered as a thermal fluctuation at room temperature.

When we look at the band structure, we can see that the Dirac states are almost not influenced. Thus we can say, that the low energy physics of graphene does not get affected if we use $a = 2.49$ Å for our vdW structure. The change in the band structure manifests mainly in the low energy bands, since these are formed by s, p_x and p_y orbitals, lying in the graphene plane, which get directly affected by the lattice constant. Going to larger lattice constants, shifts the low energy bands up in energy. Thus, from the graphene point of view, it should be okay to take a larger lattice constant of $a = 2.49$ Å, since our main interest lies in the Dirac states. The change in the lattice constant by this is 1.2%.

We make a similar analysis for hBN, see Fig. B.2, and find an optimal lattice constant of $a = 2.51$ Å, being very close to the experimental value of $a = 2.504$ Å. The change in energy by changing the lattice constant to $a = 2.49$ Å is roughly 10 meV, which is again small compared to the total energy of the system. Also the change in the band gap is negligible small, since it is roughly 10 meV. Both energies can be considered as thermal fluctuations at room temperature. Similar to graphene, low energy states are mainly affected by the lattice constant. In general by changing the lattice constant to $a = 2.49$ Å, the change is only 0.6%,

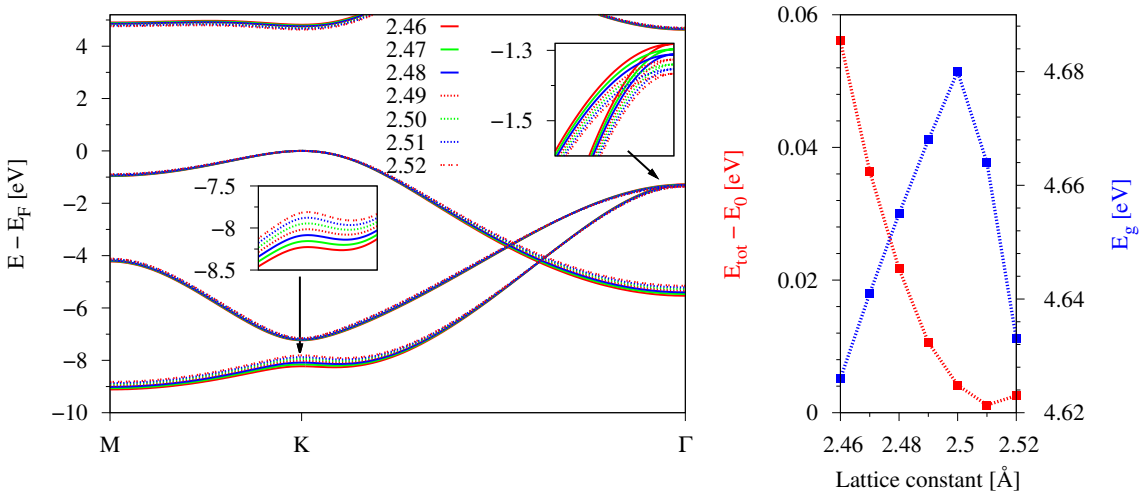

FIG. B.2: Influence of the lattice constant on the hBN band structure, the total energy and the band gap E_g. Left panel: Band structure for the different lattice constants. Insets show zooms on the corresponding region, indicated by the arrow. Right panel: Total energy normalized by reference energy E_0 (red curve) and band gap E_g (blue curve) as a function of the lattice constant a.

which is very small. In total if we now use a lattice constant of $a = 2.49$ Å for graphene and hBN, the basic physics should not be that different.

We make a further analysis, by looking at the heterostructure of graphene on hBN. By that we place graphene on top of hBN in the energetically most favorable way, as found in section 3.1.1. We allow the atoms to fully relax within the unit cell (x, y, z-coordinates) to minimize forces

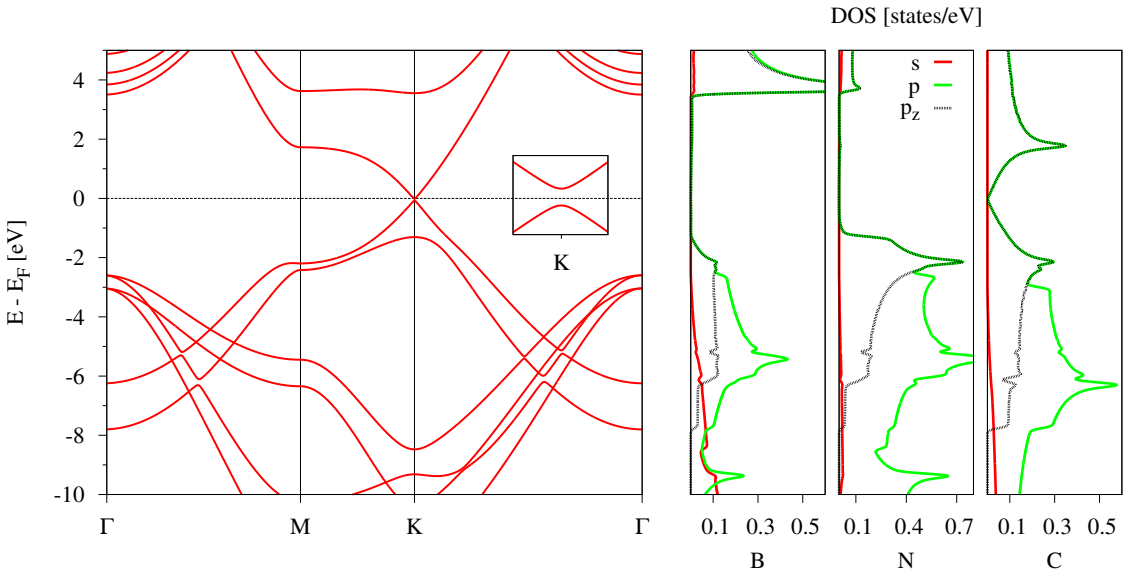

FIG. B.3: Band structure and corresponding orbital resolved DOS of graphene on hBN. Left panel: Band structure along the high-symmetry path Γ-M-K-Γ. The inset shows a zoom on the Dirac states with a gap of $E_g = 70.2$ meV. Right panel: Atom and orbital resolved DOS. Labels B, N and C correspond to the different atoms.

and also allow the system to perform a relaxation of the in-plane lattice constant to minimize the strain of the unit cell. We find a relaxed composite lattice constant of $a = 2.486$ Å and a layer spacing of $d = 3.136$ Å. We have to keep in mind, that in the graphene/hBN/cobalt heterostructure, we still have the lattice of cobalt with $a = 2.507$ Å. Thus, it is reasonable to take the assumed average lattice constants, for the vdW heterostructures as given in Tab. 2.2. Figure B.3 shows the band structure and the corresponding DOS of graphene on hBN for the composite lattice constant of $a = 2.486$ Å. We find an orbital gap in the graphene states at K of $E_g = 70.2$ meV, wich is in agreement with Ref. [24]. The graphene p_z states forming the Dirac cone are lying within the band gap of hBN.

B.3. Computational Methods

The calculations for the single layers were performed with QE and WIEN2k in order to ensure and check the correctness of the results, which slightly deviate, since the two programs are based on different methods. All of the given results on the relevant vdW heterostructures are from QE calculations. For calculations where a two dimensional slab structure was considered, we took a vacuum spacing of 14 Å.

In WIEN2k we performed convergence studies to get the values for $\mathrm{RK_{max}}$, which is the cutoff for the number of basis functions, and the k-point sampling, which additionally determines the accuracy. For calculations we used the following parameters. For single layers of graphene and hBN: $\mathrm{RK_{max}} = 9$ and a sampling of $60 \times 60 \times 1$ for self-consistent calculations. For the band structure we used a sufficient number of discrete k-points along the given high-symmetry paths. For bulk ferromagnets hcp-cobalt and fcc-nickel: $\mathrm{RK_{max}} = 9$ and a sampling of 120000 k-points within the Brillouin zone was used, for an accurate description of the ferromagnetic properties and the correct determination of the Fermi level. For bulk oxide insulators Al_2O_3 and SiO_2: $\mathrm{RK_{max}} = 9$ and a sampling of 120000 k-points within the Brillouin zone was used for an accurate description of the band gap. However, without using an accurate exchange correlation functional, the band gap is underestimated by roughly 30%. All electronic properties (band structure and orbital/spin resolved DOS) for the single layers presented in chapter 2 were calculated with WIEN2k. In QE we obtained very similar results.

In QE we especially dealt with the vdW structures. To study proximity induced exchange interaction in graphene, we consider graphene/insulator/ferromagnet heterostructures in a slab geometry. The calculation parameters for structures with hBN are given in the following. After performing convergence studies of the total and the Fermi energy, dependent on k-point sampling and cutoff, we found the following values. For self-consistent calculations a k-point sampling of $120 \times 120 \times 1$ was used. This large sampling of the Brillouin Zone is necessary for an accurate description of the system, especially for states near the Dirac cone and the determination of the correct Fermi level [28]. For band structure calculations we used a sufficient number of discrete k-values along the high-symmetry paths in the first Brillouin Zone. We used a kinetic energy cutoff for charge density and potential of 450 Ry, the kinetic energy cutoff for wavefunctions was 100 Ry for the `X.pbe-n-kjpaw.UPF` pseudopotential, which is scalar relativistic with the projector augmented wave method [116] with a Perdew-Burke-Ernzerhof exchange correlation functional [109] and a nonlinear core correction. For the relaxation of the heterostructures, we used vdW corrections [117], with a force relaxation using BFGS quasi-newton algorithm [118]. We also considered dipole corrections to avoid interactions between periodic images. To determine the interlayer distances, the atoms were

allowed to relax in their z positions (transverse to the layers) until all components of all forces were reduced below 10^{-4} [Ry/a_0], where a_0 is the bohr radius. The vacuum in z direction for these slab structures is roughly 15 Å after relaxation in order to simulate quasi-2D systems.

List of Figures

List of Tables

Bibliography

[1]K. S. Novoselov, A. K. Geim, S. V. Morozov, D. Jiang, Y. Zhang, S. V. Dubonos, I. V. Grigorieva, and A. A. Firsov, "Electric field effect in atomically thin carbon films", Science **306**, 666–669 (2004).

[2]D. R. Cooper et al., "Experimental Review of Graphene", ISRN Cond. Mat. Phys. **2012**, 1–56 (2012).

[3]C. Lee, X. Wei, J. W. Kysar, and J. Hone, "Measurement of the elastic properties and intrinsic strength of monolayer graphene.", Science **321**, 385–388 (2008).

[4]I. Lahiri, V. P. Verma, and W. Choi, "An all-graphene based transparent and flexible field emission device", Carbon **49**, 1614–1619 (2011).

[5]I. Zutic, J. Fabian, and S. Das Sarma, "Spintronics: fundamentals and applications", Rev. Mod. Phys. **76**, 323–410 (2004).

[6]J. Fabian, A. Matos-Abiague, C. Ertler, P. Stano, and I. Zutic, "Semiconductor spintronics", Acta Phys. Slovaca **57**, 565–907 (2007).

[7]A. Ferreira, T. G. Rappoport, M. A. Cazalilla, and A. H. Castro Neto, "Extrinsic spin hall effect induced by resonant skew scattering in graphene", Phys. Rev. Lett. **112**, 066601 (2014).

[8]T. Y. Yang, J. Balakrishnan, F. Volmer, a. Avsar, M. Jaiswal, J. Samm, S. R. Ali, a. Pachoud, M. Zeng, and M. Popinciuc, "Observation of long spin-relaxation times in bilayer graphene at room temperature", Phys. Rev. Lett. **107**, 5–8 (2011).

[9]A. H. Castro Neto and F. Guinea, "Impurity-induced spin-orbit coupling in graphene", Phys. Rev. Lett. **103**, 026804 (2009).

[10]M. Gmitra, D. Kochan, and J. Fabian, "Spin-orbit coupling in hydrogenated graphene", Phys. Rev. Lett. **110**, 246602 (2013).

[11]J. Zhou, Q. Liang, and J. Dong, "Enhanced spin–orbit coupling in hydrogenated and fluorinated graphene", Carbon **48**, 1405–1409 (2010).

[12]S. Irmer, T. Frank, S. Putz, M. Gmitra, D. Kochan, and J. Fabian, "Spin-orbit coupling in fluorinated graphene", Phys. Rev. B **91**, 115141 (2015).

[13]R. M. Guzmán-Arellano, A. D. Hernández-Nieves, C. A. Balseiro, and G. Usaj, "Gate-induced enhancement of spin-orbit coupling in dilute fluorinated graphene", Phys. Rev. B **91**, 195408 (2015).

[14]K. M. McCreary, A. G. Swartz, W. Han, J. Fabian, and R. K. Kawakami, "Magnetic moment formation in graphene detected by scattering of pure spin currents", Phys. Rev. Lett. **109**, 186604 (2012).

[15]D. V. Fedorov, M. Gradhand, S. Ostanin, I. V. Maznichenko, A. Ernst, J. Fabian, and I. Mertig, "Impact of electron-impurity scattering on the spin relaxation time in graphene: a first-principles study", Phys. Rev. Lett. **110**, 156602 (2013).

[16]D. Ma, Z. Li, and Z. Yang, "Strong spin–orbit splitting in graphene with adsorbed au atoms", Carbon **50**, 297–305 (2012).

[17]S. Abdelouahed, A. Ernst, J. Henk, I. V. Maznichenko, and I. Mertig, "Spin-split electronic states in graphene: effects due to lattice deformation, rashba effect, and adatoms by first principles", Phys. Rev. B **82**, 125424 (2010).

[18]K. Pi, W. Han, K. M. McCreary, A. G. Swartz, Y. Li, and R. K. Kawakami, "Manipulation of spin transport in graphene by surface chemical doping", Phys. Rev. Lett. **104**, 187201 (2010).

[19]J. Hu, J. Alicea, R. Wu, and M. Franz, "Giant topological insulator gap in graphene with 5d adatoms", Phys. Rev. Lett. **109**, 266801 (2012).

[20]C. Weeks, J. Hu, J. Alicea, M. Franz, and R. Wu, "Engineering a robust quantum spin hall state in graphene via adatom deposition", Phys. Rev. X **1**, 021001 (2011).

[21]K. Zollner, T. Frank, S. Irmer, M. Gmitra, D. Kochan, and J. Fabian, "Spin-orbit coupling in methyl functionalized graphene", Phys. Rev. B **93**, 045423 (2016).

[22]S. Konschuh, M. Gmitra, and J. Fabian, "Tight-binding theory of the spin-orbit coupling in graphene", Phys. Rev. B **82**, 245412 (2010).

[23]H. González-Herrero, J. M. Gómez-Rodríguez, P. Mallet, M. Moaied, J. J. Palacios, C. Salgado, M. M. Ugeda, J.-Y. Veuillen, F. Yndurain, and I. Brihuega, "Atomic-scale control of graphene magnetism by using hydrogen atoms", Science **352**, 437–441 (2016).

[24]G. Giovannetti, P. a. Khomyakov, G. Brocks, P. J. Kelly, and J. Van Den Brink, "Substrate-induced band gap in graphene on hexagonal boron nitride: Ab initio density functional calculations", Physical Review B **76**, 2–5 (2007).

[25]G. Giovannetti, P. A. Khomyakov, G. Brocks, V. M. Karpan, J. van den Brink, and P. J. Kelly, "Doping Graphene with Metal Contacts", Physical Review Letters **101**, 026803 (2008).

[26]M. V. Kamalakar, A. Dankert, J. Bergsten, T. Ive, and S. P. Dash, "Enhanced tunnel spin injection into graphene using chemical vapor deposited hexagonal boron nitride.", Sci. Rep. **4**, 6146 (2014).

[27]M. V. Kamalakar, A. Dankert, P. J. Kelly, and S. P. Dash, "Inversion of Spin Signal and Spin Filtering in Ferromagnet|Hexagonal Boron Nitride-Graphene van der Waals Heterostructures", Scientific Reports **6**, 21168 (2016).

[28]M. Bokdam, P. a. Khomyakov, G. Brocks, and P. J. Kelly, "Field effect doping of graphene in metal|dielectric|graphene heterostructures: A model based upon first-principles calculations", Physical Review B **87**, 075414 (2013).

[29]T. C. Nguyen, M. Otani, and S. Okada, "Semiconducting electronic property of graphene adsorbed on (0001) surfaces of SiO2", Phys. Rev. Lett. **106**, 1–4 (2011).

[30]T. Frank, M. Gmitra, and J. Fabian, "Theory of electronic and spin-orbit proximity effects in graphene on Cu(111)", Phys. Rev. B **93**, 1–7 (2016).

[31]G. Bertoni, L. Calmels, A. Altibelli, and V. Serin, "First-principles calculation of the electronic structure and EELS spectra at the graphene/Ni(111) interface", Physical Review B **71**, 1–8 (2005).

[32]M.-B. Martin et al., "Protecting nickel with graphene spin-filtering membranes: A single layer is enough", Appl. Phys. Lett. **107**, 012408 (2015).

[33]B. Dlubak et al., "Graphene-passivated nickel as an oxidation-resistant electrode for spintronics", ACS Nano **6**, 10930–10934 (2012).

[34]V. M. Karpan, G. Giovannetti, P. A. Khomyakov, M. Talanana, A. A. Starikov, M. Zwierzycki, J. van den Brink, G. Brocks, and P. J. Kelly, "Graphite and Graphene as Perfect Spin Filters", Phys. Rev. Lett. **99**, 176602 (2007).

[35]P. Lazić, G. M. Sipahi, R. K. Kawakami, and I. Žutić, "Graphene spintronics: Spin injection and proximity effects from first principles", Phys. Rev. B **90**, 085429 (2014).

[36]C. L. Kane and E. J. Mele, "Quantum Spin hall effect in graphene", Phys. Rev. Lett. **95**, 226801 (2005).

[37]D. Huertas-Hernando, F. Guinea, and A. Brataas, "Spin-orbit coupling in curved graphene, fullerenes, nanotubes, and nanotube caps", Phys. Rev. B **74**, 155426 (2006).

[38]H. X. Yang, A. Hallal, D. Terrade, X. Waintal, S. Roche, and M. Chshiev, "Proximity Effects Induced in Graphene by Magnetic Insulators: First-Principles Calculations on Spin Filtering and Exchange-Splitting Gaps", Phys. Rev. Lett. **110**, 046603 (2013).

[39]Q. Wu, L. Shen, Z. Bai, M. Zeng, M. Yang, Z. Huang, and Y. P. Feng, "Efficient spin injection into graphene through a tunnel barrier: Overcoming the spin-conductance mismatch", Physical Review Applied **2**, 1–10 (2014).

[40]P. Michetti and P. Recher, "Spintronics devices from bilayer graphene in contact to ferromagnetic insulators", Phys. Rev. B **84**, 1–8 (2011).

[41]Han Wei, Kawakami Roland K., Gmitra Martin, and Fabian Jaroslav, "Graphene spintronics", Nat Nano **9**, 794–807 (2014).

[42]B. Behin-Aein, D. Datta, S. Salahuddin, and S. Datta, "Proposal for an all-spin logic device with built-in memory", Nature nanotechnology **5**, 266–270 (2010).

[43]Z. Wang, C. Tang, R. Sachs, Y. Barlas, and J. Shi, "Proximity-Induced Ferromagnetism in Graphene Revealed by the Anomalous Hall Effect", Physical Review Letters **114**, 016603 (2015).

[44]C. Soldano, A. Mahmood, and E. Dujardin, "Production, properties and potential of graphene", Carbon **48**, 2127–2150 (2010).

[45]A. H. Castro Neto, F. Guinea, N. M. R. Peres, K. S. Novoselov, and a. K. Geim, "The electronic properties of graphene", Rev. Mod. Phys. **81**, 109–162 (2009).

[46]M. Gmitra, S. Konschuh, C. Ertler, C. Ambrosch-Draxl, and J. Fabian, "Band-structure topologies of graphene: Spin-orbit coupling effects from first principles", Physical Review B **80**, 1–5 (2009).

[47]M. Losurdo, M. M. Giangregorio, P. Capezzuto, and G. Bruno, "Graphene CVD growth on copper and nickel: role of hydrogen in kinetics and structure", Phys. Chem. Chem. Phys. **13**, 20836 (2011).

[48]L. C. Allen, "Electronegativity is the average one-electron energy of the valence-shell electrons in ground-state free atoms", J. Am. Chem. Soc. **111**, 9003–9014 (1989).

[49]A. Catellani, M. Posternak, A. Baldereschi, and A. J. Freeman, "Bulk and surface electronic structure of hexagonal boron nitride", Phys. Rev. B **36**, 6105–6111 (1987).

[50]X. Blase, A. Rubio, S. G. Louie, and M. L. Cohen, "Quasiparticle band structure of bulk hexagonal boron nitride and related systems", Phys. Rev. B **51**, 6868–6875 (1995).

[51]J. A. Camargo-Martinez and R. Baquero, "Performance of the modified becke-johnson potential for semiconductors", Phys. Rev. B **86**, 195106 (2012).

[52]J. Robertson, "Electronic structure and core exciton of hexagonal boron nitride", Phys. Rev. B **29**, 2131–2137 (1984).

[53]Z. Liu, L. Song, S. Zhao, J. Huang, L. Ma, J. Zhang, J. Lou, and P. M. Ajayan, "Direct growth of graphene/hexagonal boron nitride stacked layers", Nano Letters **11**, 2032–2037 (2011).

[54]G. E. Wood, A. J. Marsden, J. J. Mudd, M. Walker, M. Asensio, J. Avila, K. Chen, G. R. Bell, and N. R. Wilson, "van der Waals epitaxy of monolayer hexagonal boron nitride on copper foil: growth, crystallography and electronic band structure", 2D Materials **2**, 025003 (2015).

[55]M. Bokdam, G. Brocks, M. I. Katsnelson, and P. J. Kelly, "Schottky barriers at hexagonal boron nitride/metal interfaces: A first-principles study", Physical Review B **90**, 085415 (2014).

[56]V. M. Karpan, P. A. Khomyakov, G. Giovannetti, A. A. Starikov, and P. J. Kelly, "Ni(111)|graphene|h-BN junctions as ideal spin injectors", Physical Review B **84**, 153406 (2011).

[57]Y. Le Page and G. Donnay, "Refinement of the crystal structure of low-quartz", Acta Crystallogr. Sec. B **32**, 2456–2459 (1976).

[58]Z. Ao, M. Jiang, Z. Wen, and S. Li, "Density functional theory calculations on graphene/α-SiO2(0001) interface.", Nanoscale research letters **7**, 158 (2012).

[59]Y.-J. Kang, J. Kang, and K. J. Chang, "Electronic structure of graphene and doping effect on SiO2", Physical Review B **78**, 115404 (2008).

[60]X. F. Fan, W. T. Zheng, Z. X. Shen, and J.-L. Kuo, "Interaction between graphene and SiO2 surface", J. Phys. Condens. Matter **305004**, 1–17 (2011).

[61]T. H. DiStefano and D. E. Eastman, "The band edge of amorphous SiO2 by photoinjection and photoconductivity measurements", Solid State Communications **9**, 2259–2261 (1971).

[62]R. Gupta, "Electronic structure of crystalline and amorphous silicon dioxide", Physical Review B **32**, 8278–8292 (1985).

[63]M. Gautier, G. Fenaud, L. Pham Van, B. Villette, M. Pollak, N. Thromat, F. Jollet, and J.-P. Duraud, "alpha-Al2O3 (0001) Surfaces: Atomic and Electronic Structure", J. Am. Ceram. Soc. **77**, 323–334 (1994).

[64]V. Puchin, J. Gale, a.L. Shluger, E. Kotomin, J. Günster, M. Brause, and V. Kempter, "Atomic and electronic structure of the corundum (0001) surface: comparison with surface spectroscopies", Surface Science **370**, 190–200 (1997).

[65]R. D. Felice and J. E. Northrup, "Theory of the clean and hydrogenated Al2O3 (0001) surfaces", Physical Review B **60**, R16287–R16290 (1999).

[66]W. Han, K. Pi, K. M. McCreary, Y. Li, J. J. I. Wong, A. G. Swartz, and R. K. Kawakami, "Tunneling spin injection into single layer graphene", Phys. Rev. Lett. **105**, 167202 (2010).

[67]S. P. Dash, S. Sharma, J. C. Le Breton, J. Peiro, H. Jaffrès, J.-M. George, A. Lemaître, and R. Jansen, "Spin precession and inverted hanle effect in a semiconductor near a finite-roughness ferromagnetic interface", Phys. Rev. B **84**, 054410 (2011).

[68]C. Sevik and C. Bulutay, "Theoretical study of the insulating oxides and nitrides: SiO2, GeO2, Al2O3, Si3N4, and Ge3N4", J. Mater. Sci. **42**, 6555–6565 (2007).

[69]R. H. French, "Electronic Band Structure of Al2O3, with Comparison to Alon and AIN", J. Am. Ceram. Soc. **73**, 477–489 (1990).

[70]V. Murthy, *Structure and properties of engineering materials* (McGraw-Hill Education, 2003).

[71]A. Bosak, M. Krisch, M. Mohr, J. Maultzsch, and C. Thomsen, "Elasticity of single-crystalline graphite: Inelastic x-ray scattering study", Physical Review B **75**, 153408 (2007).

[72]K. Watanabe, T. Taniguchi, and H. Kanda, "Direct-bandgap properties and evidence for ultraviolet lasing of hexagonal boron nitride single crystal", Nature Materials **3**, 404–409 (2004).

[73]I. M. Billas, a. Châtelain, and W. a. de Heer, "Magnetism from the atom to the bulk in iron, cobalt, and nickel clusters.", Science **265**, 1682–1684 (1994).

[74]P. Enghag, *Encyclopedia of the elements: technical data - history - processing - applications* (Wiley, 2008).

[75]P. Rinke, E. Kioupakis, A. Janotti, F. Bechstedt, M. Scheffler, and C. G. Van De Walle, "First-principles optical spectra for F centers in MgO", Physical Review Letters **108**, 126404 (2012).

[76]G. Grad, P. Blaha, K. Schwarz, W. Auwärter, and T. Greber, "Density functional theory investigation of the geometric and spintronic structure of h-BN/Ni(111) in view of photoemission and STM experiments", Physical Review B **68**, 1–7 (2003).

[77]P. a. Khomyakov, G. Giovannetti, P. C. Rusu, G. Brocks, J. Van Den Brink, and P. J. Kelly, "First-principles study of the interaction and charge transfer between graphene and metals", Physical Review B **79**, 1–12 (2009).

[78]R. Laskowski, P. Blaha, and K. Schwarz, "Bonding of hexagonal BN to transition metal surfaces: An ab initio density-functional theory study", Physical Review B **78**, 045409 (2008).

[79]A. B. Preobrajenski, A. S. Vinogradov, and N. Mårtensson, "Monolayer of h-BN chemisorbed on Cu(111) and Ni(111): The role of the transition metal 3d states", Surf. Sci. **582**, 21–30 (2005).

[80]M. Bokdam, P. A. Khomyakov, G. Brocks, Z. Zhong, and P. J. Kelly, "Electrostatic doping of graphene through ultrathin hexagonal boron nitride films", Nano Letters **11**, 4631–4635 (2011).

[81]T. Abtew, B.-C. Shih, S. Banerjee, and P. Zhang, "Graphene-ferromagnet interfaces: hybridization, magnetization and charge transfer.", Nanoscale **5**, 1902–9 (2013).

[82]Y. S. Dedkov and M. Fonin, "Electronic and magnetic properties of the graphene/ferromagnet interface", New J. Phys. **12**, 125004 (2010).

[83]C. Tablero, "Electronic and magnetic properties of the Fe-doped CuInS2", Chemical Physics Letters **499**, 75–78 (2010).

[84]W. Gannett, W. Regan, K. Watanabe, T. Taniguchi, M. F. Crommie, and A. Zettl, "Boron nitride substrates for high mobility chemical vapor deposited graphene", Applied Physics Letters **98**, 242105 (2011).

[85]C. Dean, a. F. Young, L. Wang, I. Meric, G. H. Lee, K. Watanabe, T. Taniguchi, K. Shepard, P. Kim, and J. Hone, "Graphene based heterostructures", Solid State Communications **152**, 1275–1282 (2012).

[86]M. S. Driver, J. D. Beatty, O. Olanipekun, K. Reid, A. Rath, P. M. Voyles, and J. A. Kelber, "Atomic Layer Epitaxy of h-BN(0001) Multilayers on Co(0001) and Molecular Beam Epitaxy Growth of Graphene on h-BN(0001)/Co(0001)", Langmuir **32**, 2601–2607 (2016).

[87]A. Avsar et al., "Spin-orbit proximity effect in graphene.", Nat. Commun. **5**, 4875 (2014).

[88]M. Gmitra and J. Fabian, "Graphene on transition-metal dichalcogenides: A platform for proximity spin-orbit physics and optospintronics", Phys. Rev. B **92**, 155403 (2015).

[89]C. M. Singal and T. P. Das, "Electronic structure of ferromagnetic hcp cobalt. i. band properties", Phys. Rev. B **16**, 5068–5092 (1977).

[90]M. Vanin, J. J. Mortensen, a. K. Kelkkanen, J. M. Garcia-Lastra, K. S. Thygesen, and K. W. Jacobsen, "Graphene on metals: A van der Waals density functional study", Physical Review B **81**, 1–4 (2010).

[91]P. Moon and M. Koshino, "Electronic properties of graphene/hexagonal-boron-nitride moiré superlattice", Phys. Rev. B **90**, 155406 (2014).

[92]M. Bokdam, T. Amlaki, G. Brocks, and P. J. Kelly, "Band gaps in incommensurable graphene on hexagonal boron nitride", Phys. Rev. B **89**, 201404 (2014).

[93]M. Gmitra, D. Kochan, P. Högl, and J. Fabian, "Trivial and inverted dirac bands and the emergence of quantum spin hall states in graphene on transition-metal dichalcogenides", Phys. Rev. B **93**, 155104 (2016).

[94]P. Bruno and C. Chappert, "Ruderman-Kittel theory of oscillatory interlayer exchange coupling", Physical Review B **46**, 261–270 (1992).

[95]P. Bruno, "Oscillations of Interlayer Exchange Coupling vs. Ferromagnetic-Layers Thickness", EPL **23**, 615 (1993).

[96]K. Nakamura, R. Arita, Y. Yoshimoto, and S. Tsuneyuki, "First-principles calculation of effective onsite Coulomb interactions of 3d transition metals: Constrained local density functional approach with maximally localized Wannier functions", Phys. Rev. B **74**, 1–5 (2006).

[97]F. Aryasetiawan, K. Karlsson, O. Jepsen, and U. Schönberger, "Calculations of Hubbard U from first-principles", Phys. Rev. B **74**, 125106 (2006).

[98]O. G. A. Svane, "Transition-Metal Oxides in the Self-Interaction-Corrected Density-Functional Formalism", Physical Review Letters **65**, 1148–1151 (1990).

[99]A. Juhin, F. de Groot, M. Calandra, and C. Brouder, "Angular dependence of core hole screening in LiCoO2: A DFT+U calculation of the oxygen and cobalt K-edge x-ray absorption spectra", Physical Review B **81**, 115115 (2010).

[100]M. Forti, P. Alonso, P. Gargano, and G. Rubiolo, "Transition Metals Monoxides. An LDA+U Study", Procedia Materials Science **1**, 230–234 (2012).

[101]N. Ashcroft and N. Mermin, *Solid state physics* (Saunders College, 1976).

[102]C. Kittel, *Introduction to solid state physics* (Wiley, 2004).

[103]F. Volmer, M. Drögeler, E. Maynicke, N. von den Driesch, M. L. Boschen, G. Güntherodt, and B. Beschoten, "Role of MgO barriers for spin and charge transport in Co/MgO/graphene nonlocal spin-valve devices", Phys. Rev. B **88**, 161405 (2013).

[104]F. Godel, E. Pichonat, D. Vignaud, H. Majjad, D. Metten, Y. Henry, S. Berciaud, J.-F. Dayen, and D. Halley, "Epitaxy of MgO magnetic tunnel barriers on epitaxial graphene.", Nanotechnology **24**, 475708 (2013).

[105]M. W. Bräuninger, "Tunnel barriers for spin injection into graphene" (Universität Basel, 2014).

[106]P. Hohenberg and W. Kohn, "Inhomogeneous electron gas", Phys. Rev. **136**, B864–B871 (1964).

[107]W. Kohn and L. J. Sham, "Self-consistent equations including exchange and correlation effects", Phys. Rev. **140**, A1133–A1138 (1965).

[108]W. Kohn, "Nobel lecture: electronic structure of matter-wave functions and density functionals", Rev. Mod. Phys. **71**, 1253–1266 (1999).

[109]J. P. Perdew, K. Burke, M. Ernzerhof, D. of Physics, and N. O. L. 7. J. Quantum Theory Group Tulane University, "Generalized Gradient Approximation Made Simple", Phys. Rev. Lett. **77**, 3865–3868 (1996).

[110]S. Cottenier, *Density Functional Theory and the family of (L)APW-methods: a step-by-step introduction* (2002), ISBN 9080721514.

[111]S. R. Bahn and K. W. Jacobsen, "An object-oriented scripting interface to a legacy electronic structure code", Comput. Sci. Eng. **4**, 56–66 (2002).

[112]A. Kokalj, "XCrySDen—a new program for displaying crystalline structures and electron densities", J. Mol. Graph. Model. **17**, 176–179 (1999).

[113]K. Momma and F. Izumi, "VESTA3 for three-dimensional visualization of crystal, volumetric and morphology data", Journal of Applied Crystallography **44**, 1272–1276 (2011).

[114]P. Giannozzi et al., "QUANTUM ESPRESSO: a modular and open-source software project for quantum simulations of materials", J. Phys. Condens. Matter **21**, 395502 (2009).

[115]K. Schwarz and P. Blaha, "Solid state calculations using wien2k", Computational Materials Science **28**, 259–273 (2003).

[116]G. Kresse and D. Joubert, "From ultrasoft pseudopotentials to the projector augmented-wave method", Phys. Rev. B **59**, 1758–1775 (1999).

[117]S. Grimme, "Semiempirical gga-type density functional constructed with a long-range dispersion correction", Journal of Computational Chemistry **27**, 1787–1799 (2006).

[118]J. J. E. Dennis and J. J. Moré, "Quasi-newton methods, motivation and theory", SIAM Rev. **19**, 46–89 (1977).

Acknowledgments

At the end of my thesis I would like to thank all the people that supported me and contributed to this thesis.

First of all, I would like to express my deep gratitude to Prof. Jaroslav Fabian, who gave me the chance to write my thesis in his research group. During this period of time I have learned many things, which will be helpful for my further scientific work. Especially the topic, presented in this thesis, was carefully chosen and is very interesting.

I would like to thank my academic supervisors Martin Gmitra and Tobias Frank, for the helpful discussions and useful comments on the obtained results. I thank Tobias for his help when it came to computational problems, but also for the well-conceived comments, when I started with this topic. I thank Martin for the thought-provoking discussions of the results and for intensive support, not only on the scientific level, during this research project.

Finally, I would like to thank my family, friends and colleagues. Their support and care helped me to stay focused during my studies.

Erklärung gemäß § 39, Abs. (5) der Prüfungsordnung vom 29. November 2011

Ich erkläre hiermit, dass ich

- die vorliegende Abschlussarbeit selbstständig verfasst,
- keine anderen als die angegebenen Quellen und Hilfsmittel benutzt und
- die Arbeit nicht bereits an einer anderen Hochschule zur Erlangung eines akademischen Grades eingereicht habe.

Weiterhin bestätige ich hiermit, dass

- die vorgelegten Druckexemplare und die vorgelegte elektronische Version der Arbeit identisch sind,
- ich über wissenschaftlich korrektes Arbeiten und Zitieren aufgeklärt wurde und
- von den in § 24, Abs. (5) vorgesehenen Rechtsfolgen Kenntnis habe.

Regensburg, 14 Juli 2016 _____

Unterschrift